

IAEA-TECDOC-1607

Ion Beam Applications in Surface and Bulk Modification of Insulators



IAEA

International Atomic Energy Agency

December 2008

IAEA-TECDOC-1607

Ion Beam Applications in Surface and Bulk Modification of Insulators



IAEA

International Atomic Energy Agency

December 2008

The originating Section of this publication in the IAEA was:

Physics Section
International Atomic Energy Agency
Wagramer Strasse 5
P.O. Box 100
A-1400 Vienna, Austria

ION BEAM APPLICATIONS IN SURFACE AND BULK
MODIFICATION OF INSULATORS

IAEA, VIENNA, 2008

IAEA-TECDOC-1607

ISBN 978-92-0-112008-3

ISSN 1011-4289

© IAEA, 2008

Printed by the IAEA in Austria
December 2008

FOREWORD

Ion implantation and ion beam analysis are powerful tools for characterization and modification of materials by means of bombarding solids with energetic ions. Although the techniques have been highly developed during the past half century, they face new challenges as material processing approaches the nanometer scales.

Under a programme entitled Effective Utilization of Particle Accelerators, the IAEA has over recent years initiated two Coordinated Research Projects (CRPs) related to the modification and analysis of materials by ion beams: Use of Ion Beam Techniques for Analysis of Light Elements in Thin Films, including Depth Profiling, and Application of MeV Ion Beams for Development and Characterization of Semiconductor Materials. These CRPs attracted over 40 applications. In addition, some 12 developing Member States have received or applied for technical cooperation support to establish low energy particle accelerators suitable for ion beam analysis and materials modification. This interest underscores the worldwide attention that is being attracted generally by research in materials modification and the development of new advanced materials, and in particular, by ion beam applications in these endeavours.

Motivated by this interest and to continue supporting this important field of study, the IAEA in 2004 established a CRP on Ion Beam Modification of Insulators. The objectives of the CRP were (1) to facilitate applied, innovative R&D efforts utilising low energy accelerators to study material characteristics, develop appropriate techniques and synthesise novel materials, and (2) to strengthen the capacity of accelerator laboratories in developing Member States by encouraging partnerships with colleagues from developed Member States.

This publication includes outputs obtained from research contracts and agreements under this CRP. The document represents an output of a series of meetings, which started with the Advisory Group Meeting in 2002, and was followed by three Research Coordination Meetings (RCMs). The first RCM was held in Vienna in 2004, where agreement was reached on the coordinated aspects of the CRP, including research activities and milestones. In June 2006 a second RCM was hosted by iThemba LABS in South Africa, where participants reported on their progress and achievements. The final RCM was hosted by the Fast Neutron Research Facility, Chiang Mai University, Thailand, in December 2007, where participants reported their final results and evaluated the achievements of the CRP. The achievements of the participants within the three years of the CRP are included in this publication. The contributions of the participants and of their research colleagues are very much appreciated, as is the hospitality offered by the hosts of the RCMs.

It is with deep sadness that the members of the CRP received news of the passing away of Mr Zvonko Medunić of Zagreb (Croatia), who was an initiating member of this CRP.

The IAEA officer responsible for this IAEA-TECDOC was F. Mulhauser of the Division of Physical and Chemical Sciences. U. Rosengard initiated this CRP at the IAEA.

EDITORIAL NOTE

This publication has been prepared from the original material as submitted by the authors. The views expressed do not necessarily reflect those of the IAEA, the governments of the nominating Member States or the nominating organizations.

The use of particular designations of countries or territories does not imply any judgement by the publisher, the IAEA, as to the legal status of such countries or territories, of their authorities and institutions or of the delimitation of their boundaries.

The mention of names of specific companies or products (whether or not indicated as registered) does not imply any intention to infringe proprietary rights, nor should it be construed as an endorsement or recommendation on the part of the IAEA.

The authors are responsible for having obtained the necessary permission for the IAEA to reproduce, translate or use material from sources already protected by copyrights.

CONTENTS

Summary	1
Ion beam modification of polymer surfaces.....	9
<i>T. Tsvetkova, S. Balabanov</i>	
Modification of electronic properties in insulators using ion microprobe	19
<i>M. Jakšič, M. Karlušič, I. Bogdanovič Radovič,</i> <i>Ž. Pastuovič, N. Skukan, Z. Medunič</i>	
Formation of ferro-, para-, and superparamagnetic nanostructures by ion beam treatment of materials	27
<i>H. Hofsäass, C. Ronning, S. Müller, K. Zhang, H. Zutz</i>	
Formation of magnetic nanoclusters and complexes by ion implantation of Fe into suitable insulators	35
<i>K. Bharuth-Ram</i>	
Ion implantation doping of SrTiO ₃	43
<i>U. Wahl, J.G. Correia, A.C. Marques, C.P. Marques, E. Alves,</i> <i>L. Pereira, J.P. Araújo, K. Johnston</i>	
Ion beam modification of sputtered metal nitride thin films.....	53
<i>M. Milosavljevič, D. Peruško, M. Popovič, M. Novakovič</i>	
Ion beam synthesis and modification of silicon carbide	63
<i>Yu Liangdeng, Saweat Intarasiri, Teerasak Kamwanna, Somsorn Singkarat</i>	
Optimized pre-amorphization conditions for the formation of highly activated ultra shallow junctions in silicon-on insulator	93
<i>J.J. Hamilton, K.J. Kirkby</i>	
Publications resulting from the CRP	99
List of participants.....	103

SUMMARY

The development of new materials is driven by the high impact of such materials in important areas such as information technology, energy management, environmental protection, and human health. Most of these applications require devices having surface layers and thin film coatings or appropriately doped matrices with dedicated properties and structure. For many applications such accurately configured structures cannot be achieved by thermal diffusion methods. Ion beam methods, on the other hand, offer accurate control of implanted ion/dopant species, and implantation fluence, profile and temperature. They can be used to grow nano-composite materials by ion beam deposition, to create nano-patterned surfaces of materials by ion beam erosion, to introduce impurities into matrices by ion implantation, or to investigate novel properties resulting from impurity–defect interactions.

Ion beam modification of materials may be achieved by ion implantation or ion irradiation. These are unique approaches to altering the near surface region of a wide range of solid materials in a manner that is independent of many of the constraints associated with conventional processing methods. Some materials, such as metals and most semiconductors, are rather insensitive to the electronic part of the energy deposition as long as the electronic stopping power remains below a certain critical threshold value. Other materials, for example insulating and dielectric materials such as ionic solids, alkali and silver halides, dielectric glasses and amorphous materials, are quite sensitive to the energy deposited in their electronic systems. The high sensitivity of these materials to ion irradiation makes them particularly attractive for ion beam modification.

A comprehensive programme on ion beam modification requires not only facilities for materials production and ion beam implantation/irradiation, but also modern methods of analysis and diagnostics in order to characterize the ion beam induced effects. All these facilities may not be available in one laboratory, but can be achieved by means of collaboration between laboratories and scientists from developed and developing Member States. In the latter case, in particular, with appropriate partnerships with research centres in developed Member States and participation in research networks, research students and scientists have access to world class facilities and are able to take advantage of facility manpower supervision to enhance research development.

These issues and concerns impacted upon the research activities in this CRP which were organised into five main areas, namely:

- (1) Study of crystalline materials (e.g. silicon carbide and diamond) using ion beams;
- (2) Development of methods and techniques for ion implantation to produce buried layers;
- (3) Synthesis of sub-micron sized elemental phases and compounds with novel properties;
- (4) Ion induced modification of polymer properties;
- (5) Ion beam modifications of metal-nitride layers.

Eight projects were selected within this CRP, whose achievements are summarized in the following sections. Objectives 1 and 3 were studied by four groups, while objectives 2, 4 and 5 were covered each by two groups. Details of the projects are given in the participants' reports, while publications resulting from the CRP are collected in the last section.

ION BEAM MODIFICATION OF POLYMERS

Extending the understanding of the ion beam induced structural rearrangements effect on the relevant optical properties of polymer materials reveals new approaches to the design of devices with desired parameters, and leads to the development of high-performance polymers applications in different optical elements and luminescent devices. The formation of silicon carbide (SiC) in polymers was investigated using Si as the main implant species and ion fluences ranging from 10^{13} to 2×10^{17} cm^{-2} . Si ion implantation in ultra-high-molecular-weight-polyethylene results in photoluminescence properties such as emergence of ultra-violet range photoluminescence, and in poly-methyl-methacrylate in the appearance of photoluminescence enhancement. These effects may be related to the emergence of new photoluminescence sites associated with the presence of Si and/or SiC based clustering in the implanted polymer surface.

IR and Raman spectroscopy, as well as scanning electron microscopy studies of the implanted materials and Si elemental analysis provided tentative evidence for such clustering for samples implanted with the higher ion fluences. Micro-hardness measurements show a dramatic increase of surface hardness at low fluences which further increases with higher fluence, suggesting the effectiveness of the higher doses in creating the relevant structural changes. However in order to unequivocally identify the clusters and determine their size, transmission electron microscopy measurements are required. Post-implantation processes also need to be investigated.

MODIFICATION OF ELECTRONIC PROPERTIES IN INSULATORS USING ION MICROPROBE

Techniques have been developed that use focused MeV ion beams for the creation of new structures by modifying properties of materials, with particular emphasis on the use of heavy ions to create radiation damage in materials which can be used for new applications.

Structuring of radiation damage using heavy ion microbeams in crystalline materials has been developed and tested on silicon and diamond. In silicon, radiation damage can decrease charge collection properties and may be of interest in the production of position sensitive sensors. This approach has been demonstrated on silicon pin diodes. In the case of diamond, excessive radiation damage can increase conductivity which may be of interest for the production of diamond based devices. The microbeam method has been successfully utilized to produce buried conductive lines in single crystal diamond.

A technique for the production of ion tracks using heavy ion beams from a 6.0 MV Tandem accelerator has been developed at the Ruđer Bošković Institute and tested on polymer materials and other materials of technological interest (such as SrTiO_3). Cl and I ion beams of energies above 18 MeV have been used. Implantation of lower energy ions such as carbon between 800 and 2000 keV has been also performed, using both broad and micro beam in order to form nano-diamonds in SiO_2 .

FORMATION OF FERRO-, PARA- AND SUPERPARAMAGNETIC NANOSTRUCTURES BY ION BEAM TREATMENT OF MATERIALS

A variety of metal-carbon nanocomposite thin film materials has been synthesized using low energy ion beam deposition and reactive magnetron sputtering. The evolution of phase formation and film morphology has been investigated using ion beam analysis techniques in

combination with electron microscopy, Mössbauer spectroscopy and optical and magnetic characterization techniques. The investigated nanocomposites with amorphous diamond-like carbon (a-C) as host matrix include non-magnetic systems like a-C:Cu, a-C:Ag as well as ferromagnetic or paramagnetic systems like a-C:Fe and a-C:Ni. The non-magnetic systems like a-C:Cu show interesting optical absorption properties related to surface plasmon effects of the embedded metal nanoclusters. For certain growth conditions self-organized formation of multilayers, consisting of nanocrystalline metal layers separated by a-C with periods of only 10–20 nm is observed. Based on the results, a model that describes the mechanism of self-organized multilayer growth has been developed. The predictions of the model have been confirmed by systematically varying the growth conditions. This study was performed in particular on the a-C:Ni and a-C:Cu systems. The model now predicts the thin film morphology of nanocomposite thin films by considering processes such as sub-surface cluster formation, diffusion, surface segregation and sputtering, taking place simultaneously during film growth. Homogeneous metal-carbon nanocomposite materials with ultra-small nanoclusters <3 nm embedded in a-C or DLC matrices have also been successfully produced. These materials may be useful for tribological and optical applications, and also as biocompatible coatings (a-C:Ag).

The systems a-C:Fe and a-C:Ni displayed paramagnetic behaviour due to the small size and the spatial separation of the metal particles. In order to investigate the possibility to modify the magnetic properties of such nanoscopic systems, a series of experiments was initiated with the aim of imprinting an in-plane uniaxial magnetic anisotropy by generating a shape anisotropy of the film surface. This shape anisotropy was created by ion beam sputter erosion, which resulted in nanoscale surface ripple patterns. The ripple patterns were found to introduce a pronounced uniaxial magnetic anisotropy in nanocrystalline Fe thin films. The magnitude of the anisotropy was quantitatively determined (25–100%) as well as the size of the surface region (≈ 12 nm) that is influenced by the shape anisotropy due to the ripple pattern. The synthesis of magnetically anisotropic Fe nano-wires on glass and Si substrates was also achieved. Ion implantation of ^{57}Fe in a range of substrates has been carried out; the results of Mössbauer measurements are presented. The studies will be further extended to nanocomposite systems.

FORMATION OF MAGNETIC NANOSTRUCTURES AND COMPLEXES BY ION IMPLANTATION OF Fe INTO SUITABLE SUBSTRATES

The aim of the project was to investigate the conditions required to achieve the formation of magnetic nano-clusters by ion implantation of Fe into suitable host matrices. Related investigations were also undertaken on magnetic complex formation in ZnO and other oxides following implantation of short lived ^{57}Mn ($T_{1/2} = 1.45$ min), in research collaborations with the Mössbauer group at the ISOLDE Facility at CERN.

^{57}Fe was implanted into host matrices ZnO, 3C-SiC, SiO₂, CVD diamond and graphite, to fluences of up to $2 \times 10^{16}/\text{cm}^2$ at the Göttingen ion implanter. Characterization by means of RBS and UV-VIS optical transmission measurements showed redistribution of the implanted ions on annealing. In the search for magnetic cluster formation, Mössbauer spectroscopy (MS) was used as the main characterization technique. Transmission MS measurements were performed on the SiC samples at room temperature (RT) and 80K, the change in the MS spectra suggested formation of magnetic assemblies with Curie temperatures below RT. Conversion electron MS (CEMS) measurements at RT were performed on ^{57}Fe -implanted ZnO and SiC samples after annealing the samples up to 1073K. In ZnO, the Fe^{3+} ions remain

essentially unchanged with annealing; the Fe^{2+} ions showed a redistribution, but there was no evidence of any magnetic ordered component with implantation fluence of $2 \times 10^{16} \text{ }^{57}\text{Fe}/\text{cm}^2$, which is two orders of magnitude below that at which the effect has been observed. The MS spectra of 3C-SiC showed more promise, with evidence of structure additional to that observed with extremely low fluence implantation.

The measurements showed that MS spectra of good statistics can be obtained with implanted fluences of $5 \times 10^{15} \text{ }^{57}\text{Fe}/\text{cm}^2$, and thus allowing for a more systematic study with higher fluence implantation of ferromagnetic (FM) and non FM ions.

Complementary investigations were undertaken in research collaborations on Mössbauer spectroscopy following implantations of low fluence radioactive ions. Mössbauer measurements were performed on 3C-SiC, CVD diamond, and ZnO following implantation of 60 keV $^{57}\text{Mn}^*$ ions which decay to the 14.4 keV Mössbauer state in $^{57}\text{Fe}^*$. Interstitial and substitutional Fe in SiC and CVD diamond were identified in the MS spectra and information obtained on the annealing of implantation induced damage, and on diffusion of interstitial Fe in SiC. In the ZnO sample, clear evidence was found for magnetic order being established at RT and above. The magnetic effect was found to disappear at $T > 600\text{K}$, pointing to a vacancy associated mechanism, most likely the formation of Fe-V-O complexes, which result in the observed behaviour.

ION IMPLANTATION DOPING OF SrTiO_3

This project aimed to investigate the possibilities for ion implantation doping of perovskite oxides and related materials in order to modify their optical, magnetic and electrical properties.

The systems which were studied were single-crystalline samples of SrTiO_3 ion implanted with various potential magnetic, electrical and optical dopant elements at widely differing fluences. Among the analysis techniques used were nuclear techniques such as Perturbed Angular Correlation spectroscopy, and, in particular, the ion beam techniques of emission channelling and Rutherford backscattering/channelling.

Low-fluence (10^{12} – 10^{14} cm^{-2}) implantations of 60 keV ions were used to create buried layers in, which are located several 10 nm below the surface, are of similar thickness, and contain dopant atoms below the per cent range. In addition, by means of high-fluence implantations (60 keV, 10^{15} – 10^{16} cm^{-2}) of Fe, also near-surface layers were produced where the Fe atom concentration reaches levels of 2–20%, and where new Fe-rich phases are certainly present inside the material. In this case the modification of the magnetic properties of the samples was directly measured by means of a superconducting quantum interference device.

One of the major findings is that the annealing temperature for effective recovery of implantation damage in SrTiO_3 is around 1000°C , which is much higher than the 400°C recrystallization temperature of amorphous SrTiO_3 reported in the literature. The second major finding is that most of the implanted foreign atoms in SrTiO_3 (with the exception of Fe) behave in an amphoteric way, i.e. they partially substitute for Sr and Ti, which complicates site-specific doping attempts in this material. Besides the chemical properties the ionic size seems to be a decisive factor in determining the preferred lattice position. The possibility to produce ferromagnetic SrTiO_3 by means of Fe implantation was demonstrated for the first time.

MICROSTRUCTURAL CHANGES INDUCED BY ION BEAM MODIFICATION OF SPUTTERED METAL NITRIDE FILMS

Single and multilayered CrN, TiN and AlN thin film structures deposited on Si substrates, as well as pure metallic Al/Ti multilayers, of thicknesses of 240–280 nm were irradiated with 120–200 keV Ar⁺ ions to the fluences ranging from 1×10^{15} to 4×10^{16} ions/cm². The metallic multilayered structure was also irradiated with high fluence ($1\text{--}2 \times 10^{17}$ /cm²) nitrogen ions at 200 keV, in order to study interface mixing and formation of nitrides.

Single component CrN and TiN thin films were found to grow in the form of very fine polycrystalline columnar structures. The individual columns stretched from the substrate to the surface, while their lateral dimensions were of the order of a few tens of nm. The films deposited at an elevated substrate temperature of 150°C grow in the form of larger crystal grains (i.e. wider columns) compared to those deposited at room temperature. The chemical composition of the Cr-N and Ti-N films were identified as CrN or Cr₂N (depending on the nitrogen partial pressure during deposition) and as stoichiometric TiN, respectively. After ion irradiation the layers retain their polycrystalline structure, although modified. The columns become disconnected, and the resulting structures consist of larger grains and nano-particles of the same phase. The results of electrical resistivity measurements are consistent with those of the structural analysis. The films grown at an elevated substrate temperature have a lower electrical resistivity, due to larger mean grain size and a lower concentration of grain boundaries. Implanted samples have a higher electrical resistivity due to a higher concentration of point defects and the presence of nano-particles, despite the net increase of lateral size of the grains for higher implanted fluences.

In the case of Al/Ti and AlN/TiN multilayers irradiated with Ar ions, markedly different behaviour was observed. The as-deposited structures exhibit well-defined, isolated polycrystalline Al and Ti, or AlN and TiN layers, with sharp interfaces. In the metallic system ion irradiation was found to induce interface mixing, which progressed with increasing ion fluence. Formation of intermetallic phases for the highest fluence of 4×10^{16} ions/cm² was observed. Reactions were most pronounced at the interfaces that are located around the projected ion range. The multilayered structure was essentially preserved, but individual layers had a graded composition. The implanted samples exhibit much larger crystal grains, and the formation of lamellar columns is observed stretching over a number of individual layers. In contrast to the Al/Ti system, the AlN/TiN multilayered structures exhibit remarkable ion irradiation stability: no measurable interface mixing was observed at all applied Ar ion fluences. The absence of any intermixing was attributed to the nature of interatomic bonding and to mutual immiscibility of AlN and TiN.

High fluence nitrogen ion irradiation of Al/Ti multilayers results in both the introduction of nitrogen into the structures as well as a high level of their intermixing. The latter effect is assigned to the chemical reactivity of Al and Ti, and is most efficient around the projected ion range. A multilayered structure was preserved consisting of a compositionally graded ternary (Al,Ti)N multilayers, with individual layers being either Al or Ti rich.

ION BEAM SYNTHESIS AND MODIFICATION OF SILICON CARBIDE

The objectives of the project were to investigate, using ion beam synthesis techniques, the formation of a buried crystalline silicon carbide layer in a silicon wafer with technically applicable large area and thickness for high-power microelectronic applications, and to

develop the ion beam synthesis technique of multiple-energy high-fluence carbon ion implantation in silicon wafers followed by either high-temperature thermal annealing or swift heavy ion beam annealing.

Carbon ions have been implanted with both single and multiple energies and with high fluences in silicon wafers at room or elevated temperatures. This has been followed by post-implantation thermal annealing or swift heavy ion beam annealing. Characterization of the implanted carbon depth profile and of the formation and phase of SiC has been undertaken using a range of techniques. Formation of a buried high-quality polycrystalline nano-grained β -SiC layer in a Si wafer has been achieved.

The use of swift heavy ion beams in the annealing process, which has been pioneered in this CRP, is shown to give favourable results. The annealing depends on ion energy and fluence, and annealing of SiC by this method has been achieved.

Neither annealing method results in broadening of the implanted high-concentration carbon profile. This, however, was achieved by multiple-energy C-ion implantation in Si in the energy sequence from high to low energy. Initial chemical etching methods failed to expose the synthesized SiC nanocrystallites for luminescence studies.

OPTIMIZED PRE-AMORPHIZATION CONDITIONS FOR THE FORMATION OF HIGHLY ACTIVATED ULTRA-SHALLOW JUNCTIONS IN SILICON-ON-INSULATOR

The buried oxide layer in the silicon on insulator (SOI) substrates acts as an insulator and as a diffusion barrier in semi-conducting silicon. The effects of dopant (principally B) activation and diffusion in SOI have been studied and compared with the behaviour of the same dopant in bulk silicon. The results show that by carefully tailoring the implantation conditions of the pre-amorphizing implant, the buried oxide layer can act as a sink and a trap for the interstitials released by the end of range (EOR) defect band. In bulk silicon these interstitials migrate towards the silicon surface, where they form boron interstitial clusters and deactivate the boron. In SOI, if the EOR defects are placed close to the buried oxide interface, this becomes the predominant sink rather than the surface and thus the interstitials migrate towards defects. Consequently, significantly less dopant deactivation is observed in SOI when compared to bulk silicon (sheet resistance rises by 80 Ω /sq in SOI compared to over 400 Ω /sq in bulk silicon).

CONCLUDING REMARKS

Ion implantation and ion beam analysis are powerful tools for characterization and modification of materials by means of bombarding solids with energetic ions. Although the techniques have been highly developed during the past half century, they face new challenges as material processing approaches the nanometer scales. Thus, the overall objective of this CRP which was to facilitate applied, innovative R&D efforts utilizing low energy accelerators for studying material characteristics, developing appropriate techniques and synthesis of novel materials is perfectly in line with the nanoscience research.

The report confirms the work which took place during the RCMs in South Africa and Thailand and allowed for exchange of ideas, lively discussions of research results and exploration of partnerships. The results presented emphasized:

- the versatility of ion beam techniques in material modification and characterization;
- the increasingly important role that the ion beam techniques can continue to play in materials technology development;
- the successful training of young researchers, especially from developing countries. Generally the projects achieved their objectives, in some cases they did not due to ambitious goals or extraneous factors.

The CRP was particularly successful in facilitating the exchange of knowledge and experience, initiating research programmes that will continue into the future, and in spawning new research ideas in ion beam applications. In particular, with regard to developing Member States, the CRP has resulted in novel applications of ion beam methods which had not been explored before. Closer collaboration between developed and developing Member States has been strengthened and will continue beyond the lifetime of the CRP. Successful joint workshops have been held, several exchange visits between participants took place, and co-authored publications were presented at international conferences.

ION BEAM MODIFICATION OF POLYMER SURFACES

T. Tsvetkova and S. Balabanov

Institute of Solid State Physics, Bulgarian Academy of Sciences, Sofia, Bulgaria

Abstract. Ion implantation of polymers results in modification of various properties of the polymer material. Relatively low doses of silicon (Si^+) ion implantation yield interesting photoluminescence (PL) properties modification, like emergence of ultra-violet range PL in some polymers, and appearance of photoluminescence enhancement (PLE) effect in others. These effects have been interpreted as due to the emergence of new PL sites resulting from the presence of Si and/or SiC based clustering in the implanted polymer surface. Evidence for such clustering is supplied by the results of IR and Raman spectroscopy, as well as by SEM studies of the implanted materials and Si elemental analysis. High doses silicon implants are particularly effective for the creation of such Si and SiC cluster networks, as suggested by infra-red (IR) and Raman spectroscopy, as well as by microhardness measurements. The ion beam induced structural modification of the implanted polymer materials has been also analysed using Auger and X ray photo-electron spectroscopy (XPS) studies.

1. INTRODUCTION

Polymer materials are currently used extensively because of their excellent materials properties, like high optical clarity, low attenuation and weathering ability, etc., and are more and more sought for their electronic properties. The attractive materials properties, combined with relatively low cost of production, have led to their widespread use in the manufacture of microwave, electronic and photonic systems [1]. This use is largely attributed to the ease of processing and tailoring their properties to suit a wide range of applications.

In recent years there has been a growing interest towards the modification of surfaces and thin layers of polymers. Ion beam technique is widely used as a flexible and powerful tool for different materials surface engineering, including polymers. The increased attention in the ion implantation of polymer materials is due to the possibility of precise control of the technological parameters for fundamental research purposes, and also considering some possible applications to device fabrication. The ion irradiation of polymers causes various processes, such as: macro-molecular destruction, cross-linking, free radicals formation, carbonization and oxidation [2][3][4]. The understanding of certain structural re-arrangements influence on the suitable properties of polymers opens a way to design devices with required parameters, involving such applications as optical filters, absorbers, reflectors, etc.[5][6][7]. The optical properties of ion implanted polymers, being of particular interest for modern optoelectronics and photonics, have been extensively explored [8][9].

Extending the understanding of the ion beam induced structural re-arrangements effect on the relevant optical properties of polymer materials reveals new approaches to the design of devices with desired parameters, and leads to the development of high-performance polymers applications in different optical elements and luminescent devices [10].

The aim of the present work has been to apply the ion implantation technique in some prospective polymer materials to produce ion beam synthesized (IBS) silicon carbide (SiC) protective and functional layers by relatively high-doses Si^+ implantation. Lower doses are used aiming to produce Si and SiC ultra-fine particles, embedded in polymer matrices and

yielding interesting luminescence and other material properties. Both developments are expected to reveal new perspectives for the fundamental research and applications of polymers modern optoelectronics and photonics.

2. EXPERIMENTAL PROCESSING

Samples of different polymer materials, commercially available as bulk samples with thickness of 2 mm, were studied in the present work: polymethylmethacrylate (PMMA), polypropylene (PP), poly-tetrafluor-ethylene (Teflon), ultra-high-molecular-weight-polyethylene (UHMWPE). All studied polymer materials are shaped as squares (side of 10 mm) or circles (diameter of 10 mm).

Ion implantation with Si⁺ was performed at room temperature (RT) and relatively low energies ($E = 30\text{--}50$ keV), with ion doses ranging from $D = 1 \times 10^{13}$ to $D = 1.2 \times 10^{17}$ cm⁻², using Danfysik 1090 implanter. In order to keep the target temperature lower than 80°C, at which the polymer can be decomposed, the beam current was kept under 2 μA/cm². The pressure in the target chamber was kept under 10⁻⁶ Pa during implantation. Additionally, an implantation by carbon ions was undertaken at $E = 30$ keV and $D = 10^{13}\text{--}10^{15}$ cm⁻², as well as by Fe⁺ and Ga⁺. The aim was to distinguish the Si⁺ implants induced effects from those introduced by self-ion implantation (C⁺) or by ions of other chemical elements.

The implanted samples were characterized optically by optical transmission and photoluminescence (PL) measurements. Structural characterization of the implanted polymer samples was carried out by Raman and infra-red (IR) spectroscopy measurements. Auger electron spectroscopy (AES) and X ray photoelectron spectroscopy (XPS) measurements were employed to investigate the in-depth structural modification of the implanted polymer materials.

The ion beam induced surface properties modification of the implanted polymer materials was studied with micro-hardness measurements, using Knoop indentation method, and elemental X ray microanalysis and surface morphology analysis, using SEM measurements.

3. RESULTS AND DISCUSSION

3.1. *Modification of photoluminescence properties*

3.1.1. *UV range PL emission*

Figure 1 (left) shows the PL spectra for Si⁺ implanted UHMWPE samples [11]. For PL excitation an N₂ laser ($\lambda_{\text{ex}} = 337$ nm) was used and the PL spectra were measured in the range 350–650 nm. The Si⁺ ion implantation results in PL quenching in the whole visible range of the spectrum, while emergence of an UV range ($\lambda \sim 350$ nm) PL signal is observed, increasing with the dose. No such UV range PL effect is found for the case of C⁺ implantation in the same polymer material (UHMWPE), as shown in Fig. 1 (right). Instead, here only visible range PL is registered, with C⁺ implantation resulting just in its modification in the same range. The observed PL spectral changes in the case of Si⁺ implanted UHMWPE, and the UV range emission emergence in particular, could be originating from Si⁺-related defect complexes [7]. More research is needed to clarify the nature of the PL spectral changes introduced by the Si⁺ implants in UHMWPE.

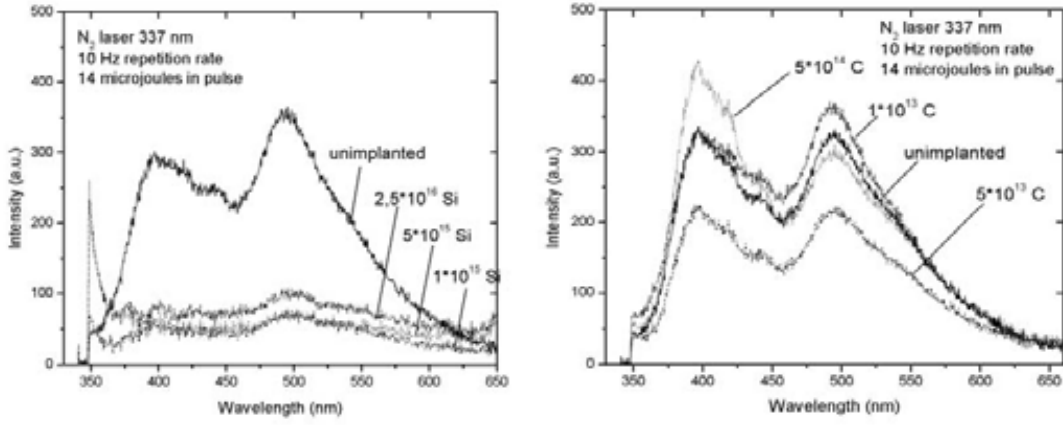


FIG. 1. PL ($\lambda_{ex} = 337$ nm) from Si^+ (left) and C^+ (right) implanted UHMWPE samples for ion beam energy $E = 30$ keV.

3.1.2. Visible PL enhancement (PLE)

A considerable PLE effect has been observed for the PMMA samples implanted by Si^+ ion implantation (Fig. 2). Here the PL is excited by UV light ($\lambda_{ex} = 272$ nm) and recorded under identical experimental conditions for all seven PMMA samples treated by seven Si^+ ion doses in the range $D = 10^{14}$ – 10^{17} cm^{-2} . The PL data for a reference sample ($D = 0$) is also given in this figure for comparison. A possible mechanism for the observed PLE in both cases is ion beam induced increased cross-linking and a higher degree of ordering in the polymer structure [12].

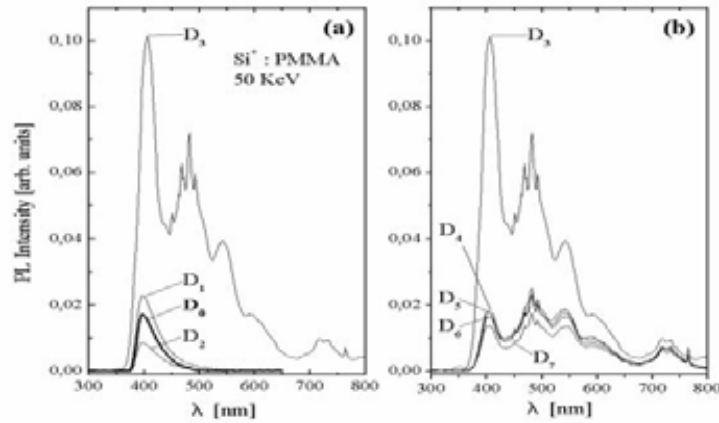


FIG. 2. PL ($\lambda_{ex} = 272$ nm) from Si^+ implanted PMMA at ion beam energy $E = 30$ keV and implantation doses: $D_1 = 1 \cdot 10^{14}$; $D_2 = 3.2 \times 10^{14}$; $D_3 = 1 \times 10^{15}$; $D_4 = 3.2 \times 10^{15}$; $D_5 = 1 \times 10^{16}$; $D_6 = 3.2 \times 10^{16}$; $D_7 = 1 \times 10^{17}$ cm^{-2} ; D_0 unimplanted PMMA.

As seen in Fig. 2, the PL of implanted PMMA at certain doses is more intensive than the one for the unimplanted PMMA — over 5 times increase for $D = 10^{15}$ cm^{-2} — and further increase of the implantation dose results only in PL intensity decrease (Fig. 2b). Considerable changes in the PL spectra are also evident. The broad valence band of PMMA at ~ 395 nm is modified to a relatively narrow and strong luminescence band at ~ 405 nm with FWHM ~ 50 nm. Additional spectral bands also appear around 480 nm, 545 nm, and 600 nm. These spectral features are preserved up to the highest dose available ($D = 10^{17}$ cm^{-2}).

A reasonable explanation for these spectral changes is the formation of new luminescence states, and associated transitions, originating from Si^+ -related defect complexes [7]. At present, the origin of the narrow lines at 570 nm and 660 nm within the PL spectra is not clear, most probably they are artefacts. The PL intensity further decrease with doses higher than $D = 10^{15} \text{ cm}^{-2}$, for this higher energy case, is presumably due to greater degree of energy dissipation, resulting in increased defect introduction and related process of degradation of the polymer structure. More research is needed to clarify the nature of the PLE in this case.

3.2. Optical properties

3.2.1. Visible range optical properties

A gradual increase in optical absorption with the dose is registered for Si^+ implanted PMMA samples with different ion doses ($D = 1 \times 10^{13} \div 2.5 \times 10^{16} \text{ cm}^{-2}$), as seen in Fig. 3 [13]. In this case, a noticeable absorption increase is observed at a relatively low dose ($D_4 = 1 \times 10^{15} \text{ cm}^{-2}$), followed by a continuous increase gradually with the dose, without reaching a saturation. The origin for this absorption increase is further revealed in the following results of IR, Raman, Auger, XPS and SEM measurements.

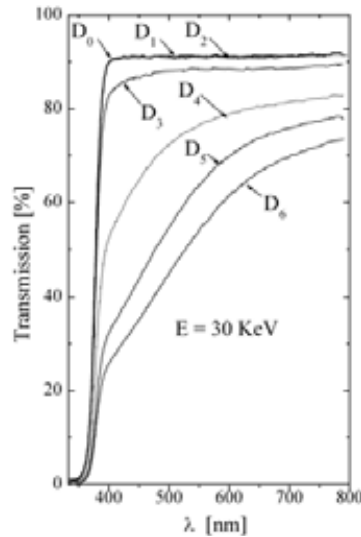


FIG. 3. Optical transmission spectra of Si^+ implanted PMMA samples at ion beam energy $E = 30 \text{ keV}$ and different ion doses: $D_1 = 1 \times 10^{13}$; $D_2 = 5 \times 10^{13}$; $D_3 = 2.5 \times 10^{14}$, $D_4 = 1 \times 10^{15}$; $D_5 = 5 \times 10^{15}$; $D_6 = 2.5 \times 10^{16} \text{ cm}^{-2}$; D_0 —unimplanted PMMA.

3.2.2. Infra-red (IR) spectroscopy results

In Fig. 4 the IR spectra of Si implanted and reference PMMA samples are compared. A wide variety of SiC phonon band profiles can be observed depending on the growth conditions. The frequencies of the transversal optical (TO) phonons for the different *polytypes* in which the material crystallize are close and lies in the range $766\text{--}780 \text{ cm}^{-1}$ [14]. Thus the feature at 780 cm^{-1} in the spectrum of the implanted sample can be related to the SiC fundamental phonon absorption. The noticeable feature at 740 cm^{-1} may be due to morphological factors as grain size and shape as well as to plasmon-phonon coupling [15]. Low intense features at 610 and 1080 cm^{-1} in the spectrum of the implanted sample, marked with arrows in Figure 1, then can be attributed to the absorption of unreacted Si atoms [16].

The comparison of the experimental transmittance spectra displayed in Fig. 4 shows unambiguously an increase of the absorption of the implanted sample in the range between 1300 and 1600 cm^{-1} , which is an indication for the presence of graphitic amorphous carbon [17].

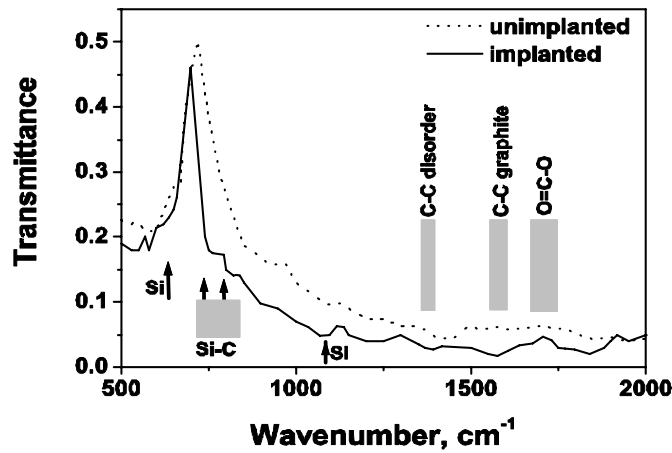


FIG. 4. IR spectra of Si^+ implanted ($E = 30 \text{ keV}$, $D = 5 \times 10^{16} \text{ cm}^{-2}$) and reference PMMA samples.

3.3. Raman spectroscopy measurements

In Fig.5 the Raman spectra of Si implanted and reference samples are shown in the range from 200 to 2000 cm^{-1} . Because of the low scattering volume of the implanted region no significant difference between the two spectra is seen. The only unambiguous statement concerns the increase of the scattered light intensity in the range about 1550 cm^{-1} , shadowed in Fig. 5. The subtraction of unimplanted sample spectrum from the implanted sample one gave the result, displayed in the inset of Fig. 2. It is seen that the difference in the spectra is governed by a broad band peaked at about 1550 cm^{-1} . The spectrum in the inset looks like the spectrum of a net-work with graphitic sp^2 hybridized C bonds; see for example [18].

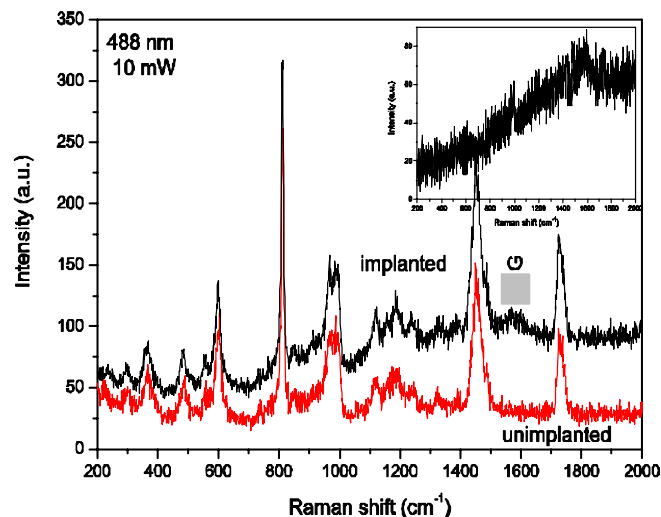


FIG. 5. Raman spectra of Si^+ implanted ($E = 30 \text{ keV}$, $D = 5 \times 10^{16} \text{ cm}^{-2}$) and reference PMMA samples.

3.4. Micro-hardness measurements

The presence of Si and SiC clustering, together with the graphitic carbon network, as suggested by results of the IR and Raman spectroscopy measurements, are also revealed by the results of the micro-hardness measurements (Table 1):

3.5. AES and XPS results

Auger electron spectroscopy (AES) and X ray photoelectron spectroscopy (XPS) results give experimental data about the in-depth distribution of the implanted Si atoms and associated structural modification.

Table 1. Dose dependence of micro-hardness for Si^+ implanted UHMWPE and PMMA samples at $E = 30 \text{ keV}$ and different doses.

Si^+ dose [cm^{-2}]		unimplanted	1×10^{13}	1×10^{15}	1×10^{17}
Micro-hardness [MPa]	UHMWPE	24.5	52.0	61.1	77.4
	PMMA	33.2	50.4	51.3	71.5

Table 2. Table of medium projected ranges R_p and straggling ΔR_p for Si^+ implanted in different polymers with $E = 30 \text{ keV}$ [19].

Material	UHMWPE	PMMA	Teflon
R_p [nm]	65	63	44
ΔR_p [nm]	14.5	16.5	15

In Fig. 6 the AES results for the in-depth distribution of Si (at%) for a Si^+ implanted UHMWPE sample is presented, showing the typical in-depth peak of the Gaussian distribution situated at some distance from the surface. At the same time, very interesting behaviour of the Si distribution is observed closer to the surface where, going through a minimum, a very high Si concentration is again registered at the top surface.

In Fig. 7 the XPS results are given for the $\text{Si}2p$ and $\text{Si}2s$ in depth spectra of a Si implanted UHMWPE sample. The depth profiling was carried out by sputter etching at 90° using a defocused Ar^+ ion beam. A considerable peak of Si concentration in the implanted polymer material is observed at some distance from the surface in conformity with the Gaussian distribution of the implanted Si ion ranges in the target material.

3.6. Scanning electron microscopy (SEM) analysis results

SEM results of Si elemental analysis of the implanted polymer surfaces show presence of Si clustering, increasing in density with the ion dose [20]. In order to define the form and size of the clusters, additional transmission electron microscopy (TEM) experiments will be needed.

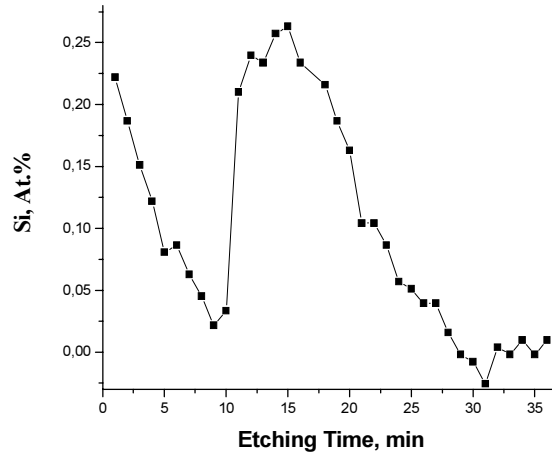


FIG. 6. AES data for in-depth distribution of Si (at%) for a Si^+ implanted UHMWPE sample with ion energy $E = 30 \text{ keV}$ and dose $D = 1.2 \times 10^{17} \text{ cm}^{-2}$.

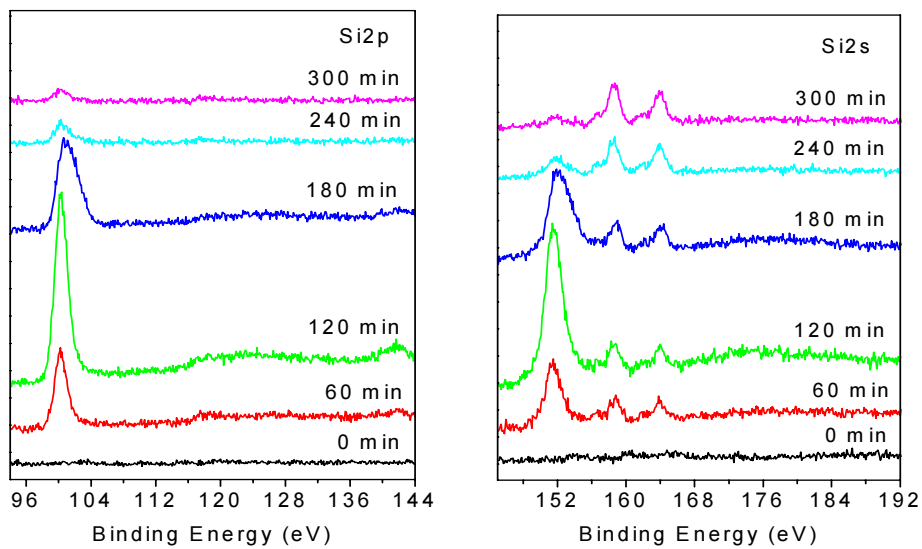


FIG. 7. XPS spectra of Si2p and Si2s electrons of a Si implanted UHMWPE sample ($D = 10^{17} \text{ cm}^{-2}$).

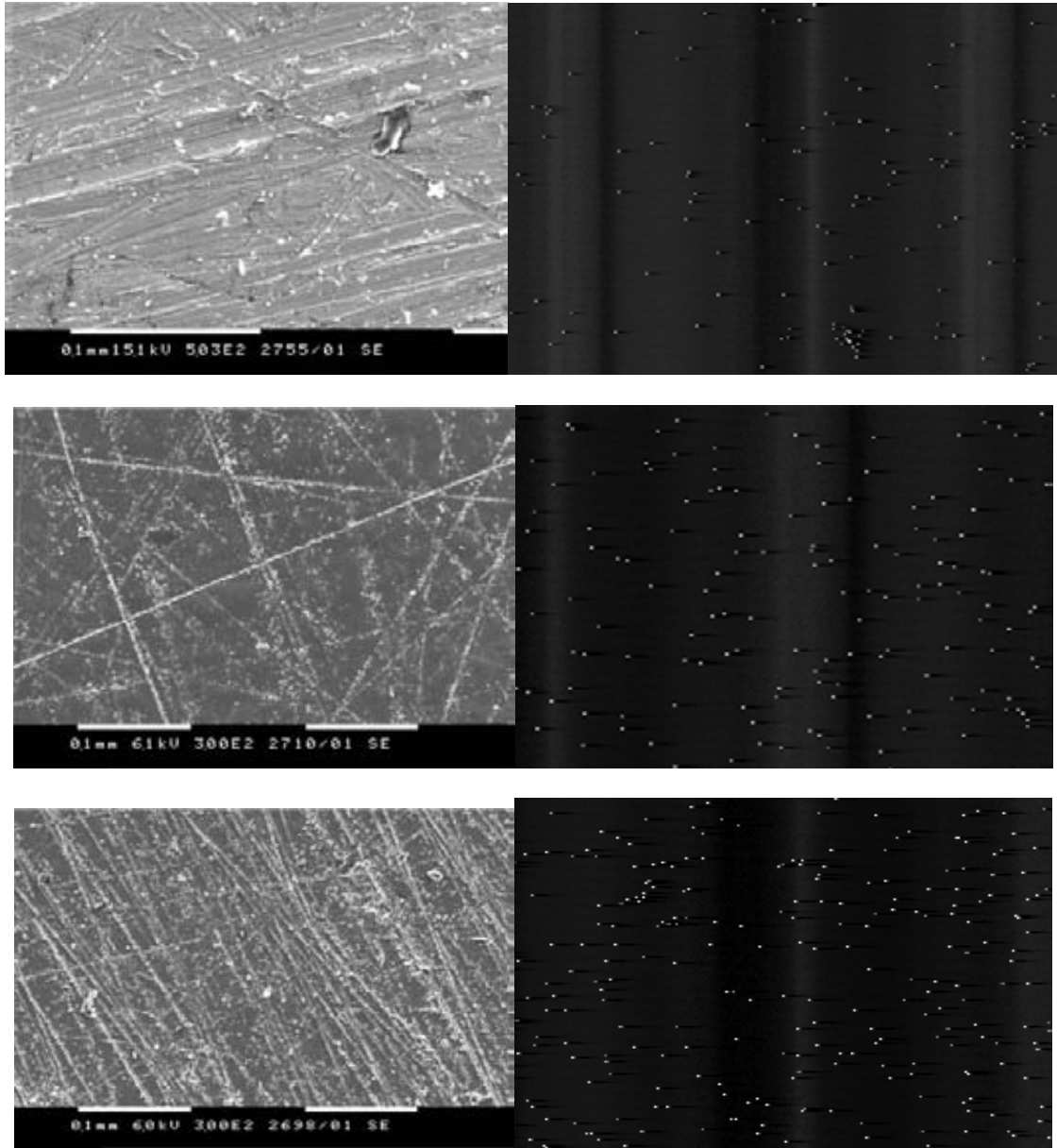


FIG. 8. Analysed surface morphology of PMMA samples, implanted with different Si⁺ ion doses: $D_2 = 5 \times 10^{15} \text{ cm}^{-2}$ (top left), $D_3 = 2.5 \times 10^{16} \text{ cm}^{-2}$ (middle left) and $D_4 = 1.2 \times 10^{17} \text{ cm}^{-2}$ (bottom left); and results of Si elemental analysis for the same samples: $D_2 = 5 \times 10^{15} \text{ cm}^{-2}$ (top right), $D_3 = 2.5 \times 10^{16} \text{ cm}^{-2}$ (middle right) and $D_4 = 1.2 \times 10^{17} \text{ cm}^{-2}$ (bottom right). Magn. 500x. Scanning electron microscopy.

4. CONCLUSIONS

Silicon ion implantation in polymers results in modification of various properties of the polymer material. Relatively low doses yield interesting photoluminescence properties modification, like emergence of UV range PL in UHMWPE, and appearance of photoluminescence enhancement (PLE) effect in PMMA. These effects could be related to the emergence of new PL sites resulting from the presence of Si and/or SiC based clustering in the implanted polymer surface. Evidence for such clustering is supplied by the results of IR and Raman spectroscopy, as well as by SEM studies of the implanted materials and Si elemental analysis. In order to define the form and size of the clusters, additional TEM experiments are in run. High doses silicon implants are particularly effective for the creation of such Si and SiC cluster networks, as suggested by IR and Raman spectroscopy, as well as by micro-hardness measurements. Possible increase of this effectiveness for the lower doses, which would increase also the cost effectiveness of the method, could be sought by different post-implantation processing of the implanted polymer materials, especially by low temperature methods like γ ray irradiation, which was not available in our institution during the time of the present research.

ACKNOWLEDGEMENTS

The authors would like to thank IAEA for accepting and financing this study as well as for coordinating the CRP in a very successful manner.

REFERENCES

- [1] FRANK, W.F.X., SCHOESSER, A., STELMASZYK, A., SCHULZ, J., *Polymers in Optics, Physics, Chemistry and Applications*, eds. R.A.Lessard and W.F.X.Frank, SPIE Optical Engineering Press (1996) p. 65.
- [2] LÜCK, H.B., *Mechanism of particle track etching in polymeric nuclear track detectors*, Nucl. Instrum. Methods 202 (1982) 497.
- [3] POPOK, V.N., ODZAEV, V.B., KOZLOV, I.P., AZARKO, I.I., KARPOVICH, I.A., SVIRIDOV, D.V, *Ion beam effects in polymer films: Structure evolution of the implanted layer*, Nucl. Instrum. Methods B 129 (1997) 60.
- [4] BALABANOV, S., KREZHOV, K., *Electrical conductivity and electrical properties of radiationally modified polymer composites with carbon black*, J. Phys. D 32 (1999) 2573.
- [5] VARGO, T.G., et al., *Surface Characterization of Advanced Polymers*, eds. L. Sabbattini and P.G. Zamboni, VCH Publ. Co., Weinheim (1993) p.163.
- [6] SLOOF, L.H., VAN BLAADEREN, A., POLMAN, A., HEBBINK, G.A., KLINK, I.S., VAN VEGGEL, F.C.J.M., HOFSTRAAT, J.W., Appl. Phys. Lett. 91 (2002) 3955.
- [7] YU, Y.H., et al., *Ion Implantation Technology — 2000*, eds. H.Ryssel et al., IEEE, (2000) p.765.
- [8] STEPANOV, A.L., *Optical Properties of Metal Nanoparticles Synthesized in a Polymer by Ion Implantation: A Review*, Tech. Phys. 49 (2004) 143.
- [9] TOWNSEND, P.D., CHANDLER, P.J., ZHANG, L., *Optical Effects of Ion Implantation*, Cambridge Univ. Press (1994).
- [10] SLOOF, L.H., et al., *Rare-earth doped polymers for planar optical amplifiers*, J. Appl. Phys. 91 (2002) 3955.

- [11] TSVETKOVA, T., BALABANOV, S., AVRAMOV, L., BORISOVA, E., ANGELOV, I., BISCHOFF, L., *Photoluminescence of Si⁺ and C⁺ implanted polymers*, Vacuum, 2008, in press.
- [12] CHARLESBY, A., *Atomic Radiation and Polymers*, Pergamon Press, Oxford (1960).
- [13] TSVETKOVA, T., BALABANOV, S., BORISOVA, E., AVRAMOV, L., ZUK, J., BISCHOFF, L., *Optical properties of Si⁺ and C⁺ implanted polymers*, Proc. IX Int. Conf. on Laser and Laser-Information Technologies, Oct.4–7 (2006) Smolyan, Bulgaria, p.201.
- [14] FREITAS, JR. J.A., *Properties of Silicon Carbide*, ed. G.L. Harris, EMIS Datareviews Series 13 (1995) 29.
- [15] MUTSCHKE, H., ANDERSEN, A.C., CLEMENT, D., HENNING, T., PEITER, G., *Infrared properties of SiC particles*, Astron. Astrophys. 345 (1999) 187.
- [16] COLLINS, R.J., FAN, H.Y., *Infrared Lattice Absorption Bands in Germanium, Silicon, and Diamond*, Phys. Rev. 93 (1954) 674.
- [17] NAKAYAMA N., TSUEHIYA Y., TAMADA S., KOSUGE K., NAGATA S., TAKAHIRO K., YAMAGUCHI S., *Structural properties of amorphous carbon nitride films prepared by reactive RF-magnetron sputtering*, Jpn. J. Appl. Phys. 32 (1993) L1465.
- [18] DOYLE, T.E., DENNISON, J.R., *Vibrational dynamics and structure of praphitic amorphous carbon modelled using an embedded-ring approach*, Phys. Rev. B, 51 (1995) 196
- [19] ZIEGLER, J.F., BIRSACK, J.P., LITTMARK, U., *The Stopping and Range of Ions in Solids*, Pergamon Press, Oxford (1985).
- [20] TSVETKOVA, T., BALABANOV, S., AVRAMOV, L., BORISOVA, E., BISCHOFF, L., *Si⁺ implantation induced photolumiscence enhancement in PMMA*, Proc. 5th Int. Conf. “New Electrical and Electronic Technologies”, June 12–15 (2007) Zakopane, Poland, “Przeglad Elektrotechniczny”, ISSN 0033-2097, R. 84 NR3 (2008) 72.

MODIFICATION OF ELECTRONIC PROPERTIES IN INSULATORS USING ION MICROPROBE

**M. Jakšič, M. Karlušič, I. Bogdanovič Radovič,
Ž. Pastuovič, N. Skukan, Z. Medunič**

Ruder Bošković Institute, Zagreb, Croatia

Abstract. Development of techniques that use focused ion beams of MeV energy range for creation of new structures in materials by modifying their properties has been initiated in order to expand application possibilities of ion accelerators at the Ruđer Bošković Institute. In particular we have focused on heavy ions that create significantly larger radiation damage in materials when compared to protons and He ions. Structuring of radiation damage using the ion microbeam in crystalline materials has been developed and tested on silicon and diamond. Application possibilities of created structures came from the fact that radiation damage can decrease charge collection properties in silicon which may be of interest in production of position sensitive sensors. This approach has been demonstrated by creating position dependent response of silicon pin diodes. In the case of diamond, excessive radiation damage can increase conductivity which may be of interest for production of diamond based devices. Buried conductive lines have been produced in single crystal diamond. Additional application that use ion tracks created in different materials by heavy ion beams from 6.0 MV Tandem accelerator has also been developed. Application was first tested on polymers and subsequently on other materials of technological interest (such as SrTiO₃). Cl and I ion beams of energies above 18 MeV have been used in this application. Implantation of lower energy ions such as carbon between 800 and 2000 keV has been performed also, using both broad and micro beam in order to form nanodiamonds in SiO₂.

1. INTRODUCTION

Radiation damage in semiconductors generally deteriorates electronic transport properties of semiconductors. In insulators however, excessive exposure may lead to the formation of conductive regions, as in diamond. The possibility of the Zagreb ion microprobe facility to inject wide range of ion species of various respective energies was therefore utilized for structuring of materials in three dimensions on micrometer levels. Several different techniques have been developed and tested.

- (1) Structuring of radiation damage in silicon was tested on the example of pin diodes that were used as radiation detectors. Radiation damage produced by ion microbeam was utilized to produce simple position sensitive sensors.
- (2) Swift heavy ions are known to be excellent tools for creation of nanometer sized tracks in dielectrics. However, lower energy limit for track formation is not well known and therefore use of smaller accelerators is rather limited. We showed that sub MeV/u energies can be used for track formation in some materials
- (3) Exposure of diamond to focused ion beam can lead to its graphitization above certain dose. We developed technique of using C ion beam to create conductive paths inside the irradiated diamond
- (4) MeV ion implantation has been used to create nanodiamonds when implanted into quartz. Implantation technique as well as ion beam analysis for C ions have been developed

2. FACILITIES AND TECHNIQUES

It is a well known fact that the highest transfer of energy from the fast ion to the stopping material occurs for heavy ions. According to the dependence shown on Figure 1, calculated by SRIM [1], nuclear stopping has its maximum at energies below 100 keV, (nuclear stopping — lower curves), while electronic stopping has its maximum at energies above 1 MeV per nucleon. For the heaviest ions like Cl and I this transfer is larger than 1 keV/nm (for silicon). Such large transfer in both low energy limits and high energy limits can create significant changes in materials. In order to employ this fact for materials modification, new techniques had to be developed while the existing accelerators had to be upgraded.

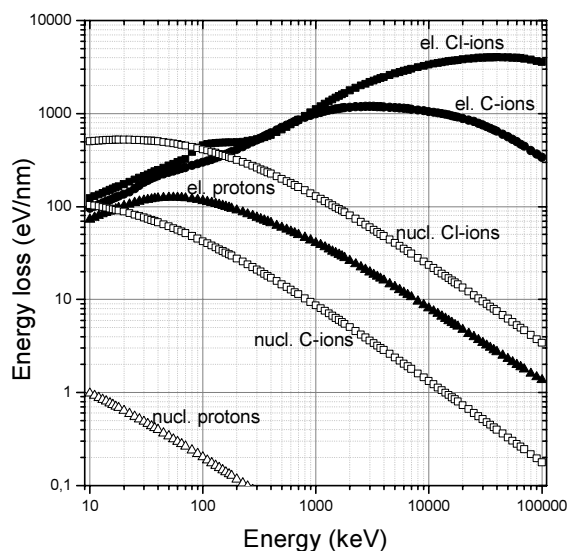


FIG. 1. Energy loss curves (nuclear stopping lower, electronic stopping upper) for protons, C and Cl ions in silicon.

2.1. Accelerator upgrades

Routine operation of the 1.0 MV Tandatron accelerator started in January 2006 after completion of its installation in 2005. During 2006 accelerator was used with voltages ranging from 200 to 1000 kV. Currents of H⁻ ions from the direct extraction duoplasmatron source were typically up to 20 μ A. Analyzed currents of 2 MeV protons are typically in the range between 5 and 15 μ A which results in easily attainable 100–300 pA proton currents in the microprobe chamber. This was a significant improvement, as proton microbeam currents from the large 6.0 MV Tandem accelerator used earlier were never above 20 pA.

Concerning the 6.0 MV Tandem accelerator, it is important to note that, due to the high load by secondary electrons at high voltages and in particular heavy ions, it could be used until 2006 only for light ion beams with voltages up to 4 MV. Conventional accelerating tubes installed at original setup had to be exchanged with new inclined field tubes. This change was performed during April 2006. In spite of the decreased ion beam transmission observed for operations at low terminal voltages, the performance of accelerator has been dramatically increased with significant decrease of secondary electron load and resulting radiation. So far, the maximum useful voltage achieved was 5.5 MV, while the heaviest ion accelerated was iodine.

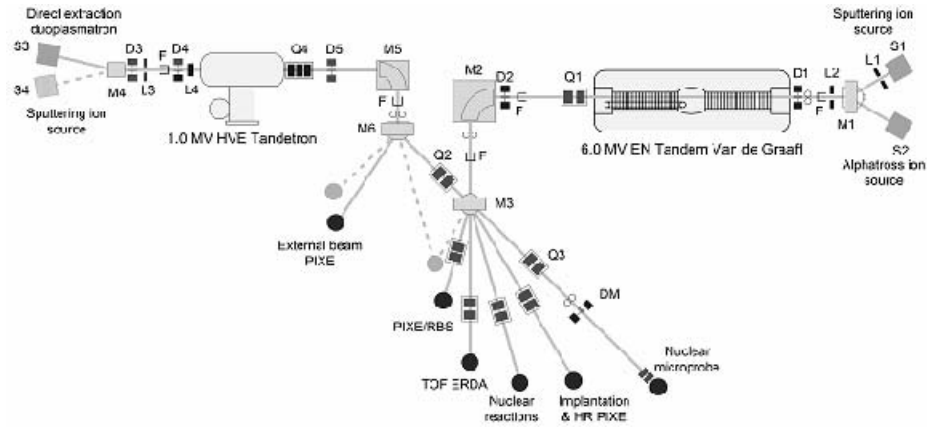


FIG. 2. Layout of the accelerator facility.

2.2. Microprobe focusing upgrade

In order to be able to focus heavy ions of sufficient energy to reach a threshold of creation of latent ion tracks in most of the materials, heavy ions of 1 MeV/u energy are needed. In addition, manipulation of single ions for materials modification application will need better focusing capability than the existing quadrupole doublet.

In order to increase the maximum ME/q^2 as well as demagnification of the microprobe facility, a purchase of additional quadrupoles in order to form quintuplet system according to Ryan design has been started. This system will provide maximum $ME/q^2 \leq 25$ (3 times better) and demagnification of 60×80 (7 times better). So far, only third quadrupole has been mounted which enabled smaller spot size. The best spatial resolution obtained for low currents is 300 nm. Additional quadrupoles needed for quintuplet operation will be installed in 2008 [2]. In addition to improvements of the focusing system, a new scattering chamber has also been installed with several new possibilities and smaller working distance.

2.3. Single ion hit detection

To take a full advantage of swift heavy ions focused down to a micron spot size and their application for ion tracks formation, reliable ion hit detection system has been developed. This system is needed for independent verification of ion penetration into the material. In spite of the rather low efficiency of hit detection for proton beam, an Amptektron MD-502 detector showed close to 100% efficiency for 8 MeV Si ions. The same efficiency is expected to be achieved for ions of greater stopping power. This setup is useful for low current or single ion irradiations where thickness of material exceeds penetration depth of projectile. Results of efficiency tests that have been performed are given in Table 1.

Table 1. Ion hit detection efficiency of CEM detector system.

Ion, energy	dE/dx (keV/nm)	CEM efficiency
H, 2 MeV	0.026	5%
C, 5 MeV	1.16	45%
Si, 8 MeV	2.88	100%

3. APPLICATION RESULTS

3.1. Radiation damage in Si pin diodes

We have fabricated a position sensitive radiation detector by creating radiation damage regions in a Si photodiode. Radiation damage was created in layers at a depth of several μm by ^7Li and ^{16}O ion beams which had energy between 2 and 4 MeV. Ions were focused and scanned using a nuclear microprobe facility. The ion beam induced charge (IBIC) signals created in diodes during irradiation were simultaneously measured to monitor the exact ion beam fluence and analyzed to estimate the amount of defects created. By controlling the ion microbeam scanning system, graduated and position dependent radiation damage was produced in different micro-patterns. Results showed that such patterns can provide information about the position of the interaction between monoenergetic charged particles or photons and the photodiode [3][4].

Our studies have shown that defects created in this way reach stability after approximately one day (see Figure 4). We have also studied the stability and nature of damage created by different ions (protons, Li and O ions of the same range) in silicon. It has been proved that the damage created influence CCE in a way that to a certain extent can be predicted by the NIEL concept. These results will be published [7].

3.2. Single ion tracks

During 2007, the first experiments using chlorine and iodine beams were undertaken in attempts to produce single ion tracks in different materials. All structures created so far were done using the broad beam irradiation; however, the new hit detection system that has been recently installed will enable microbeam irradiation as well.

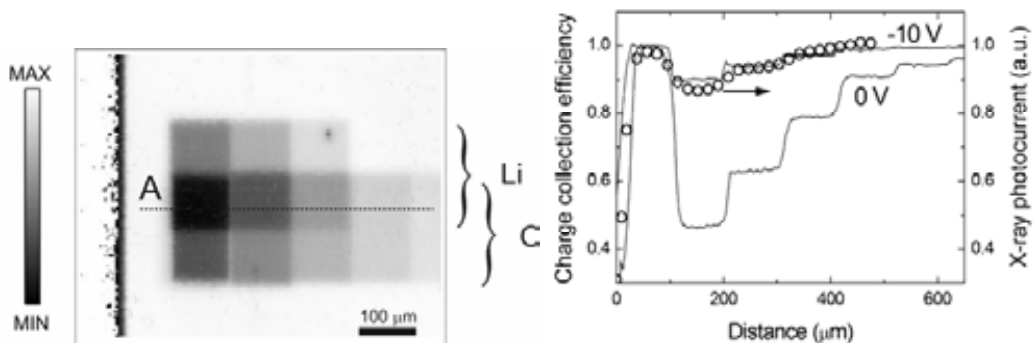


FIG. 3. Pixelated structure (left figure) as measured by 4 MeV ^7Li IBIC. Si photodiode was irradiated with ^7Li (upper), ^{16}O (lower) and both ^7Li and ^{16}O (middle) ions. Reduction of CCE (right figure) recorded along the line A was confirmed by photocurrent measurements during the irradiation by 5.4 keV x ray microbeam.

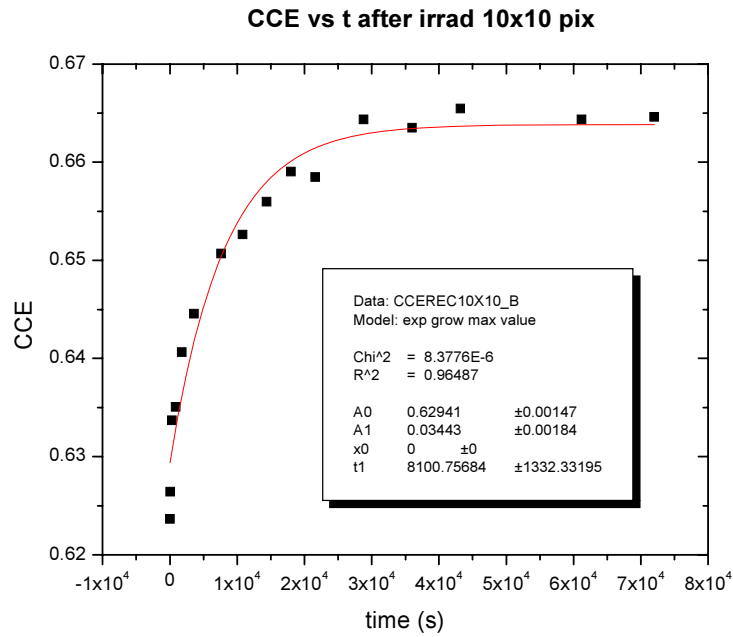


FIG. 4. Stability of ion induced damage (430 keV protons).

3.2.1. Polycarbonate films for fuel cell applications

Thin polycarbonate films were irradiated with 35 MeV chlorine ions. After etching in 6N NaOH + 10% methanol for 5–10 minutes at 400C, pores with 100 nm in diameter were obtained (SEM + AFM). Prolonged etching for two hours resulted in micrometer wide pores that could be observed under optical microscope. Further impedance spectroscopy measurements are planned in near future. Such structures are excellent templates for electrodeposition of metals in the created pores. Nanowires and other structures of high aspect ratios are possible applications of this technique.

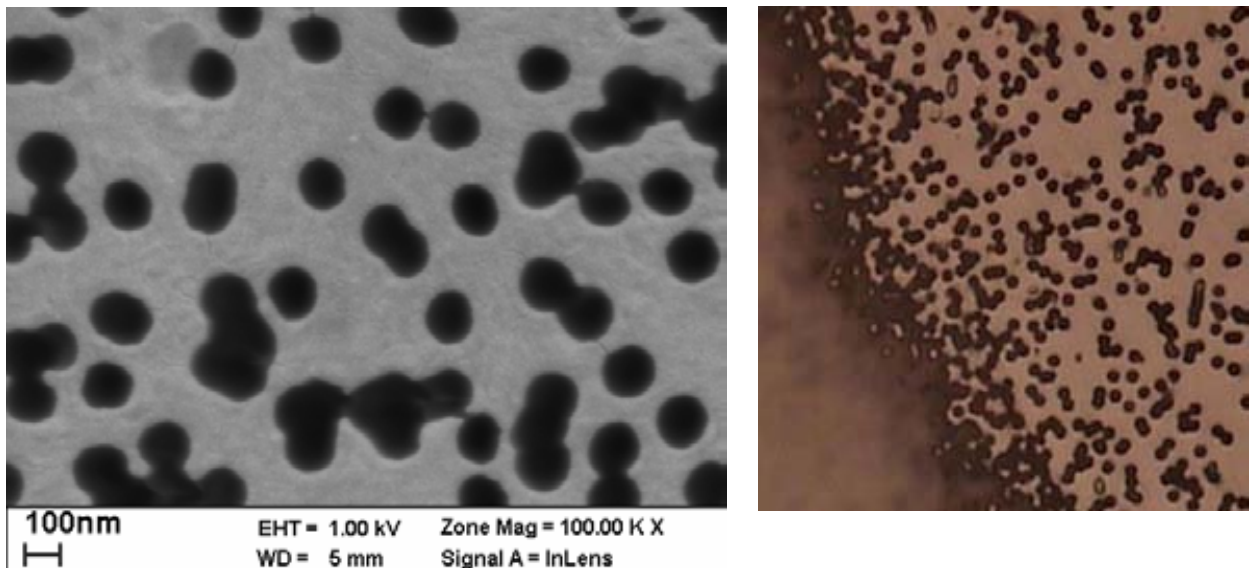


FIG. 5. Etched ion tracks produced by single 35 MeV Cl ions in polycarbonate. SEM image is on left (sample with short etching time), optical image is on right (long etching time).

3.2.2. SrTiO_3 irradiated at grazing angle

A collaboration has been started with Duisburg University, where irradiation with 92 MeV Xe ions under grazing angle (1–5 degrees) has been performed on single crystals of Strontium Titanate (SrTiO_3) [5]. We have repeated the same experiment at lower energies (10–40 MeV) using iodine ions. Sample surfaces were examined using AFM and chains of nanodots resulting from single ion impact were observed in both laboratories. The threshold for creation of such structures was determined to be below 20 MeV ($dE/dx = 7 \text{ keV/nm}$). More precise studies are currently in progress, as well as attempt to measure a nanodot production efficiency curve. Wet HF etching will also be used to study the morphology of nanodot chains.

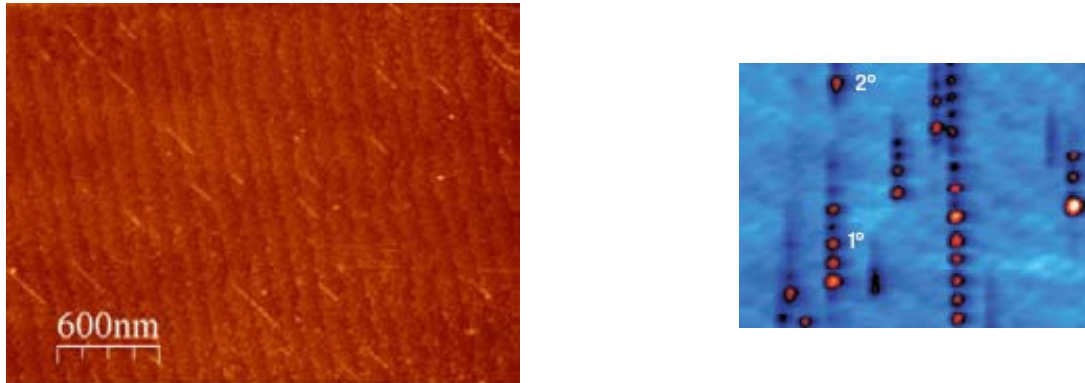


FIG. 6. AFM images of nanodot chains obtained by irradiation of SrTiO_3 .

3.3. Conductive lines in diamond

In recent years, several international laboratories have been engaged in ion beam irradiation to produce structures in diamond [6]. In general, damaged regions were etched away in order to produce optical waveguides. However, if annealing is used instead of etching, it is possible to create graphitic regions that are electrically conductive.

We have started our first experiments in making graphitic conductive lines in diamond that can serve as an interesting building block for future diamond based devices. An example is given in Figure 7.

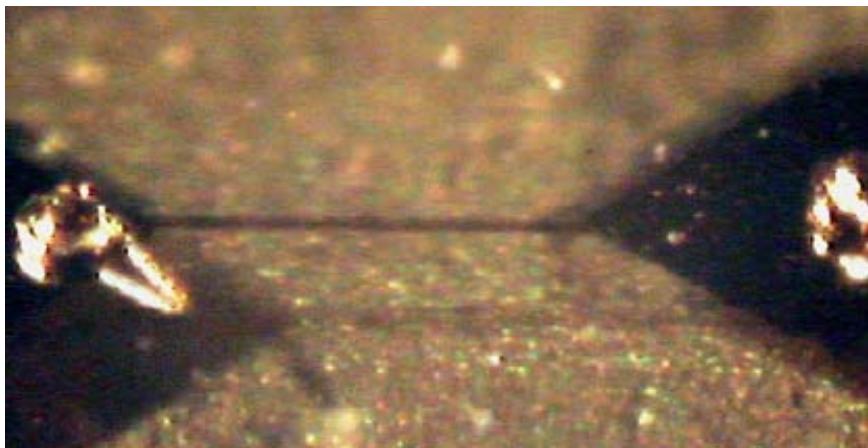


FIG. 7. Graphitization line produced by 6 MeV C ion irradiation of diamond.

3.4. Ion implantation

Implantation of carbon ions into quartz in the energy range between 0.6 and 2.0 MeV has been performed in numerous occasions, both using broad beam as well as microbeam. Samples were annealed using different procedures in order to study processes of nanodiamond formations as well as migration of carbon and hydrogen ions during this process. Several ion beam analysis techniques of depth profiling have been used for characterization. The elastic scattering reaction $^{12}\text{C}(\alpha,\alpha)^{12}\text{C}$ between 3.5 and 4 MeV as well as the strong resonance in $^{12}\text{C}(\text{p,p})^{12}\text{C}$ at 1726 keV were found to have the best capabilities for that purpose.

4. CONCLUSIONS

During the course of this project, experimental capabilities at Zagreb laboratory have been dramatically improved. A new field of research, modification of materials using MeV ion beams, has been initiated. The summary of results presented here are encouraging for the future activities in this field.

ACKNOWLEDGEMENTS

Dr Zvonko Medunić (1963–2006) was the initiator and the first principal investigator of this project. After his graduation at the University of Zagreb, he worked mostly on high temperature superconductors which were also the subject of his PhD thesis which he obtained in 1998. From 2000, he joined Laboratory for ion beam interactions of the Ruđer Bošković Institute where he initiated research of ion beam induced defects in semiconductors and developed a completely novel technique of temperature dependent IBIC measurements. In his too short professional career he published 23 papers. As a brilliant physicist we will miss him as partners in research, as a great person we will all miss him as friends.

REFERENCES

- [1] ZIEGLER J.F., *SRIM-2003*, Nucl. Instrum. Methods B 219-220 (2004) 1027–1036.
- [2] JAKŠIĆ, M., BOGDANOVIĆ RADOVIĆ, I., BOGOVAC, M., DESNICA, V., FAZINIĆ, S., KARLUŠIĆ, M., MEDUNIĆ, Z., MUTO, H., PASTUOVIĆ, Ž., SIKETIĆ, Z., SKUKAN, N., TADIĆ, T., *New capabilities of the Zagreb ion microbeam system*, Nucl. Instrum. Methods B 260 (2007) 114.
- [3] JAKŠIĆ, M., MEDUNIĆ, Z., SKUKAN, N., BOGOVAC, M., WEGRZYNEK, D., *Fabrication of a Si photodiode for position sensitive radiation detection*, IEEE Trans. Nucl. Sci. 54 (2007) 280.
- [4] SIMON, A., KALINKA, G., JAKŠIĆ, M., PASTUOVIĆ, Ž., KISS, A.Z., *Investigation of radiation damage in a Si PIN photodiode for particle detection*, Nucl. Instrum. Methods B 260 (2007) 304.
- [5] PASTUOVIĆ, Ž., JAKŠIĆ, M., KALINKA, G., NOVAK, M., SIMON, A., *Deterioration of Electrical and Spectroscopic Properties of a Detector Grade Silicon Photodiode Exposed to Short Range Proton, Lithium and Oxygen Ion Irradiation*, accepted for publication in IEEE Trans. Nucl. Sci.

- [6] AKCOLTEKIN, E., PETERS, T., MEYER, R., DUVEBECK, A., KLUSMANN, M., MONNET, I., LEBIUS, H., SCHLEBERGER, M., *Creation of nanodots by single ions*, Nature Nanotechnology 2 (2007) 290.
- [7] OLIVERO, P., et. al., *Characterization of three-dimensional microstructures in single-crystal diamond*, Diamond and Related Materials 15, (2006), 1614.

FORMATION OF FERRO-, PARA-, AND SUPERPARAMAGNETIC NANOSTRUCTURES BY ION BEAM TREATMENT OF MATERIALS

H. Hofsäss, C. Ronning, S. Müller, K. Zhang, H. Zutz

University Göttingen, II. Physikalisches Institut, Friedrich-Hund-Platz 1,
37077 Göttingen, Germany

Abstract. In this contribution we present studies on the formation of nanostructured magnetic materials using different ion beam treatments. Ion beams can be used to grow nano-composite materials by ion beam deposition, to create nanopatterned surfaces of materials by ion beam erosion and to introduce impurities into matrices by ion implantation. We discuss examples for the three different ion beam modification techniques and highlight their unique features. In Section 2 we describe the formation of carbon-metal nanocomposite materials using Ni and Fe as magnetic constituents. Of particular interest are self-organization effects, leading to the formation of layered structures of paramagnetic nanoclusters. In Section 3 we discuss the nanopattern formation on Ni and Fe thin film surfaces by ion beam erosion, leading to a pronounced correlated uniaxial magnetic texture in these films. In Section 4 we present studies on ion implantation of magnetic impurities into ZnO bulk and nanowire semiconductors.

1. INTRODUCTION

Ion beams can be used in a variety of different ways to synthesize and modify materials on the nanometer scale. Of particular interest is the possibility of ion beams to circumvent thermodynamic limits related to diffusion, solubility, desorption, alloy formation, etc., by providing high kinetic energy through ion impact and utilizing ballistic effects during ion solid interaction. Moreover, by adjusting ion energy, ion species, ion fluence and irradiation geometry it is possible to tailor the ion irradiation conditions for specific needs. In this contribution we discuss three examples of the use of ion beams: ion beam synthesis of nanocomposite materials [1], surface nano-pattern formation by ion beam erosion [2], and doping of semiconductors by ion implantation [3][4]. We focus on modification and synthesis of para- or ferromagnetic materials and discuss the specific influence of the ion beam processes on the structural and magnetic properties of the resulting materials. In Section 2 we describe the formation of Fe_xC and Ni nanoclusters in amorphous carbon (a-C) by ion beam deposition. Of particular interest are self-organization effects, leading to the formation of layered structures of paramagnetic nanoclusters. In Section 3 we discuss the nano-pattern formation on Ni and Fe thin film surfaces by ion beam erosion under glancing angle of incidence, leading to a pronounced correlated uniaxial magnetic texture in these films. Finally, we investigate the possibility of ion implantation of Fe into bulk ZnO and ZnO nanowires as a method to induce magnetic behaviour in this wide band gap semiconductor material.

2. FORMATION OF FERRO-, PARA-, AND SUPER-PARAMAGNETIC NANOCLUSTERS BY ION BEAM DEPOSITION OF CARBON-METAL NANOCOMPOSITES

During ion beam deposition of compound thin films, energetic ion impact enhances processes like sub-surface cluster formation, diffusion, surface segregation and sputtering. The interplay between these processes may result in the formation of self-organized layered nanocomposite thin films, such as metal-carbon nanocomposites [5][6][7][8]. Triggering of self-organization

mechanisms by adjusting ion energy, ion fluence and ion species is investigated for ion beam deposited metal-carbon nanocomposite thin films, grown by simultaneous co-deposition of metal and carbon ions in the energy regime 50–150 eV. The implication of self-organization effects for plasma-based film deposition techniques will be discussed in the following.

The simultaneous deposition of energetic species of two different elements usually leads to homogeneously mixed films due to diffusion and rearrangement processes in subsurface and surface regions. If the involved elements are immiscible, a phase separation with precipitates of one element within the other may occur. The size and distribution of such clusters is strongly dependent on the deposition parameters such as ion energy, provided stoichiometry, and temperature. A number of studies have shown that this phase separation process can also result in the formation of a self-assembled multilayer structure. This structure appears in particular under certain deposition conditions for the co-deposition of carbon and certain metals, including the carbide forming metals Fe. These studies reveal that alternating nanoscale layers of carbon and metal were obtained after co-deposition of the respective energetic species, but with two different methods: mass selected ion beam deposition (MSIBD) and dc-reactive magnetron sputter deposition, respectively.

Here, we report on the experimental results of the multilayer formation for the system a-C:Ni by means of MSIBD [9]. The aim was to test the onset of multilayer formation and the predicted variation of the layer period with the ion energy and the fluence ratio from a simple model describing the multilayer formation. Nickel is a weak carbide forming metal, forming only metastable carbides. The nickel containing amorphous carbon system therefore should be a de-mixing system, which possibly could form a layered structure using the right deposition parameters.

a-C:Ni films were prepared by Mass-Selected Ion Beam deposition (MSIBD). The source of the energetic ions is a penning ion gun feed with CO₂ and equipped with a pure nickel target. The ions were extracted with 30 kV from the source and decelerated in front of the substrate to the desired energy of 100 eV. The beam is mass-separated using a 90° sector magnet, and therefore only carbon and nickel contribute to film growth. The ion current on the substrate is time integrated and measured with aid of a computer. The computer controls the sector magnet and switches between both ions in intervals of 0.5–1 × 10¹⁵ ions split up according to the desired fluence ratio of carbon and nickel ions. The fluence ratio was varied between $r_f = [C]/[Ni] = 93/7$ and 50/50. The films were grown on p-type silicon in <100> orientation which is cleaned by acetone and 1 keV ⁴⁰Ar⁺ sputtering. Prior to the a-C:Ni deposition the substrate is coated with a pure carbon layer to prevent the development of a carbon-silicon-nickel mixing layer.

The first sample was deposited with 100 eV ion energy and with a fluence ratio of $r_f = 90/10 = 9$. The total metal sputtering coefficient calculated by $S_M = r_f \times S_{C \rightarrow M} + S_{M \rightarrow M}$ using SRIM yields $S_M = 3.4 > 1$. For this case, the qualitative film growth model predicts the formation of homogeneously distribution of small clusters in an amorphous carbon matrix. This is exactly what is found by cross-section Transmission Electron Microscopy (X-TEM) and Energy Dispersive X ray Spectroscopy (EDX) (Figure 1). We find small (<3 m) nickel clusters homogeneously distributed in a matrix consisting of amorphous carbon. Using Rutherford Backscattering Spectroscopy (RBS), we found — knowing the total amount of deposited nickel — that only a fraction of $f_{\text{Surface}} = 0.66$ of the nickel ion-implanted into the films segregates to the films surface and is subject to sputtering. Due to the high total metal sputtering coefficient this nickel will not form stable cluster but will be sputtered off. With

this results the model predicts the evolution of a layered structure for the a-C:Ni system with deposition energy of 100 V at fluence ratios of $r_f < 2$. A film deposited with a fluence ratio of $r_f = 60/40 = 1.5 < 2$ ($S_M = 0.84$) shows a layered structure clearly visible in X-TEM and EDX with a layer periodicity of around 33(2) nm (Figure 2). The metal rich layers consist of nickel cluster while the metal deficient layers consist of very small nickel clusters in an amorphous carbon matrix. Another film deposited with a fluence ratio of $r_f = 70/30 = 2.3$ ($S_M = 1.12$) shows a weak layer structure with a periodicity of 18–24 nm. Assuming a little lower mean deposition energy due to the energy straggling of the ion source of 90 eV ($S_M = 0.99$) the layer growth is possible within the limits of the model. The model enables us in the case of a-C:Ni to predicted the structure of the growing film, i.e. either layered structure or homogeneously distributed clusters.

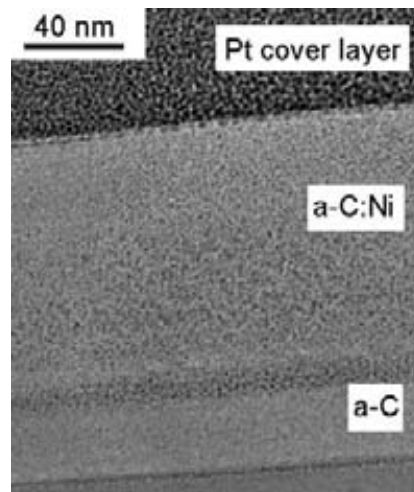


FIG. 1. TEM micrograph of an a-C:Ni film prepared by MSIBD using an ion fluence ratio of $C/Ni = 90/10$ and ion energies of ~ 100 eV at RT on a-C on p-Si. The effective sputter yield for Ni at the surface is $S_M \sim 3.3$ that no Ni cluster agglomeration at the surface occurs. Thus, the Ni clusters are homogeneously distributed in the film. The Pt-cover layer is deposited on the film in the process of TEM preparation using the FIB (from Ref. [9]).

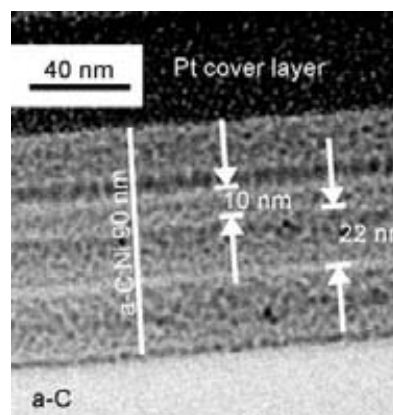


FIG. 2. TEM micrograph of an a-C:Ni film prepared by MSIBD using an ion fluence ratio of $C/Ni = 60/40$ and ion energies of ~ 100 eV at RT on a-C on p-Si. The effective sputter yield for Ni at the surface is $S_M \sim 0.8$, so that Ni clusters may agglomerate at the surface. Thus, the multilayer structure consisting of alternating Ni cluster layers and carbon-rich layers evolves. The Pt-cover layer is deposited on the film in the process of TEM preparation using the FIB.

3. MAGNETICALLY TEXTURED NANO-CRYSTALLINE FE AND NI THIN FILMS AND NANOWIRES ON GLASS SUBSTRATES PREPARED BY ION BEAM EROSION

Ripple patterns created by sputter erosion of Fe and Ni thin films induce a correlated magnetic texture of the surface near region [2]. We investigated the magnetic anisotropy of films deposited on glass substrates as a function of the residual film thickness and determined the thickness of the magnetically anisotropic layer as well as the magnitude of the magnetic anisotropy using MOKE and RBS measurements. Polycrystalline 140 nm thick Fe films were deposited at the room temperature on glass substrates of $7 \times 10 \text{ mm}^2$ using electron beam evaporation. X ray diffraction of the as-deposited and sputter eroded films gave a width of $\text{FWHM} = 0.8(1)^\circ$ for the Fe(110) diffraction peak, corresponding to an average grain size of about 12–15 nm. Ripple patterns were created by sputter erosion with 5 keV Xe ions under grazing incidence of 80° with respect to the surface normal. Since MOKE is a surface sensitive measurement with a sensitive depth of about 15 nm, MOKE analysis from the top and bottom sides of the films provides unambiguous information of the size of the textured layer and the magnitude of the anisotropy.

The as-deposited samples exhibit an isotropic surface topography and an isotropic magnetic behaviour. After erosion with ion-fluences above $1 \times 10^{16} \text{ cm}^{-2}$ the formation of ripples with wavelengths between 30 nm and 80 nm oriented parallel to the ion beam direction is observed (Figure 3). A clear uniaxial anisotropy with magnitude of about 10–20 % and easy axis along the ripple direction is seen for films with about $d = 50\text{--}70 \text{ nm}$ residual thickness (Figure 4). For d smaller than 30 nm the magnetic anisotropy increases and approaches 60–100% for small residual thickness, depending on the roughness of the substrate used. The measured MOKE anisotropies can be explained in the framework of a two-layer model: an approximately 12 nm thick surface layer with uniaxial magnetic anisotropy on top of the magnetically isotropic bulk. This layer thickness is comparable to the average grain size as determined by XRD. As long as the residual film thickness is less than $\sim 30 \text{ nm}$, the magnetic anisotropy of the whole film is dominated by the anisotropy induced by the surface ripples. For increasing film thickness, the underlying isotropic film partially suppresses the anisotropy of the top layer down to a fraction of 25%. The Fe films on glass exhibit a weaker anisotropy, only 65% compared to Fe on Si, which is assumed to be due to the higher roughness of the glass substrate. Figure 5 shows the comparison of calculated MOKE anisotropies based on the two-layer model and measured MOKE anisotropies for the Fe films deposited on Si and glass substrates. The model calculations are in very good agreement with measured anisotropies. Our results indicate that the magnitude of the magnetic anisotropy depends only weakly on the values of the ripple wavelength and amplitude. However, the variation in wavelength and ripple amplitude in our studies was limited to about 30–120 nm and less than about 5 nm, respectively. All sputter experiments were done at room temperature. It is well known that ripple patterns depend on the substrate temperature via surface diffusion processes. Higher temperatures give rise to larger ripple wavelengths and eventually smoother surfaces. Thus, the substrate temperature may have an influence on the magnetic anisotropy of ferromagnetic films. Further systematic studies regarding these aspects may be done in the future.

We have also shown that films with very thin residual thickness separate into individual nano-wires or nano-rods due to the ripple structure [2]. Thus, ion beam erosion with grazing incident ion beams allows fabricating ferromagnetic nano-rods and nano-wires with complete uniaxial magnetic anisotropy.

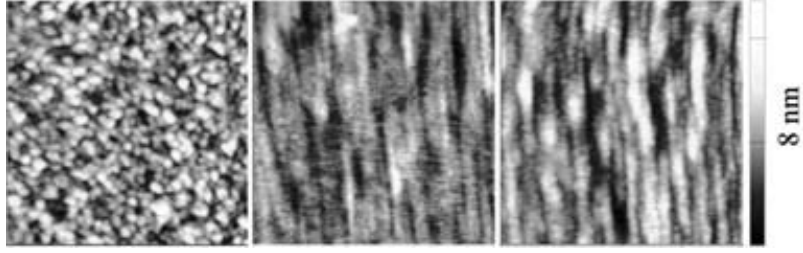


FIG. 3. AFM analysis of an as deposited Fe film (left) and ripple structures for Fe films sputtered with 5 keV Xe at 80° and $5 \times 10^{16} \text{ cm}^{-2}$ (middle) and $7 \times 10^{16} \text{ cm}^{-2}$ (right) and subsequently coated with 4.5 nm Cr. Shown is an area of $1 \times 1 \mu\text{m}^2$. The ripple orientation is parallel to the incident ion beam (from Ref. [10]).

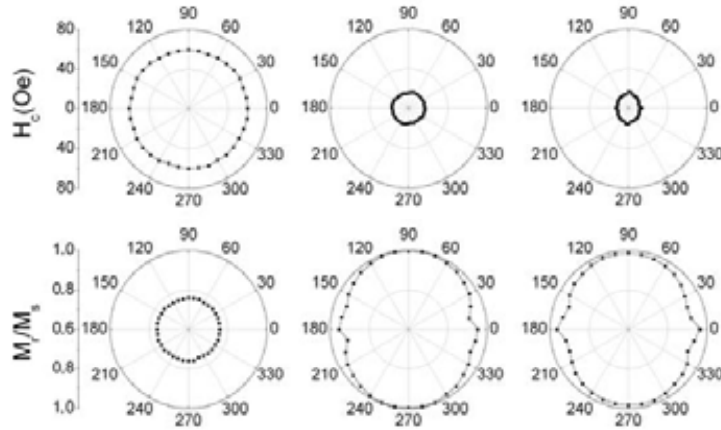


FIG. 4. MOKE analysis of the films shown in Fig. 3. Plotted is the coercive field H_C and the relative remanence M_r/M_s for the as-deposited (left) and two eroded films (middle and right). The uniaxial anisotropy has its easy axis oriented parallel to the ripples and the anisotropy of the MOKE signal is about 10%. A weak four-fold anisotropy is also visible (from Ref.[10]).

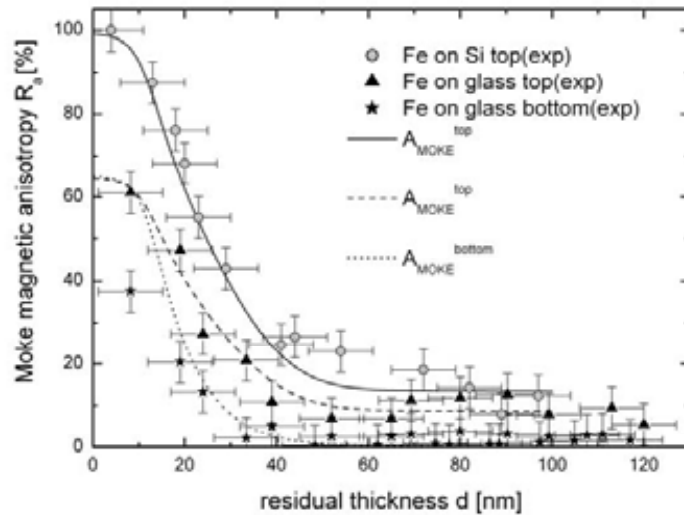


FIG. 5. Comparison between experimentally observed MOKE anisotropies and calculated anisotropy according to a two-layer model assuming a top-layer with uniaxial anisotropy and an isotropic bulk film. “Top” indicates MOKE analysis from the top side of the film; “bottom” indicates MOKE analysis from the bottom of the film through the glass substrate (from Ref. [10]).

4. FE-IMPLANTED ZINC OXIDE CRYSTALS AND NANO-WIRES

Room temperature ferromagnetism has been proposed for transition metal (TM) doped ZnO, and therefore ZnO:TM is of high potential for spintronic applications [12]. Additionally, TM-doped semiconductors show optically active and sharp intra-3d-transition with long life-times. Such intra-shell transitions are usually forbidden, but due to the incorporation into a suitable matrix the crystal field splitting leads to long-lived, partly allowed, transitions.

ZnO nano-wires were grown by the vapour liquid solid (VLS) growth mechanism, where silicon substrates covered with a 4 nm thick Au film and pure ZnO powder were placed in a horizontal tube furnace and heated up to 1350°C [13]. An argon gas flux of 50 sccm transports the evaporated ZnO to the substrates which were placed in a temperature zone of about 1100°C. The pressure was adjusted to about 100 mbar during the whole growth process. The as-deposited nano-wires are typically up to 100 μm long and between 40 and 500 nm in diameter, as determined by scanning electron microscopy (SEM).

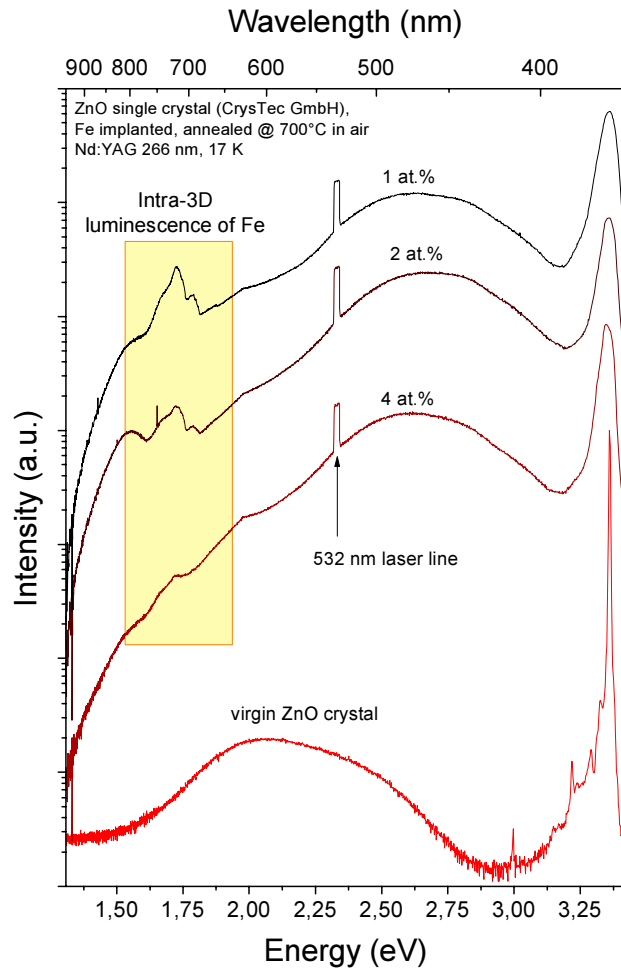


FIG. 6. Photoluminescence spectrum of Fe ion implanted ZnO crystals measured at 17K using a 266 nm Nd:YAG UV laser for excitation. Shown are the spectra of the virgin ZnO crystal, and crystals with Fe concentrations from 1–4 at.% after annealing at 700°C. The intra 3D luminescence from Fe impurities is visible between 700 and 800 nm.

Fe ions were implanted into VLS-grown ZnO nanowires and ZnO single crystals (CrysTec GmbH, Berlin) with a box like profile and different fluences to obtain transition metal concentrations of 1, 2 and 4 at.%. The implanted ZnO samples were annealed at 700°C for 30 min in air. During the ion implantation of Fe and annealing, no secondary phases or out diffusion of Fe was observed in the ZnO nanowires or crystals, which was confirmed with transmission electron microscope. Due to the sputtering during the ion implantation process the surface roughness of the nano-wires increases and is visible in TEM images. The successful implantation of Fe was confirmed with energy dispersive X ray and energy electron loss spectroscopy which show the corresponding Fe singles. RAMAN measurements show an increasing intensity of the disordering band around the $A_1(\text{LO})$ phonon vibration with increasing Fe concentration. In comparison to Mn implanted ZnO no additional elemental specific local vibration mode was found by RAMAN spectroscopy. Cathodoluminescence and photoluminescence studies show a sharp and intense intra-3D luminescence of Fe^{3+} in ZnO in the red/near-infra-red luminescence region between 1.70 and 1.78 eV (Figure 6). The intensity of the intra-3D luminescence of the Fe implanted ZnO is a half magnitude lower than the maximum peak intensity of the entire luminescence, which is located in the green luminescence band. In particular, the structured form of the green luminescence band is a consequence of the ion implantation process and is also visible after ion implantation of other transition metals into ZnO. Intra-3D luminescence decreases with increasing Fe concentration in the ZnO single crystals compared to the ultra violet luminescence.

The magnetism of the Fe implanted ZnO single crystals was characterised with MOKE and shows a weak paramagnetic or possibly ferromagnetic signal at room temperature for the 2 at.% and 4 at.% doped samples, where as the 1 at.% Fe doped ZnO single crystal reveal only diamagnetic properties. The hysteresis is very weak and coercive fields are close to zero. Mössbauer measurements before annealing reveal the appearance of Fe in the 3^+ and 2^+ charge state which should reorder during the annealing and principally the Fe^{3+} charge state should remain in the crystal (Figure 7). These studies are under way. Ferromagnetism in doped ZnO and GaN semiconductors are still under debate, experimentally as well as theoretically. The present studies at least demonstrate the successful incorporation of Fe as possible magnetic impurity into ZnO and the feasibility of MOKE and Mössbauer spectroscopy to characterize the behaviour of Fe as magnetic impurity in semiconductors.

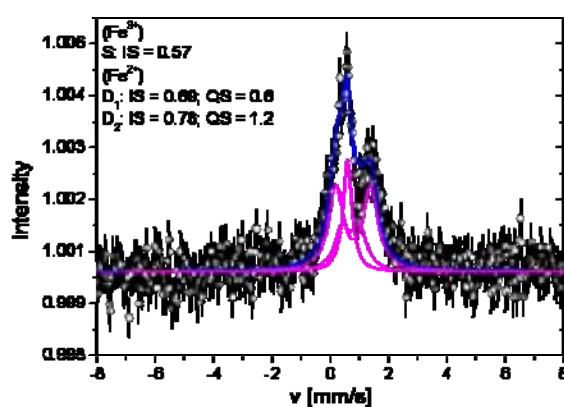


FIG. 7. Mössbauer spectrum for Fe-implanted ZnO implanted at room temperature and without annealing. The spectrum shows two doublet lines (D_1 and D_2) of the Fe^{2+} charge state (D_1 : isomer shift 0.69 mm/s, quadrupole splitting 0.6 mm/s; D_2 : isomer shift 0.78 mm/s and quadrupole splitting 1.2 mm/s) and a singlet line with isomer shift 0.57 mm/s of the Fe^{3+} charge state.

ACKNOWLEDGEMENTS

We would like to acknowledge the help and cooperation of the following colleagues: Y-M. Ting (University of Tainan, Taiwan), S. Cusenza (University Göttingen), M.J. Zhou and Q. Li (Chinese University of Hong Kong), M. Koerdel, M. Schumm, F. Bach, J. Geurts (Universität Würzburg), Prof. K. Bharuth-Ram (iThemba-LABS, South Africa).

REFERENCES

- [1] HOFSSÄSS, H., *Ion Beam Deposition of Thin Films: Growth Processes and Nanostructure Formation* Invited Lecture, Symposium on the Physics of Ionized Gases, SPIG-2004, Tara, Serbia & Montenegro, AIP Conf. Proc. 740 (2004) 101.
- [2] ZHANG, K., ROTTER, F., UHRMACHER, M., RONNING, C., HOFSSÄSS, H., KRAUSER, J., *Ion induced nanoscale surface ripples on ferromagnetic thin films with correlated magnetic texture*, New J. Phys. 9 (2007) 29.
- [3] RONNING, C., DALMER, M., UHRMACHER, M., RESTLE, M., VETTER, U., ZIEGELER, L., HOFSSÄSS, H., GEHRKE, T., JÄRREND AHL, K., DAVIS, R.F., *Ion implanted impurities in GaN and AlN: lattice sites, annealing behavior and defect recovery*, J. Appl. Phys. 87 (2000) 2149.
- [4] MÜLLER, S., STICHTENOTH, D., UHRMACHER, M., HOFSSÄSS, H., RONNING, C., KULINSKA, A., RÖDER, J., *Unambiguous identification of the PL-I₀-line in zinc oxide*, Appl. Phys. Lett. 90 (2007) 012107.
- [5] GERHARDS, I., STILLRICH, H., RONNING, C., HOFSSÄSS, H., SEIBT, M., *Self-organized Nanoscale Multilayer Growth in Hyperthermal Ion Deposition*, Phys. Rev. B 70 (2004) 245418.
- [6] GERHARDS, I., RONNING, C., VETTER, U., HOFSSÄSS, H., GIBHARDT, H., ECKOLD, G., LI, Q., LEE, S.T., HUNAG, Y.L., Seibt, M., *Ion beam synthesis of amorphous carbon thin films containing metallic nanoclusters*, Surf. Coat. Technol. 158/159 (2002) 114.
- [7] WU, W.-Y., TING, J.-M., ZUTZ, H., LYZWA, D., GERHARDS, I., RONNING, C., HOFSSÄSS, H., *Comparative study of self-assembling of multilayers using reactive sputter deposition and mass selective ion beam deposition*, Diam. Relat. Mater. (2008) in print.
- [8] RONNING, C., GERHARDS, I., SEIBT, M., HOFSSÄSS, H., WU, W.Y., TING, J.M., *Self-assembled nano-scale multilayer formation using physical vapor deposition methods*, Nucl. Instrum. Meth. 242 (2006) 261.
- [9] ZUTZ, H., GERHARDS, I., RONNING, C., HOFSSÄSS, H., SEIBT, M., WU, W.Y., TING, J.-M., *Self-organized nanoscale multilayer growth during the deposition of hyperthermal species*, Rev Adv. Mat. Sci. 15 (2007) 241.
- [10] ZHANG, K., UHRMACHER, M., KRAUSER, J., HOFSSÄSS, H., *Magnetic texturing of ferromagnetic thin films by sputtering induced ripple formation*, J. Appl. Phys. (2008) accepted.
- [11] HOFSSÄSS, H., ROTTER, F., UHRMACHER, M., ZHANG, K., RONNING, C., KRAUSER, J., *Sputter erosion of ferromagnetic thin films*, Surf. Coat. Technol. 201 (2007) 8477.
- [12] SCHLENKER, E., BAKIN, A., SCHMID, H., MADER, W., ALBRECHT, M., RONNING, C., MÜLLER, S., AL-SULEIMAN, M., POSTELS, B., WEHMANN, H.H., SIEGNER, U., WAAG, A., *Properties of V-implanted ZnO nanorods*, Nanotechnology 18 (2007) 125609.
- [13] BORCHERS, C., MÜLLER, S., STICHTENOTH, D., SCHWEN, D., RONNING, C., *Catalyst-nanostructure interaction in growth of 1D-ZnO nanostructures*, J. Phys. Chem. B 110 (2006) 1656.

FORMATION OF MAGNETIC NANOCCLUSERS AND COMPLEXES BY ION IMPLANTATION OF Fe INTO SUITABLE INSULATORS

K. Bharuth-Ram^{ab}

^aSchool of Physics, University of Kwazulu-Natal, Durban 4041, South Africa

^biThemba LABS, Somerset West 7129, Western Cape, South Africa

Abstract. The focus of the project was to use ion implantation of Fe into suitable host matrices to achieve the formation of assemblies with magnetic order. In the main part of the project mass separated ^{57}Fe ions were implanted to fluences of 1×10^{15} , 1×10^{16} and $2 \times 10^{16} \text{ cm}^{-2}$, into a range of substrates which included ZnO, 3C-SiC, CVD diamond, SiO_2 , Si and graphite. The search for cluster formation was conducted as functions of thermal treatment of the substrates and implantation dose. Characterization methods included Mössbauer spectroscopy, Rutherford Backscattering spectrometry, and MOKE and VSM measurements. The Mössbauer spectra of the Fe implanted ZnO and SiC single crystals, annealed up to 1073K and 973K, respectively, show that the Fe^{3+} ions remain fairly constant in the crystals, while the Fe^{2+} show some reordering. However, no clear evidence of magnetic clustering was obtained. Complementary investigations were also conducted with the Mössbauer Spectroscopy group at CERN on Mössbauer studies on magnetic complexes formed in ZnO (as well as other oxides) following ion implantation of extremely low fluences of ^{57}Mn . The ZnO spectra, in addition to the expected doublet structure due to Fe at substitutional and interstitial sites, displayed magnetic structures that have been analysed in terms a sharp sextet, two paramagnetic doublets, and two ferromagnetic magnetic distribution. The magnetic effects disappear above 600K. The formation of the magnetic ordering is proposed to occur on an atomic scale upon the association of complexes of Mn/Fe probe atoms with the Zn vacancies that are created in the implantation process, and conversely, disappearance sets in above 600K due to thermally activated annealing of the vacancies.

1. INTRODUCTION

Ion beam methods have particular application in the modification of materials where they have been especially utilized to produce effects tailored to particular applications, incorporate dopant atoms in crystalline materials in which thermal diffusion is precluded by formation energy barriers, and to study the interactions between implanted impurity and radiation induced defects. In this contribution we present examples of the ion beam applications in i) a search for the formation of nano-clusters of ion implanted ferromagnetic ions in insulators, and ii) ion implantation induced magnetic complexes formed in ZnO.

The main focus of the programme was to investigate the conditions required to achieve the production of magnetic nano-clusters of low fluence implanted Fe ions into bulk SiC, ZnO, and several other substrates. The program included investigations as functions of implantation fluence and annealing temperature of the substrates. This is discussed in Section 1. Section 2 presents the results of studies carried out with the CERN Mössbauer group on investigation on room temperature ferromagnetic effects in ZnO achieved with extremely low fluence implantation of $^{57}\text{Mn}/^{57}\text{Fe}$.

2. FORMATION OF MAGNETIC NANOCCLUSERS BY ION IMPLANTATION OF FE IN INSULATORS

Ferromagnetic (FM) ion clusters of size below 5 nm have a high proportion of surface atoms which results in a narrowing of the d-band responsible for magnetism. This, coupled with quantum size effects, has been observed to lead to clusters with novel properties such as

increase in the magnetic anisotropy and enhancements of the magnetic moment per atom [1][2]. This stimulated our investigations into the formation of ferro-, para- and diamagnetic clusters in suitable insulating materials following ion implantation of Fe ions and thermal treatment of the host material.

Mössbauer spectroscopy (MS) provides clear signatures of the onset of magnetic order, and was therefore employed as our main characterization method, with the Mössbauer probe nuclide ^{57}Fe being used as the implanted Fe species. Mass separated ^{57}Fe ions were implanted at energies of 60 or 80 keV, and to fluences of 5×10^{15} , 1×10^{16} and $2 \times 10^{16} \text{ cm}^{-2}$, using the Göttingen ion implanter, Ionas, into a range of substrates which included ZnO, 3C-SiC, SiO₂ CVD diamond and graphite. The search for cluster formation was conducted as functions of thermal treatment of the substrates and implantation dose. Characterization methods included Mössbauer spectroscopy, Rutherford Backscattering spectrometry, Raman spectroscopy and MOKE and VSM measurements.

The effects of annealing on the distribution ^{57}Fe ions in the SiC and ZnO samples were monitored with RBS and optical UV-Visible transmission measurements. The RBS measurements were performed at a grazing angle of 10° with a 2 MeV ^4He beam from the van de Graaf accelerator at iThemba LABS. Sample SiC spectra are displayed in Fig. 1. Figure 2 presents UV-Visible transmission measurements. Both samples display noticeable change in the transmission efficiency on annealing, reflecting the re-distribution of the implanted Fe ions from their implantation profiles.

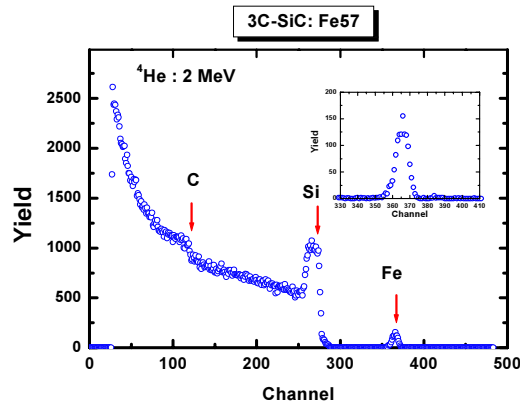


FIG. 1. RBS spectrum of 3C-SiC sample implanted with $1 \times 10^{16}/\text{cm}^2$ ^{57}Fe , and annealed at 573K. The inset shows the Fe distribution.

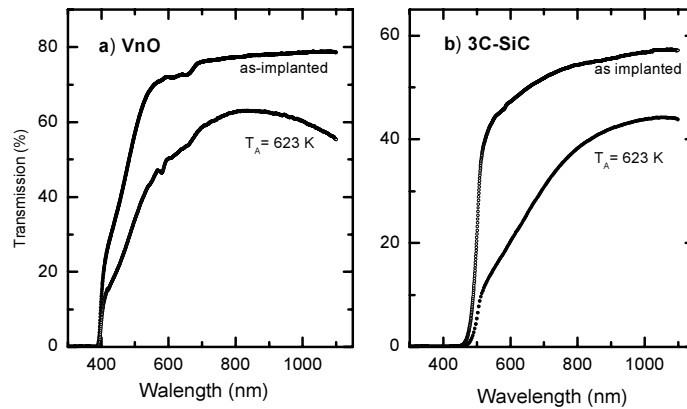


FIG. 2. UV-Visible transmission intensity of the ^{57}Fe -implanted VnO (left) and SiC (right) samples, before and after annealing at 623K.

Preliminary conversion electron Mössbauer measurements (CEMS) on a SiC sample implanted with 1×10^{16} ^{57}Fe suggested small contributions of magnetic components in spectra. Hence, subsequent Mössbauer measurements were made in transmission mode at 300K and 80K, on the as-implanted sample and after annealing the sample at 623K. The spectra are displayed in Fig. 3, obtained at the temperatures indicated for a) the as-implanted sample, and b) after heating the substrate at 623K for 1 hour. The spectra show evidence of magnetic structures imposed on the expected doublet components due to Fe at tetrahedral substitutional, interstitial and damage sites in the 3C-SiC lattice [3].

These features were supported by magnetization measurements which were made with a vibrating sample magnetometer (VSM) on the as-implanted and annealed samples. Because of the low Fe concentration, the VSM signals were close to the tolerance level of the instrument, and consequently several days of measurements were required on the samples. A composite plot of the many measurements made on the annealed SiC sample, corrected for diamagnetic effects in the virgin sample, is presented in Fig. 4. A small ferromagnetic behaviour is evident.

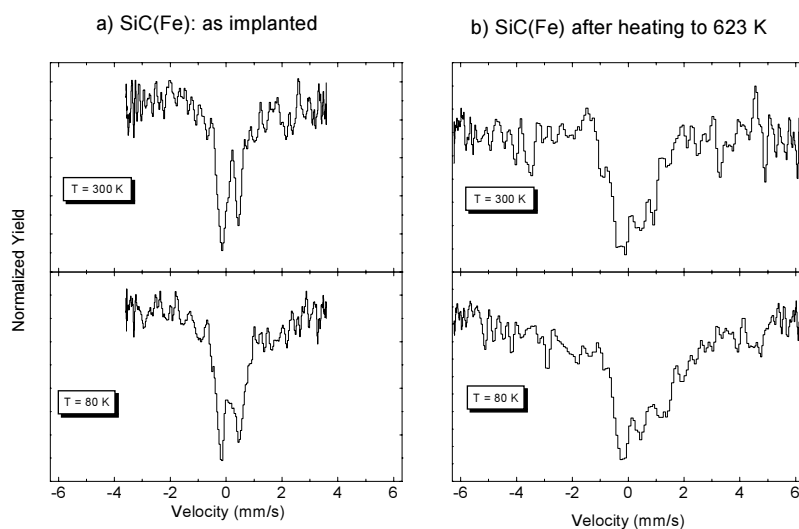


FIG. 3. Transmission Mössbauer spectra observed for ^{57}Fe implanted-3C-SiC at 300K and 80K: a) as-implanted sample, b) after heating sample at 623K for 1 h.

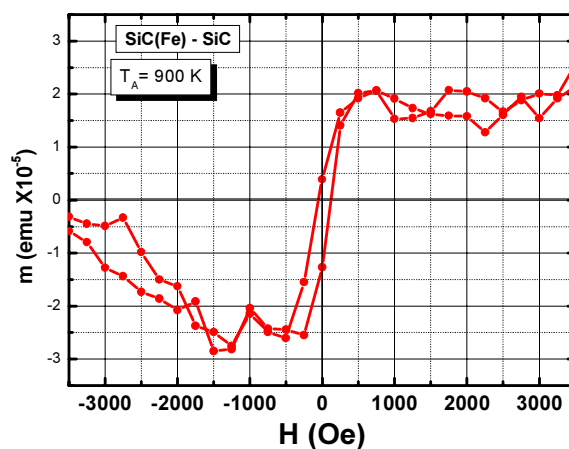


FIG. 4. Composite plot of magnetization measurements on SiC sample after annealing at 623K.

In order to obtain spectra with better statistics CEMS measurements were made at RT on the ZnO and 3C-SiC samples with a recently acquired 50 mCi $^{57}\text{CoRh}$ source. The spectra are presented below.

2.1. ZnO

ZnO is a substrate that has attracted the considerable recent interest in studies on low fluence ion implantation induced magnetization. Several authors have reported observation of magnetization effects in this wide band gap semiconductor following incorporation of 1–3 at.% transition metal ions [4][5][6].

CEMS spectra of a ZnO substrate (purchased from Crystec GmbH, Munich) implanted with 1×10^{16} ^{57}Fe ions/cm² and annealed at 623K, and a second substrate implanted with 2×10^{16} /cm² ^{57}Fe and annealed at 973K and 1073K are displayed in Fig. 5.

The components required to fit the spectra, and their assignments are listed in Table 1. Evidently, while the annealing brings about changes in the population of the Fe in the different configurations, there is no evidence of magnetic sextet in the spectra, as has been observed by Potzger et al. [7][8]. These authors observed this effect only with high fluence (4×10^{16} /cm²) and high temperature (623K) implanted sample.

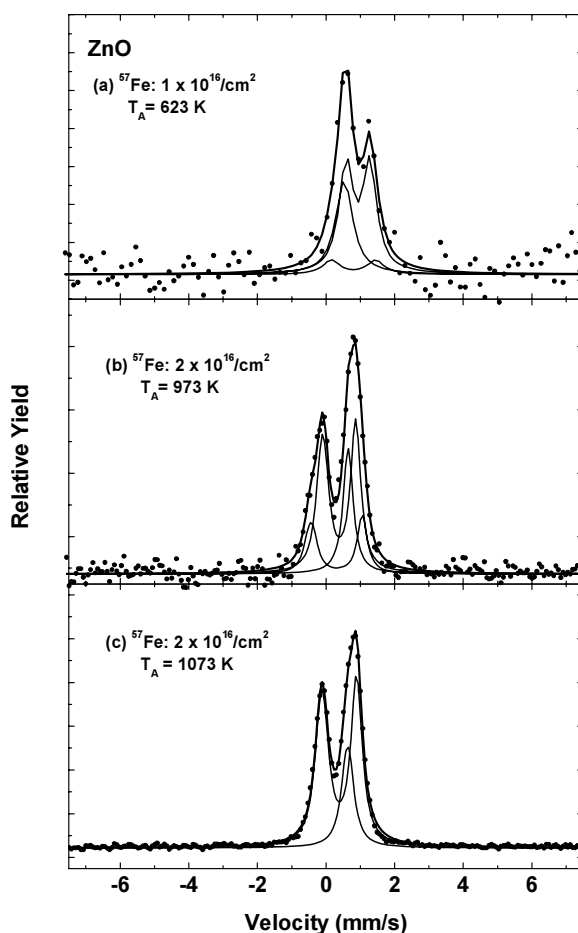


FIG. 5. CEMS spectra of ZnO substrates implanted with ^{57}Fe to fluences of 1×10^{16} /cm² and 2×10^{16} /cm² and annealed at temperatures indicated.

Table 1. Hyperfine parameters (isomer shift δ and quadrupole splitting ΔE) and fractions (f) of components required to fit the spectra of ^{57}Fe implanted ZnO (d is the implantation fluence). The parameters are in reasonable agreement with previously reported values [4][5][6].

Sample	Component	δ (mm/s)	ΔE (mm/s)	f (%)
1, $d = 1 \times 10^{16}/\text{cm}^2$ $T_A = 623\text{K}$	S1 (Fe^{3+})	0.53(5)	-	32(3)
	D1 (Fe^{2+})	0.93(5)	0.68(5)	59(4)
	D2 (Fe^{2+})	0.81(5)	1.3(1)	9(2)
2, $d = 2 \times 10^{16}/\text{cm}^2$ $T_A = 973\text{K}$	S1 (Fe^{3+})	0.64(5)	-	23(4)
	D1 (Fe^{2+})	0.37(5)	0.96(5)	57(5)
	D2 (Fe^{2+})	0.30(5)	1.50(6)	21(4)
2, $d = 2 \times 10^{16}/\text{cm}^2$ $T_A = 1073\text{K}$	S1 (Fe^{3+})	0.63(5)	-	24(4)
	D2 (Fe^{2+})	0.39(5)	1.01(5)	76(6)

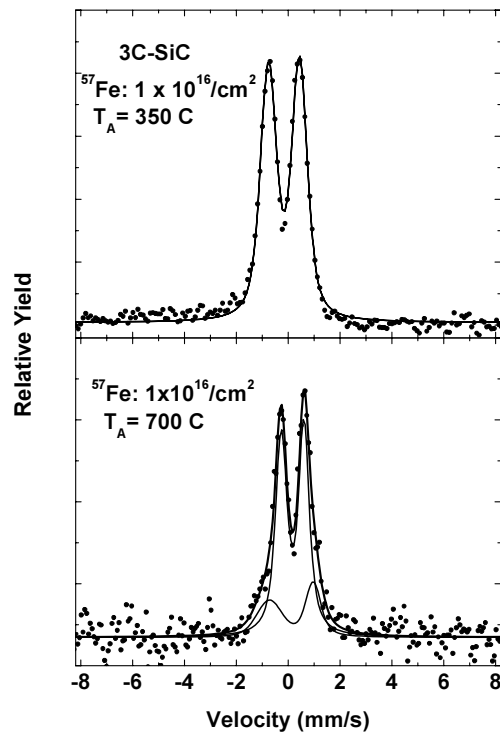


FIG. 6. CEMS spectra of 3C-SiC substrate implanted with ^{57}Fe to fluences of $1 \times 10^{16}/\text{cm}^2$ and annealed at temperatures indicated.

2.3. 3C-SiC

CEMS spectra of a 3C-SiC sample implanted with 1×10^{16} ^{57}Fe ions/cm² and annealed at 623K and 973K are displayed in Fig. 6. The spectrum, after annealing the sample at 623K, required just one component, a quadrupole split doublet, with $\delta = -0.16(5)$ mm/s, and splitting $\Delta E = 1.20(4)$ mm/s, to give a fit. After annealing at 973K, additional structures in the wings of the central component become evident. This has been fitted with a broad asymmetric doublet with $\delta = 0.12(4)$ mm/s and $\Delta E = 1.7(2)$ mm/s, but spectra with better statistics are required to give a more definite account.

3. MAGNETIC COMPLEX FORMATION AT DILUTE FE ATOMS IN ION IMPLANTED ZNO

These investigations were carried out with the Mössbauer group at CERN [9, 10], and were stimulated by the reported achievement of room temperature ferromagnetic behaviour (RTFM) in ZnO by heavy doping with 3d transition metals [4][5][6]. A full understanding of this phenomenon is still lacking, and is complicated by the reported different behaviour observed in (nominally) identical systems by different observers [11]. Radioactive $^{57}\text{Mn}^+$ ions were produced at the online isotope separator facility, ISOLDE, at CERN, using 1.4 GeV proton induced fission in a UC₂ target. Following laser ionisation, clean beams of $^{57}\text{Mn}^+$ ions were accelerated to 60 keV and implanted into ZnO samples held at temperatures between 300 and 800K in an implantation chamber. About $10^{12}/\text{cm}^2$ $^{57}\text{Mn}^+$ ions were implanted into each sample. Mössbauer emission spectra were recorded with parallel-plate resonance detectors equipped with ^{57}Fe enriched stainless steel electrode and mounted on a velocity drive unit outside the implantation chamber.

The Mössbauer spectra obtained at the temperatures indicated are shown in Fig 7. In addition to two doublet structures, Di and D2, expected for isolated Fe at substitutional and interstitial sites in ZnO, the spectra display clear magnetic structures which disappear above 600K. The magnetic structures have been analyzed in terms of a sharp sextet, and two distributions.

The fitted parameters together with their assignments are collected in Table 2, where the isomer shifts are given relative to α -Fe. The results are discussed in detail in Ref. [12]. Two components, the Fe(II) distribution and doublet D2 are assigned to recoil produced interstitial fractions (recoil energies ≤ 84 eV are imparted to the ^{57}Fe ions in the ^{57}Mn β -decay), the other fractions to substitutional Fe_{Zn} with different surroundings. Of particular interest is the sharp magnetic sextet. The temperature dependent measurements together with isothermal time dependent measurements lead us to propose that the formation of the magnetic ordering occurs on an atomic scale upon the association of complexes of Mn/Fe probe atoms with the (mobile) Zn vacancies that are created in the implantation process. Thermally activated annealing then results in the disappearance of the magnetic effects above 600K.

4. CONCLUSIONS

The Mössbauer spectra of the Fe implanted ZnO single crystals show that the Fe³⁺ ions remain fairly constant in the crystal, while the Fe²⁺ show some reordering. However, even after annealing at 1073K no magnetic ordering is achieved. Similarly, the measurements on the SiC sample show evidence that reordering of the implanted Fe is occurring, but there is no clear evidence of formation of nano-clusters with magnetic order. Nonetheless, the present studies, as stated elsewhere by Professor Hofsäass, at least demonstrate the successful incorporation of Fe as possible magnetic impurity into ZnO (and SiC) and the feasibility of MOKE and Mössbauer spectroscopy to characterize the behaviour of Fe as magnetic impurity in semiconductors.

Perhaps a way forward is suggested by recent studies of Muller et al. [13] on a ZnO single crystal implanted with $2 \times 10^{16}/\text{cm}^2$ Fe ions of several different energies to give a box shaped Fe distribution. MOKE signals of the sample display weak ferromagnetic characteristics at room temperature for the 2 at.% and 4 at.% doped samples, while the 1 at.% Fe doped ZnO single crystal reveal only diamagnetic properties.

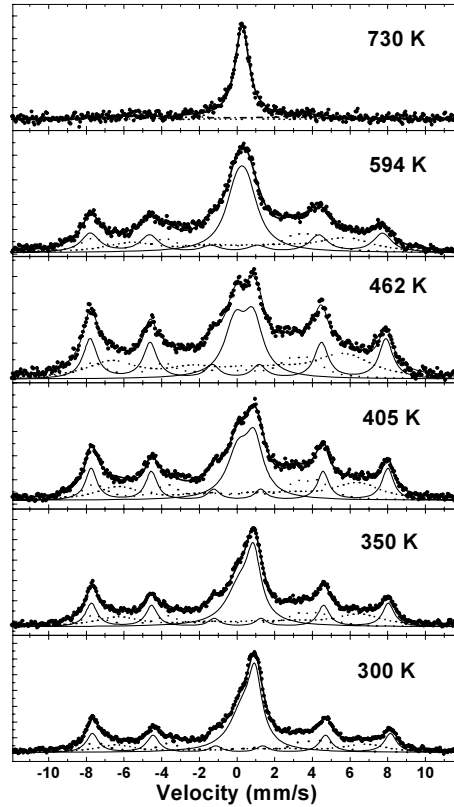


FIG. 7. Mössbauer spectra obtained at temperatures indicated, together with the fitted components.

Table 2. Fitting components, assignments and hyperfine parameters for Mn/Fe implanted ZnO: δ is the isomer shift, QS the quadrupole splitting or quadrupole shift, and B_{hf} the magnetic hyperfine field.

Spec. Comp.	Assignment	B_{hf} (T)	δ (mm/s)	QS (mm/s)
D1	Subst. Fe_{Zn}	-	0.80(2)	0.30 (5)
D2	Interstit. Fe_i	-	0.55(2)	0.73(5)
Sextet	$\text{Fe}_{\text{Zn}}\text{-O-V}_{\text{Zn}}$	48.3(3)	0.20(2)	0.13(2)
Fe(III) distr.	Complex	37(2)	0.13(5)	\sim 0.83(5)
Fe(II) disstr.	Interstit. Fe_i	12(3)	0.82(5)	-0.11(8)

ACKNOWLEDGEMENTS

KBR would like to acknowledge the help and collaboration of H. Hofsäss, C. Ronning and M. Uhrmacher of the University of Goettingen (Germany), M. Maaza and T.B. Doyle of iThemba LABS (South Africa) and of G. Weyer, H.P. Gunnlaugsson and the CERN Mössbauer group.

REFERENCES

- [1] LIU, C., YUN, F., MOROC, H., *Ferromagnetism of ZnO and GaN: A Review*, J. Mat. Sci. 16 (2005) 555.
- [2] JANISCH, R., GOPAL, P., SPALDIN, N.A., *Transition metal doped TiO₂ and ZnO — present status of the field*, J. Phys. C. 17 (2005) R657.
- [3] Bharuth-Ram, K., Gunnlaugsson, H.P., Mantovan, R., Naicker, V., Naidoo, D., Sielemann, R., Weyer, G., Aigne, T.h., *Mössbauer study of Fe in 3C-SiC following ⁵⁷Mn implantation*, Hyper. Int. (2008) (in press).
- [4] SHARMA, P., et al., *Ferromagnetism above room temperature in bulk and transparent thin films of Mn doped ZnO*, Nature Materi. 2 (2003) 673.
- [5] VENKATESAN, M., FITZGERALD, C.B., LUNNEY, J.G., Coey, J.M.D., *Anisotropic ferromagnetism in substituted zinc oxide*, Phys. Rev. Lett. 93 (2004) 177206.
- [6] ALARIA, J., et al., *Pure paramagnetic behaviour in Mn-doped ZnO semiconductors*, J. Appl. Phys. 99 (2006) 08M118.
- [7] POTZGER, K., et al., *Fe implanted ferromagnetic ZnO*, Appl. Phys. Lett. 88 (2006) 052508.
- [8] ZHOU, S., et al., *Fe implanted ZnO: Magnetic precipitate versus dilution*, J. Appl. Phys. 103 (2008) 023902.
- [9] WEYER, G., et al., *Creation and annealing of defect structures in silicon-based semiconductors during and after implantations at 77–500K*, Nucl. Instrum. Methods B 206 (2003) 90.
- [10] WEYER, G., GUNNLAUGSSON, H.P., DIETRICH, M., AIGNE, T.H., BHARUTH-RAM, K., *Mössbauer spectroscopy on Fe impurities in diamond*, Eur. J. Phys. Appl. Phys., 27 (2004) 317.
- [11] LAWES, G., RISBUD, A.A., RAMIREZ, A.P., SESHADI, R., *Absence of ferromagnetism in Co and Mn substituted polycrystalline ZnO*, Phys. Rev. B 28 (2005) 045201.
- [12] WEYER, G., GUNNLAUGSSON, H.P., MANTOVAN, R., FANCUILLI, M., NAIDOO, D., BHARUTH-RAM, K., AIGNE, T.H., *Defect-related local magnetism at dilute Fe atoms in ion-implanted ZnO*, J. Appl. Phys. 102 (2007) 113915.
- [13] MULLER, S., RONNING, C., HOFSSÄSS, H. (private communication).

ION IMPLANTATION DOPING OF SrTiO₃

U. Wahl^a, J.G. Correia^b, A.C. Marques^c, C.P. Marques^a, E. Alves^a,
L. Pereira^d, J.P. Araújo^d, K. Johnston^e

^aDepartamento Física, Instituto Tecnológico e Nuclear, Sacavém, Portugal

^bCERN-PH, Genève, Switzerland

^cCentro de Física Nuclear da Universidade de Lisboa, Lisbon, Portugal

^dDepartamento de Física, Universidade do Porto, Porto, Portugal

^eUniversität des Saarlandes, Saarbrücken, Germany

Abstract. We have explored the possibilities for doping of SrTiO₃ by means of ion implantation. One of our major findings is that the annealing temperature for effective recovery of implantation damage in SrTiO₃ is around 1000–1250°C, which is much higher than the 400–600°C recrystallization temperature of amorphous SrTiO₃ reported in the literature. The second major finding is that most of the implanted foreign atoms in SrTiO₃ (with the exception of Fe) behave in an amphoteric way, i.e. they partially substitute for Sr and Ti, which complicates site-specific doping attempts in this material. Besides the chemical properties, the ionic size is a decisive factor in determining the preferred lattice position, however, this criterion seems to be less applicable in the case of rare earths.

1. INTRODUCTION

The perovskite-type oxides ABO₃, e.g. SrTiO₃, BaTiO₃, KTaO₃, manganites such as La_{2/3}Ca_{1/3}MnO₃, etc., are a class of isolators that have a wide range of existing or potential applications in various fields of microelectronics and optoelectronics, for instance as dielectrics, ferroelectrics, magnetic materials or phosphors [1][2][3]. Strontium titanate SrTiO₃, for instance, is of interest for future devices based on metal-oxide Si heterostructures [4][5] such as high-*k* field effect transistors or as a dilute magnetic semiconductor in spintronics [2], while manganites are materials exhibiting colossal magnetoresistance (CMR) [3]. Many of the perovskites exhibit structural phase transitions at high or low temperatures, which are accompanied by pronounced changes of their electrical, optical and magnetic properties. The phase transitions are a result of the strong coupling of electronic and structural degrees of freedom that is characteristic for these materials. The electrical, optical and magnetic properties of the perovskites are also modified by the incorporation of dopants.

It has been shown that SrTiO₃ and other ABO₃ oxides which have been amorphized by means of ion implantation or deposited as an amorphous film on crystalline SrTiO₃ substrates can be recrystallized by solid state epitaxy around 400–600°C [6]–[14]. Ion implantation should thus represent an attractive approach for doping, especially in cases where the solubility of dopants is limited and they cannot be introduced during growth. However, very little is known about the fundamental question whether implants are incorporated on proper lattice sites in the perovskites (substitutional sites of element A, substitutional sites of element B, substitutional O sites, regular interstitial sites or randomly dispersed). In this paper we have investigated the

possibilities for ion implantation doping of SrTiO₃, using an approach that mainly applied nuclear techniques, complemented by some non-nuclear characterization methods.

2. RESULTS

2.1. Annealing of radiation damage in SrTiO₃

The annealing of radiation damage in SrTiO₃ was investigated using emission channelling (EC) lattice location of $8 \times 10^{14} \text{ cm}^{-2}$ implanted radioactive ⁸⁹Sr, by means of the Rutherford Backscattering/Channelling (RBS/C) technique following ⁵⁶Fe implantation (10^{15} – 10^{16} cm^{-2}), by measuring the photoluminescence effect of ⁸⁹Sr-implanted SrTiO₃, and, indirectly, by investigating the electrical field gradient experienced by implanted ^{111m}Cd using the method of perturbed angular correlation (PAC).

Figure 1 shows the normalized β^- emission channelling yield measured along the major crystallographic directions of SrTiO₃ as a function of annealing temperature following room temperature implantation of $8 \times 10^{14} \text{ cm}^{-2}$ of the radioactive isotope ⁸⁹Sr ($t_{1/2} = 50.5 \text{ d}$) with 60 keV. As was to be expected the measured channelling patterns (not shown) were characteristic for the incorporation of ⁸⁹Sr on substitutional Sr sites. The analysis of this experiment is still in progress and should result in quantitative information on the fraction of the implanted ⁸⁹Sr atoms incorporated on substitutional Sr sites as a function of annealing temperature. Note that an increase in this fraction is directly reflected by an increase in the axial electron emission channelling yields. The data shown in Fig. 1 hence illustrates the relative increase of the implanted Sr fraction on substitutional sites. Since the implanted radioactive ⁸⁹Sr atoms are subject to the same annealing processes as displaced Sr host atoms, we get direct information on the recovery of the Sr sublattice of the crystal. In the as-implanted state and for annealing up to 200°C, emission channelling effects are almost absent, which is characteristic for ⁸⁹Sr probe atoms occupying random lattice sites in a highly damaged neighbourhood, such as would be expected for a sample which has been turned nearly but not fully amorphous. The emission channelling effects and hence the substitutional Sr fraction increased in a broad recovery step which starts above 200°C and extends beyond 1000°C.

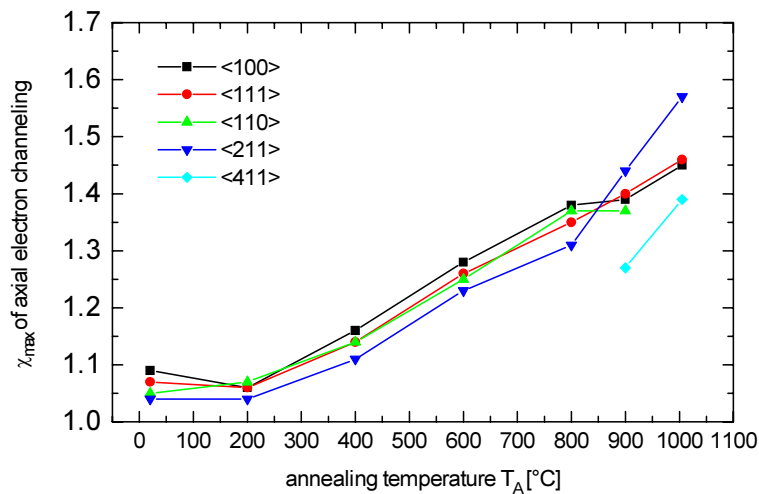


FIG. 1. Normalized electron emission channelling yield χ_{\max} measured along the major crystallographic directions of SrTiO₃ as a function of annealing temperature T_A (10 min in vacuum up to 900°C and 30 min in air at 1000°C) following room temperature implantation of $8 \times 10^{14} \text{ cm}^{-2}$ ⁸⁹Sr with 60 keV energy.

A similar result was obtained in the RBS/C experiments following 60 keV ^{56}Fe implantations at fluences of $1 \times 10^{15} \text{ cm}^{-2}$ and $5 \times 10^{15} \text{ cm}^{-2}$. The RBS/C minimum yield $\chi_{\min}(\text{Sr})$, resulting from the backscattering of 2 MeV He^+ particles at Sr atoms of the sample when the He beam is aligned along the major crystallographic directions, is a measure for the structural quality of the single-crystalline sample (Fig. 2). The fact that RBS/C minimum yields are up to around 75–100% in the as-implanted state shows that the SrTiO_3 lattice is almost amorphized. While following annealing to 900°C the RBS/C minimum yields improved considerably to 8–18%, only 1050°C and 1250°C annealing reduced them to ~4% and ~2.5%, respectively, which is similar to those found in a virgin crystal (~2%). It has been reported in the literature that amorphous SrTiO_3 recrystallizes at a temperature around 400–600°C [6]–[14]. Our experiments have shown that significantly higher temperatures (~1000–1200°C) are needed in order to restore the crystalline quality of the lattice to similar levels as in virgin crystals. Since the 1970s it is a well-known rule of thumb of semiconductor processing that annealing at roughly 2/3 of the melting temperature T_{melt} is needed in order to fully recover from damage and activate implanted electrical dopants. For SrTiO_3 , with its high melting temperature of 2080°C = 2353 K, one would therefore expect that annealing temperatures around 1300°C are needed in order to completely restore crystalline order, which indeed is the case. Although it is an oxide and not a conventional semiconductor, SrTiO_3 , therefore also seems to follow the 2/3 T_{melt} trend.

It is hence also not so surprising that the annealing behaviour of structural defects was reflected in the recovery of the optical properties of SrTiO_3 , which was investigated in a Sr-implanted sample by means of photoluminescence (PL) (Fig. 3). The PL measurements revealed that the near band-edge luminescence (line A in Fig. 3) reappeared only after annealing around 800°C and that the luminescence further improved upon annealing at 1000°C. Several broad emission bands in the visible region have been reported for SrTiO_3 , most prominently a green emission band centred around 2.4–2.5 eV or ~520 nm [12], [15], [16]. However, detailed information on sharp emission lines in SrTiO_3 , such as indicated by letters B-G in Fig. 3, is to be found in the literature only for a couple of centers, mostly related to the rare earths. Since no foreign atoms were implanted into this sample, the sharp emission lines are either due to crystal defects resulting from the implantation process, e.g. Sr interstitials, or to impurities which were already present in the as-grown sample. This is currently under further investigation.

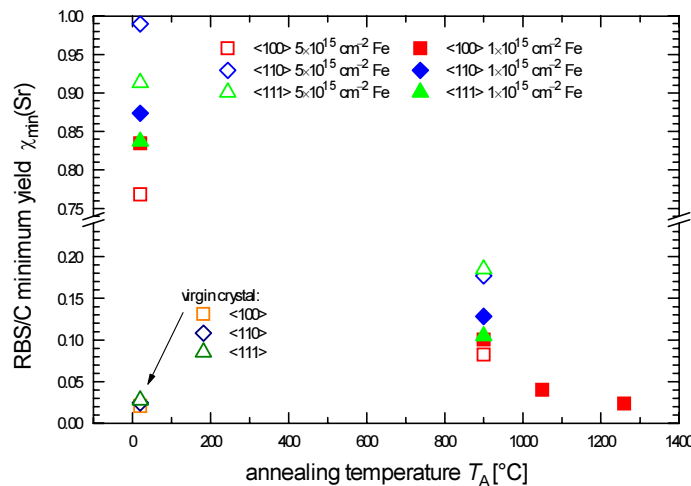


FIG. 2. 2 MeV He^+ Rutherford Backscattering/Channelling (RBS/C) minimum yield $\chi_{\min}(\text{Sr})$ along various crystallographic directions of $1 \times 10^{15} \text{ cm}^{-2}$ and $5 \times 10^{15} \text{ cm}^{-2}$ Fe-implanted SrTiO_3 as a function of annealing temperature T_A (30 min in air). Please note the break in the scale of the y-axis.

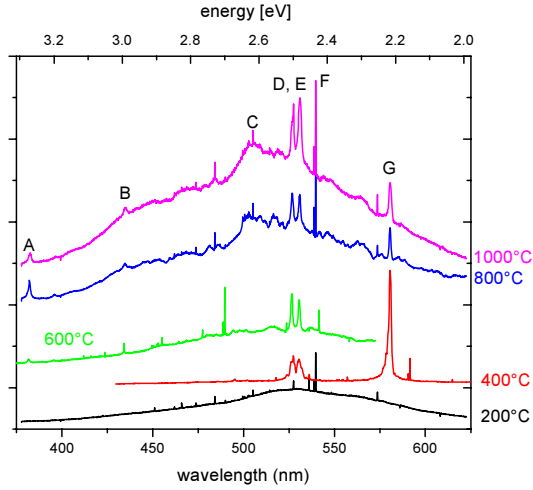


FIG. 3. Visible PL spectra of $\sim 10^{15} \text{ cm}^{-2}$ Sr-implanted SrTiO_3 at 1.6 K below its band edge (3.27 eV corresponding to 379 nm) measured as a function of annealing temperature (20 min in air.) Above-band gap excitation was achieved using the 325 nm line of a HeCd laser and the luminescence detected with a grating of 150 grooves / mm.

The recovery of point defects in the neighbourhood of implanted ^{111}mCd ($t_{1/2} = 49 \text{ m}$) probe atoms in pure SrTiO_3 and 2% Nb-doped SrTiO_3 was studied using the perturbed angular correlation (PAC) technique [17]. For ^{111}mCd probe atoms occupying ideal cubic sites one expects a time-dependent anisotropy signal $R(t)$ which is constant at $R(t) \approx 0.08$, i.e. undamped and unmodulated, while a strongly damped $R(t)$ signal is characteristic to probe atoms in strongly disordered surroundings, where they are subject to a superposition of various electrical field gradients resulting from nearby defects such as vacancies or interstitials. The PAC experiments (Fig. 4) revealed that in the as-implanted state the ^{111}mCd probe atoms are subject to a mixture of strong electrical field gradients characteristic for heavily perturbed crystalline surroundings. Annealing at 720°C removes part of the neighbouring defects, thus reducing the damping of $R(t)$ somewhat, while further annealing at 1000°C considerably flattens the $R(t)$ curve. The situation is then characteristic for 95% of the probe atoms subject to a narrow distribution of weak electrical field gradients, which is interpreted as emitter atoms on slightly perturbed cubic sites.

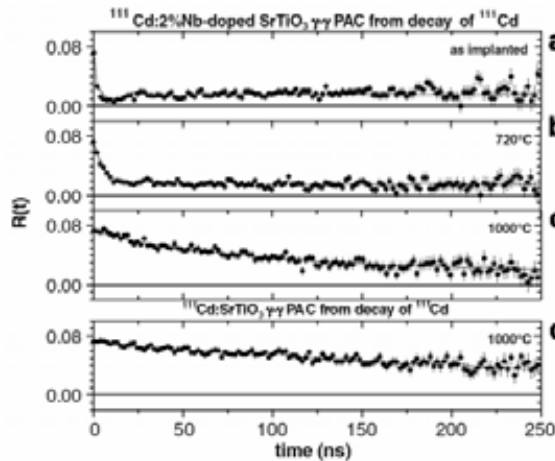


FIG. 4. Time dependent anisotropy $R(t)$ of the 151–245 keV $\gamma\text{-}\gamma$ cascade of ^{111}mCd in 2% Nb-doped SrTiO_3 as-implanted (a) and after annealing the sample for 20 min at 720°C (b), and 1000°C (c). The anisotropy function of ^{111}mCd in undoped SrTiO_3 following annealing at 1000°C is shown in panel (d). From Ref. [17] © Elsevier Science.

2.2. Fe as a magnetic dopant in SrTiO₃

A combination of structural (EC, RBS/C) and magnetic characterization methods (SQUID) was used in order to investigate the properties of Fe-implanted SrTiO₃, which is a candidate for a dilute magnetic semiconductor system at room temperature [2]. A virgin SrTiO₃ sample was implanted with a low fluence ($1 \times 10^{13} \text{ cm}^{-2}$) of 60 keV radioactive ⁵⁹Fe ($t_{1/2} = 44 \text{ d}$). In addition, three SrTiO₃ samples were first implanted with stable ⁵⁶Fe (60 keV) with the following fluences: $1 \times 10^{15} \text{ cm}^{-2}$, $5 \times 10^{15} \text{ cm}^{-2}$, and $1 \times 10^{16} \text{ cm}^{-2}$, and subsequently implanted with additional radioactive ⁵⁹Fe. The lattice location of ⁵⁹Fe was then investigated in all four samples using the β^- emission channelling technique as a function of annealing temperature. Moreover, the structural quality of the $1 \times 10^{15} \text{ cm}^{-2}$ and $5 \times 10^{15} \text{ cm}^{-2}$ implanted samples were evaluated using RBS/C, which has already been discussed above. The EC lattice location results have been fully analyzed so far only for the low-fluence $1 \times 10^{13} \text{ cm}^{-2}$ sample [Figs. 5 and 6]. In this case Fe was found to occupy mainly two lattice sites: ideal substitutional Ti sites (S_{Ti}) and sites which are displaced 0.4–0.7 Å along $\langle 100 \rangle$ directions from ideal Ti sites towards substitutional O sites ($S_{\text{Ti}} \rightarrow S_{\text{O}}$). Similar to Cu and Ag (see below), in the as-implanted state Fe also partly occupied octahedral interstitial sites (I_{g}), but these were converted to substitutional sites already following the first annealing step at 300°C. From the fact that the ionic radius of Fe^{3+} (0.64 Å) matches almost perfectly that of Ti^{4+} (0.68 Å) it is understandable that Fe is incorporated at or near Ti sites. It is also well-known that $\text{Fe}^{3+}_{\text{Ti}}$ easily pairs with nearest-neighbour oxygen vacancies V_{O} , resulting in an $\text{Fe}^{3+}_{\text{Ti}} - V_{\text{O}}$ defect, whose electron paramagnetic resonance (EPR) signal has been well-documented in the literature [18],[19]. It has been suggested that the Fe atom within the $\text{Fe}_{\text{Ti}} - V_{\text{O}}$ defects moves around 0.2 Å along $\langle 100 \rangle$ directions towards the V_{O} [19]. We therefore attribute the $\langle 100 \rangle$ -displaced Fe sites observed in the EC experiments to $\text{Fe}_{\text{Ti}} - V_{\text{O}}$ defects, however, our lattice location results show that the Fe displacement is actually much larger than 0.2 Å.

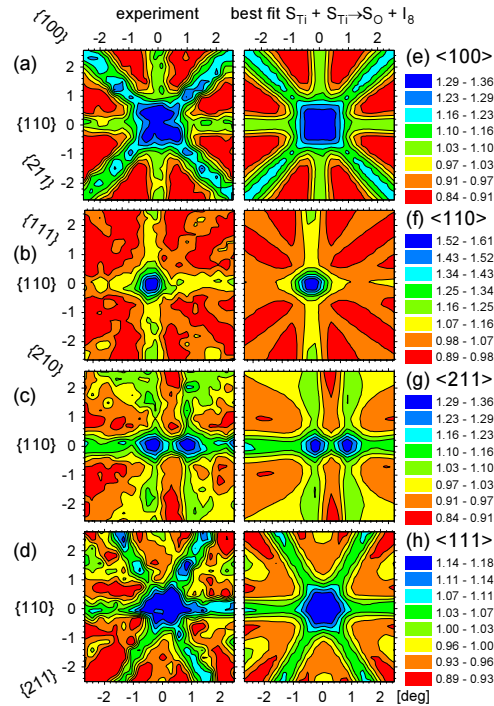


FIG. 5. Angular distributions of β^- particles emitted from ⁵⁹Fe in SrTiO₃ around the (a) $\langle 100 \rangle$, (b) $\langle 110 \rangle$, (c) $\langle 211 \rangle$ and (d) $\langle 111 \rangle$ directions following room temperature implantation and vacuum annealing for 10 min at 750°C. The best fits of the simulated patterns to the experimental ones are shown in Fig. 1(e)-(h).

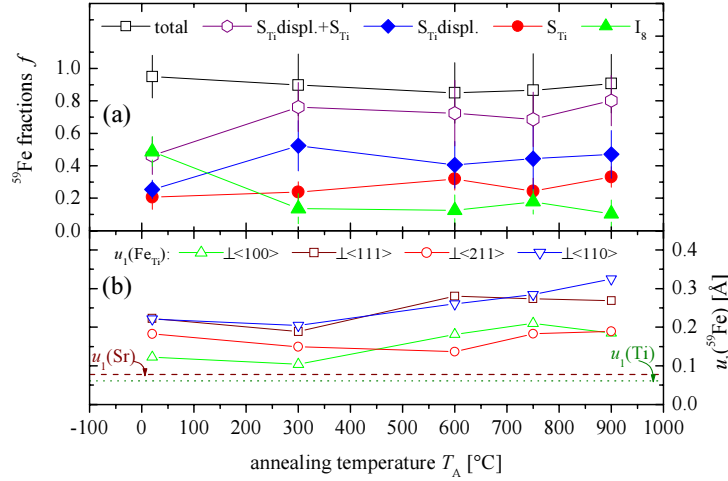


FIG. 6. (a) Substitutional fractions of Fe occupying ideal Ti (S_{Ti}), $\langle 100 \rangle$ -displaced Ti ($S_{\text{Ti}} \text{ displ.}$) and octahedral interstitial (I_8) sites and the sum of those sites as a function of annealing temperature in vacuum for 10 min. (b) The rms displacements perpendicular to $\langle 100 \rangle$, $\langle 111 \rangle$, $\langle 211 \rangle$ and $\langle 110 \rangle$ axial directions calculated from the sum of ($S_{\text{Ti}} + S_{\text{Ti}} \text{ displ.}$). The dotted and dashed lines represent the room temperature Sr and Ti vibration amplitudes, respectively.

Following the emission channelling experiments the macroscopic magnetic moments of the $1 \times 10^{15} \text{ cm}^{-2}$ and $5 \times 10^{15} \text{ cm}^{-2}$ implanted samples were characterized by means of a superconducting quantum interference device (SQUID) [20]. The results showed that in the $1 \times 10^{15} \text{ cm}^{-2}$ implanted sample most of the Fe forms paramagnetic defects, while in the $5 \times 10^{15} \text{ cm}^{-2}$ implanted sample also ferromagnetic hysteresis was observed, with an estimated magnetic moment per Fe atom of $\sim 7.5 \mu\text{B}$. The results indicate that Fe implantation can produce ferromagnetism in SrTiO_3 , but it seems that $>2\%$ of Ti atoms need to be replaced by Fe atoms.

2.3. Lattice location of group Ib impurities Cu and Ag in SrTiO_3

The two group Ib elements Cu and Ag are potential acceptor impurities in SrTiO_3 if incorporated on Sr sites. We have studied the lattice location of implanted ^{67}Cu ($t_{1/2} = 63 \text{ h}$) and ^{111}Ag ($t_{1/2} = 7.5 \text{ d}$) [21] by means of β^- emission channelling following 60 keV ion implantation at fluences of $5 \times 10^{12} - 1 \times 10^{13} \text{ cm}^{-2}$. In both cases it was found that these impurities are amphoteric, i.e. they occupy both substitutional Sr and Ti sites. However, while Cu preferred Ti lattice sites, the majority of Ag was found on Sr sites. As an example, Fig. 7 shows the emission channelling patterns of the ^{111}Ag implanted sample following 900°C annealing in comparison to the best fit results, which were obtained for $\sim 65\%$ of Ag on Sr and $\sim 20\%$ on Ti sites. The preference of Ag for the Sr sites is best illustrated by the $\langle 211 \rangle$ emission channelling pattern, as it is shown in Fig. 7 (d). For this direction, emitter atoms on Sr sites result in a single channelling peak, while emitter atoms on Ti sites produce a double peak, as was for instance observed for ^{59}Fe and is shown in Fig. 5 (c). The ^{111}Ag fractions on the considered lattice sites (Sr, Ti and interstitial) are shown for the whole annealing sequence in Fig. 8. The lattice site preferences of Cu and Ag can be qualitatively understood from the ionic radii of Sr^{2+} (1.13 Å), Ti^{4+} (0.68 Å), Cu^{1+} (0.96 Å), Cu^{2+} (0.69 Å), and Ag^{1+} (1.26 Å), which favours incorporation of Cu^{2+} on Ti sites and of Ag^{1+} on Sr sites. Also in both cases, in the room-temperature as-implanted state, fractions around 20% of the emitter atoms occupied octahedral interstitial sites I_8 , from which they disappeared, however, already at annealing temperatures around 300°C. Our results suggest that, while Cu and Ag are both problematic acceptor dopants in SrTiO_3 due to their amphoteric nature, Ag is far more promising in that respect.

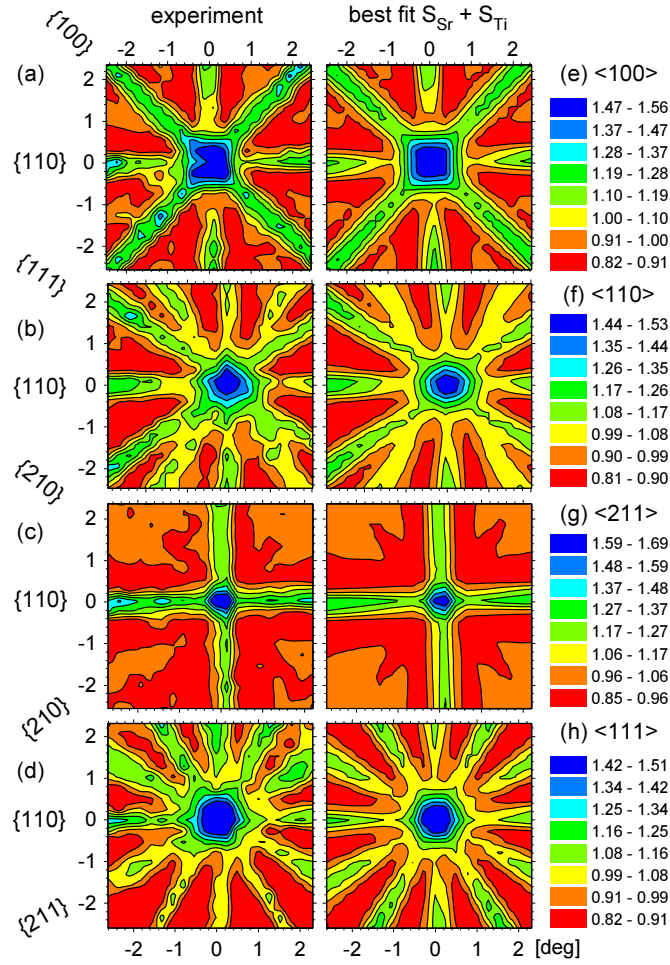


FIG.7. Angular distributions of β^- particles emitted from ^{111}Ag in SrTiO_3 around the (a) $\langle 100 \rangle$, (b) $\langle 110 \rangle$, (c) $\langle 211 \rangle$ and (d) $\langle 111 \rangle$ directions following room temperature implantation of ^{111}Ag and annealing for 10 min at 900°C . The best fits of the simulated patterns to the experimental ones are shown in Fig.1(e)-(h).

2.4. Lattice location of rare earths in SrTiO_3

Rare earth (RE) doped SrTiO_3 is currently of interest with respect to applications as a phosphor material. In particular, Pr-doped SrTiO_3 is considered to be a suitable red phosphor for field-emission displays [22]. Moreover, Pr-doping has also been reported to induce ferroelectricity in SrTiO_3 [23][24]. It is often assumed that in perovskites ABO_3 the trivalent rare earths RE^{3+} substitute for the A^{2+} cation forming a donor impurity. In SrTiO_3 , this is also suggested by the similarity of the ionic radii of Sr^{2+} (1.13 Å) and RE^{3+} (0.93–1.11 Å), while there is a larger misfit between Ti^{4+} (0.68 Å) and RE^{3+} . However, it has been controversially discussed whether RE^{3+} can also substitute for the B^{4+} cation and form an acceptor and for many rare earths there exists spectroscopic evidence of multiple sites in perovskites [12][24][25][26][27][28]. Apart from our interest in fundamental issues of doping perovskites by means of ion implantation, it is hence interesting to investigate the lattice location of rare earths in order to understand in more detail their optical properties when incorporated in SrTiO_3 .

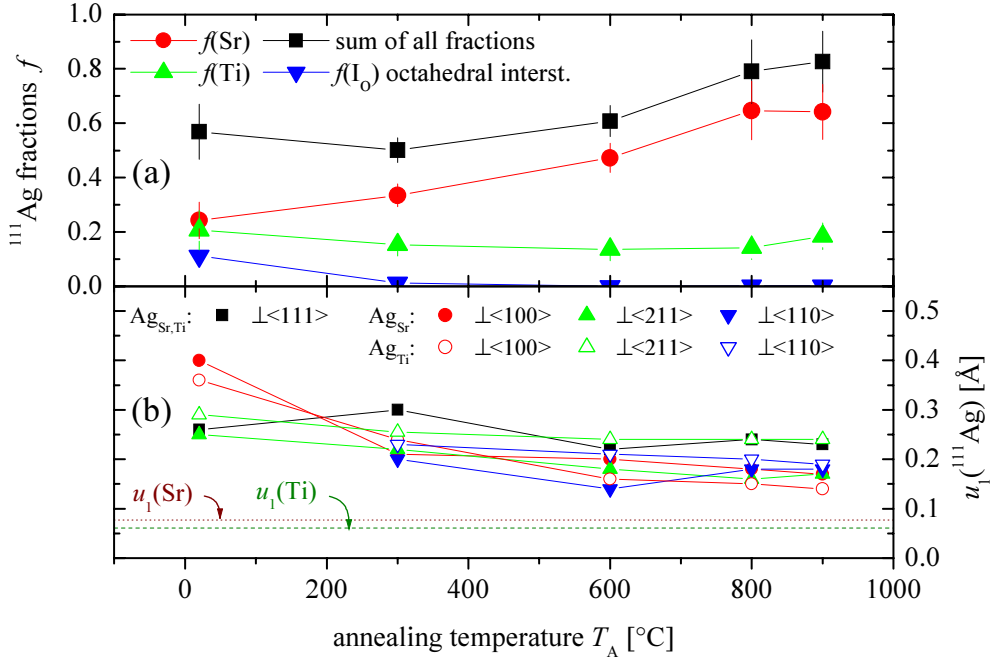


FIG. 8. (a) Substitutional fractions of ^{111}Ag occupying Sr, Ti and octahedral interstitial (I_8) sites and the sum of all those sites as a function of annealing temperature in vacuum for 10 min. (b) rms displacements from ideal Sr and Ti sites perpendicular to $\langle 111 \rangle$, $\langle 100 \rangle$, $\langle 110 \rangle$ and $\langle 211 \rangle$ axial directions. The dotted and dashed lines represent the room temperature Sr and Ti vibration amplitudes, respectively. From Ref [21]. © Elsevier Science.

Two SrTiO_3 samples were implanted with the rare earth isotopes $^{169}\text{Yb} \rightarrow ^{169}\text{Tm}^*$ ($t_{1/2} = 31$ d) and ^{141}Ce ($t_{1/2} = 32$ d) with fluences of $1 \times 10^{14} \text{ cm}^{-2}$. The lattice location of $^{169}\text{Tm}^*$ and ^{141}Ce were then determined by means of the conversion electron ($^{169}\text{Yb} \rightarrow ^{169}\text{Tm}^*$) and β^- (^{141}Ce) emission channelling techniques. In the case of $^{169}\text{Yb} \rightarrow ^{169}\text{Tm}^*$ the as-implanted sample was characterized by 28% of probe atoms on Ti and 13% on Sr sites. During annealing these fractions steadily increased until reaching 50% on Ti sites and 48% on Ti sites following 900°C annealing. The ^{141}Ce experiment yielded qualitatively similar results but has not been analyzed in detail yet. We have previously established the amphoteric character of Er in SrTiO_3 by means of conversion electron emission channelling experiments using $^{167}\text{Tm} \rightarrow ^{167\text{m}}\text{Er}$ ($t_{1/2} = 9.5$ d) [29]. In this case the maximum annealing temperature had been 600°C, after which $\sim 39\%$ of $^{167\text{m}}\text{Er}$ was found on Ti sites and $\sim 23\%$ on Sr sites. The rare earths are hence also amphoteric impurities in SrTiO_3 , being able to occupy both types of cation sites. A similar amphoteric behaviour has long ago been suggested from the analysis of the optical spectra due to Sm^{3+} in the perovskite material BaTiO_3 [25], and later also for Er^{3+} in SrTiO_3 [12].

3. CONCLUSIONS

Our investigations have explored the possibilities for doping of SrTiO_3 by means of ion implantation. One of our major findings is that the annealing temperature for full recovery of implantation damage in SrTiO_3 is around 1000–1200°C, which is much higher than the 400–600°C recrystallization temperature of amorphous SrTiO_3 reported in the literature. Although it is an oxide and not a conventional semiconductor, SrTiO_3 therefore also seems to follow the well-known rule of thumb in semiconductor processing, that annealing at temperatures around 2/3 of the melting temperature T_{melt} is needed in order to fully recover from implantation

damage. The second major finding is that most of the implanted foreign atoms in SrTiO₃ (with the exception of Fe) behave in an amphoteric way, i.e. they partially substitute for Sr and Ti cations, which complicates site-specific doping attempts in this material. Besides the chemical properties, the ionic size is a decisive factor in determining the preferred lattice position. Although being amphoteric, most of the investigated foreign atoms preferred to substitute for the cation which best matched their ionic size. However, the rare earth elements apparently fall somewhat out of this general trend since they do not seem to have a pronounced preference for Sr sites, which would be expected from the better match of the ionic radii of Sr²⁺ and RE³⁺.

ACKNOWLEDGMENTS

This work was funded by the Portuguese Foundation for Science and Technology (FCT, projects POCI-FP-81921-2007 and PTDC-FIS-66262-2006) and by the European Commission (EURONS project RII3-CT-2004-506065). We are grateful to the ISOLDE collaboration for the beam time made available at the ISOLDE/CERN facility. A.C.M., C.P.M. and L.P. acknowledge FCT for their PhD scholarships.

REFERENCES

- [1] NORTON, D.P., *Synthesis and properties of epitaxial electronic oxide thin-film materials*, Mater. Sci. Eng. R 43 (2004) 139.
- [2] PEARTON, S.J., HEO, W.H., IVILL, M., NORTON, D.P., STEINER, T., *Dilute magnetic semiconducting oxides*, Semicond. Sci. Tech. 19 (2004) R59.
- [3] RAMIREZ, A.P., *Colossal Magnetoresistance*, J. Phys. C 9 (1997) 8171.
- [4] EISENBEISER, K., FINDER, J.M., YU, Z., RAMDANI, J., CURLESS, J.A., HALLMARK, J.A., DROOPAD, R., OOMS, W.J., SALEM, L., BRADSHAW, S., OVERGAARD, C.D., *Field effect transistors with SrTiO₃ gate dielectric on Si*, Appl. Phys. Lett. 76 (2000) 1324.
- [5] FÖRST, C.J., ASHMAN, C.R., SCHWARZ, K., BLÖCHL, P.E., *The interface between silicon and a high-k oxide*, Nature 427 (2004) 53.
- [6] WHITE, C.W., BOATNER, L.A., SKLAD, P.S., MC HARGUE, C.J., RANKIN, J., FARLOW, G.C., AZIZ, M.J., *Ion implantation and annealing of crystalline oxides and ceramic materials*, Nucl. Instrum. Methods B 32 (1988) 11.
- [7] McCALLUM, J.C., RANKIN, J., WHITE, C.W., BOATNER, L.A., *Time resolved reflectivity measurements in Pb-implanted SrTiO₃*, Nucl. Instrum. Methods B 46 (1990) 98.
- [8] MORETTI, P., CANUT, B., RAMOS, S.M.M., THEVENARD, P., GODEFROY, G., *Niobium implantation effects in BaTiO₃ and SrTiO₃*, Nucl. Instrum. Methods B 65 (1992) 264.
- [9] WANG, F., BADAYE, M., YOSHIDA, Y., MORISHITA, T., *Characterization of the recovery of SrTiO₃ surface by ion channeling*, Nucl. Instrum. Methods B 118 (1996) 547.
- [10] THEVUTHASAN, S., JIANG, W., SHUTTHANANDAN, V., WEBER, W.J., *Accumulation and thermal recovery of disorder in Au²⁺-irradiated SrTiO₃*, J. Nucl. Mater. 289 (2001) 204.
- [11] MELDRUM, A., BOATNER, L.A., WEBER, W.J., EWING, R.C., *Amorphization and recrystallization of the ABO₃ oxides*, J. Nucl. Mater. 300 (2002) 242.

- [12] MONTEIRO, T., SOARES, M.J., BOEMARE, C., ALVES, E., CORREIA, J.G., *Optical activity and damage recovery of erbium implanted strontium titanate*, Radiat. Eff. Def. Solids 157 (2002) 1071.
- [13] ZHANG, Y., LIAN, J., WANG, C.M., JIANG, W., EWING, R.C., WEBER, W.J., *Ion-induced damage and electron-beam-enhanced recrystallization in SrTiO₃*, Phys. Rev. B 72 (2005) 094112/1–8.
- [14] THEVUTHASAN, S., SHUTTHANANDAN, V., ZHANG, Y., *Applications of high energy ion beam techniques in environmental science: Investigation associated with glass and ceramic waste forms*, J. Electron Spectroscopy 150 (2006) 195.
- [15] GRABNER, L., *Photoluminescence in SrTiO₃*, Phys. Rev. 177 (1969) 1315.
- [16] LEONELLI, R., BREBNER, J.L., *Time-resolved spectroscopy of the visible emission band in strontium titanate*, Phys. Rev. B 33 (1986) 8649.
- [17] MARQUES, A.C., CORREIA, J.G., WAHL, U., SOARES, J.C., *Study of point defects and phase transitions in undoped and Nb-doped SrTiO₃ using perturbed angular correlations*, Nucl. Instrum. Methods B 261 (2007) 604.
- [18] Kirkpatrick, E.S., Müller, K.A., Rubins, R.S., *Strong axial electron paramagnetic resonance spectrum of Fe³⁺ due to nearest neighbor charge compensation*, Phys. Rev. 135 (1964) A86.
- [19] SIEGEL, E., MÜLLER, K.A., *Structure of transition-metal-oxygen–vacancy pair centers*, Phys. Rev. B. 19 (1979) 109.
- [20] PEREIRA, L., *Searching room temperature ferromagnetism in wide band gap semiconductors*, Licenciatura thesis, Departamento Física, Faculdade de Ciências, Universidade do Porto, 2007.
- [21] MARQUES, A.C., WAHL, U., CORREIA, J.G., RITA, E., SOARES, J.C., *Lattice location and perturbed angular correlation studies of implanted Ag in SrTiO₃*, Nucl. Instrum. Methods B 249 (2006) 882.
- [22] YAMAMOTO, H., OKAMOTO, S., KOBAYASHI, H., *Luminescence of rare-earth ions in perovskite-type oxides: from basic research to device applications*, J. Lumin. 100 (2002) 325.
- [23] DURAN, A., DIAZ, J.A., SIQUEIROS, J.M., *Ferroelectricity at room temperature in Pr-doped SrTiO₃*, J. Appl. Phys. 97 (2005) 104109/1–4.
- [24] RANJAN, R., HACKL, R., CHANDRA, A., SCHMIDBAUER, E., TROTS, D., BOYSEN, H., *High-temperature relaxor ferroelectric behavior in Pr-doped SrTiO₃*, Phys. Rev. B 76 (2007) 224109/1–6.
- [25] MAKISHIMA, S., HASEGAWA, K., SHIONOYA, S.J., *Luminescence of Sm³⁺ in BaTiO₃ matrix*, Phys. Chem. Solids 23 (1962) 749.
- [26] COCKROFT, N.J., LEE, S.H., WRIGHT, J.C., *Site-selective spectroscopy of defect chemistry in SrTiO₃, Sr₂TiO₄, and Sr₃Ti₂O₇*, Phys. Rev. B 44 (1991) 4117.
- [27] COCKROFT, N.J., WRIGHT, J.C., *Local- and distant-charge compensation of Eu³⁺ ions in defect centers of SrTiO₃*, Phys. Rev. B 45 (1992) 9642.
- [28] KNOTT, L.J., COCKROFT, N.J., WRIGHT, J.C., *Site-selective spectroscopy of erbium-doped SrTiO₃, Sr₂TiO₄, and Sr₃Ti₂O₇*, Phys. Rev. B 51 (1995) 5649.
- [29] ARAÚJO, J.P., WAHL, U., ALVES, E., CORREIA, J.G., MONTEIRO, T., SOARES, J., SANTOS, L., and the ISOLDE collaboration, *Erbium implantation into strontium titanate*, Nucl. Instrum. Methods B 191 (2002) 317.

ION BEAM MODIFICATION OF SPUTTERED METAL NITRIDE THIN FILMS

A Study of the Induced Microstructural Changes

M. Milosavljević, D. Peruško, M. Popović, and M. Novaković

VINČA Institute of Nuclear Sciences, Belgrade 11001, P.O. Box 522, Serbia

Abstract. Single CrN and TiN and multilayered AlN/TiN and Al/Ti thin film structures ($t = 240\text{--}280$ nm) deposited on Si were irradiated with 120–200 keV Ar^+ ions to the fluences ranging from 1×10^{15} to 4×10^{16} ions/cm². The metallic Al/Ti multilayered structure was also irradiated with high fluence ($1\text{--}2 \times 10^{17}$ /cm²) nitrogen ions at 200 keV, in order to study interface mixing and formation of nitrides. Single component CrN and TiN thin films were found to grow in the form of a very fine polycrystalline columnar structures. Individual crystal grains were of the order of a few tens of nm in diameter, stretching from the substrate to the surface. After ion irradiation, the layers retain their polycrystalline structure, although the columns become disconnected, the resulting structures consisting of larger grains and nano-particles of the same phase. The implanted samples displayed higher electrical resistivity, presumably due to a higher concentration of point defects and the presence of nano-particles. In Al/Ti and AlN/TiN multilayers irradiated with Ar ions, the as-deposited structures exhibit well-defined, isolated polycrystalline Al and Ti, or AlN and TiN layers, with sharp interfaces. In the metallic system ion irradiation induced interface mixing which progressed with increasing the ion fluence. Mixing was most pronounced at the interfaces that are located around the projected ion range. The multilayered structure was essentially preserved, but the implanted samples exhibit much larger crystal grains. Also, the formation of lamellar columns stretching over a number of individual layers was observed. The AlN/TiN multilayered structures exhibited no measurable interface mixing on Ar irradiation, attributable to the nature of interatomic bonding and to mutual immiscibility of AlN and TiN. High fluence nitrogen ion irradiation of Al/Ti multilayers results in both the introduction of nitrogen into the structures as well as a high level of their intermixing. A multilayered structure was preserved, consisting of a compositionally graded ternary (Al,Ti)N multilayers, with individual layers being either Al or Ti rich.

1. INTRODUCTION

Metal-nitride thin films have many unique properties and are interesting for wide and diverse applications, from electronics, tribology, power, to bio-medicine and environment. In general, their basic functional properties depend on their microstructure, i.e. the mean grain size, preferred orientation, grain boundaries, crystalline defects, surface and interface morphology. Over the last decades, physical or chemical vapour deposition processes were established as reliable for depositing good quality TiN, CrN or AlN hard coating materials [1][2][3]. On the other hand, nano-scaled multilayered coatings of metals and metal-nitrides, with individual layer thickness from a few to a few tens of nanometers, offer advanced properties compared to thick single layers, in providing the same performance at much lower thickness [4][5][6]. They give numerous advantages over single component coatings, such as much higher hardness and strength due to a large number of interfaces, possibilities to form super lattices, graded composition, more dense and less porous structures [7][8][9].

Modern surface treatments involve the use of ion beams in the processes such as ion implantation, plasma ion immersion, or ion beam assisted deposition. The use of ion beam processing in fabrication of various thin film structures can be beneficial towards achieving better adhesion to the substrate, relaxing the interface stresses, increasing the film density and decreasing porosity. Ion implantation was proven as a very powerful technique for improving tribological properties, both when applied directly on the processed materials or on previously

deposited coatings [10]. In many ion-beam-mixing experiments it was shown that ion irradiation can induce interfacial reactions in layered systems at much lower temperatures than required in thermal treatments. However, so far ion beam processing was mainly used on single component layers, while there is very limited evidence on ion beam treatment of multilayered structures.

In this work we have studied ion implantation effects on both single component layers and on multilayers. Single component CrN and TiN films were deposited on Si wafers and subsequently irradiated with Ar ions. The ion energy was chosen according to the ion range, to ensure that all implanted ions were stopped within the deposited films. The interest here was to study the effects of ion irradiation on the micro-structural changes in the films. Another set of experiments involved investigation of the influence of nitrogen pre-implantation of stainless steel substrates on the properties of post-deposited TiN coatings. Third set of experiments was devoted to ion beam modification of multilayered Al/Ti and AlN/TiN thin films. The structures that were prepared consisted of 10 alternate layers of Al and Ti, or AlN and TiN, deposited on Si wafers to a total thickness of ~250 nm. Irradiations of Al/Ti and AlN/TiN multilayers were performed Ar ions. The aim was to study irradiation stability of these structures, by comparing the behaviour of pure metal and metal-nitride multilayers. For Al/Ti multilayered structures we also investigated ion beam mixing and synthesis of metal-nitrides, by high fluence implantation of nitrogen ions.

2. EXPERIMENTAL PROCEDURES

Metal-nitride films (CrN, TiN and AlN) were deposited by reactive ion sputtering and pure metal films (Al and Ti) by d.c. ion sputtering, in a Balzers Sputtron II system. The substrates used were (100) Si wafers. Single component films were TiN and CrN, and multilayered structures consisted of 10 alternate layers of AlN and TiN, or Al and Ti. In all cases the total thickness of the deposited structures was from 240–280 nm.

After deposition, the single component films were implanted with 120 keV Ar ions, to the fluences of 1×10^{15} and 1×10^{16} ions/cm². Multilayers, AlN/TiN and Al/Ti were implanted with 200 keV Ar, to 5×10^{15} - 4×10^{16} ions/cm². Ion irradiations were performed at room temperature, the ion beam was scanned uniformly over an area of 2×2 cm², and the beam current was kept at ~ 1 μ A/cm². Metallic multilayers, Al/Ti, were also implanted with 200 keV nitrogen ions, to 1 – 2×10^{17} at/cm². Another set of experiments involved investigation of the influence of nitrogen pre-implantation of stainless steel substrates on the properties of post-deposited TiN coatings.

Structural characterisation of as-deposited and irradiated structures was performed with Rutherford backscattering spectroscopy (RBS), transmission electron microscopy (TEM), X ray diffraction (XRD) and Auger electron spectroscopy (AES). Sheet resistance was measured on single component films, using a four point probe. We also did micro-hardness measurements of TiN coatings deposited on pre-implanted stainless steel substrates, by the Vicker's method.

3. RESULTS

3.1. TiN and CrN films irradiated with 120 keV Ar ions

Microanalysis of single component TiN and CrN layers has shown that in both cases they grow in the form of a very fine polycrystalline columnar structure. Individual columns stretch from the substrate to the surface, while their lateral dimensions are of the order of a few tens of nm. The films deposited at an elevated substrate temperature grow in form of larger crystal grains (i.e. wider columns) compared to those deposited at room temperature (RT). Figure 1 shows a cross-sectional TEM image of a TiN layer deposited on Si at 150°C. Electron diffraction pattern was taken with a focused micro-beam from the TiN layer. It exhibits individual spots lying on the rings that correspond to reflections from (111) and (200) TiN planes, and from the planes with higher indexes. Similar structure was observed in as-deposited Cr-N films.

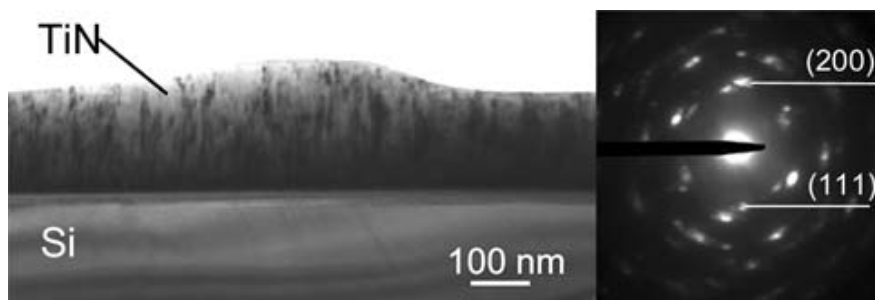


FIG.1. Cross-sectional TEM analysis of a TiN layer deposited on Si at 150°C.

With respect to the nitrogen partial pressure during deposition, TiN films typically form only the TiN phase, which is either over or under stoichiometric (enriched with Ti or N), depending on the deposition parameters. For their growth we have applied the nitrogen partial pressure that yields stoichiometric TiN films, with 1:1 ratio of Ti and N. On the other hand, Cr-N films can grow in form of different phases, most commonly Cr₂N or CrN. Here we have applied three different nitrogen partial pressures during deposition, 2×10^{-4} , 3.5×10^{-4} and 5×10^{-4} mbar. For the two lower partial pressures the grown phase was mainly Cr₂N, while for the highest pressure the layers were stoichiometric CrN. RBS spectra taken from Cr-N films deposited at different nitrogen pressure are shown in Fig. 2.

After deposition the samples were irradiated with 120 keV Ar ions to the fluences of 1×10^{15} and 1×10^{16} ions/cm². Projected range of 120 keV Ar ions in TiN or CrN is $R_p \sim 70$ nm and straggle $R_p \sim 30$ nm, as calculated by the TRIM code [12] and confirmed by RBS analysis. Hence, ion irradiation induced only local atomic rearrangements within the films. After irradiation the layers retain their polycrystalline structure, but the columnar grains, initially stretching from the substrate to the surface, were disconnected. However, higher implanted fluences yielded an increase of the mean grain size, though these larger grains contain point defects and imbedded nano-particles of the same phase. Nano-particles were also observed at grain boundaries between larger grains, as illustrated in Fig. 3.

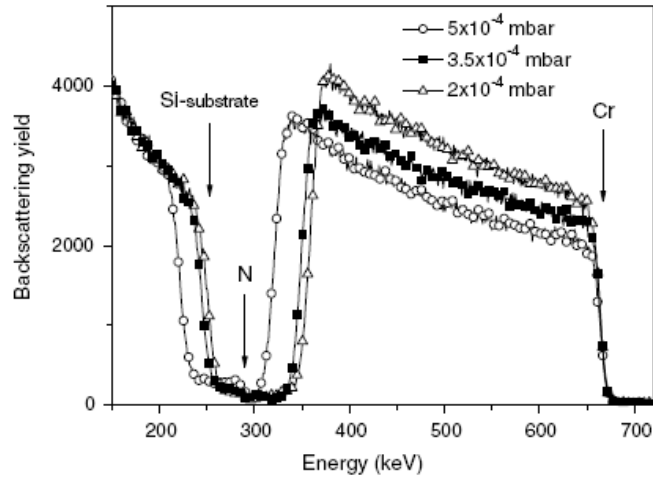


FIG. 2. RBS spectra of CrN samples deposited at different nitrogen partial pressure at RT.

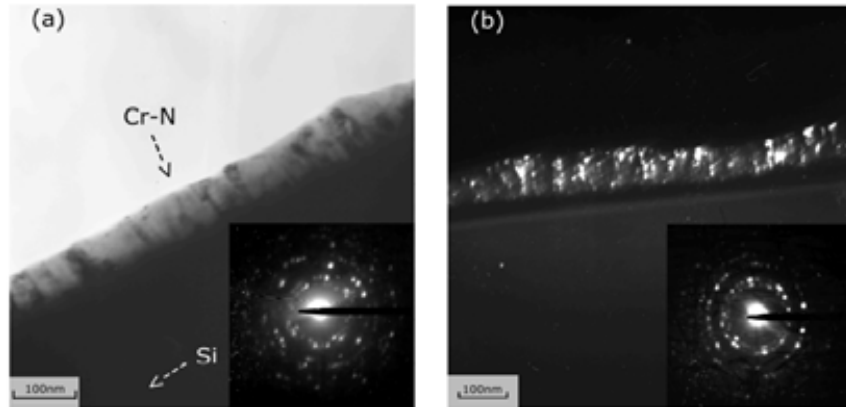


FIG. 3. TEM analysis of Cr-N/Si deposited at 150°C, nitrogen partial pressure of 5×10^{-4} mbar: (a) bright field image of as-deposited sample; (b) dark field image of sample implanted to 1×10^{15} ions/cm².

The results of XRD analysis have shown that in general the mean crystal grain size of the layers decreases after ion irradiation. In TiN layers we also register partial texturing, the preferred orientation changing from (111) to (200), as shown in Fig.4. Electrical resistivity measurements gave consistent results to those from TEM, RBS and XRD analyses. The films grown at an elevated substrate temperature have a lower electrical resistivity, due to larger mean grain size and a lower concentration of grain boundaries. In case of Cr-N films electrical measurements confirmed the transition from a low-resistivity Cr₂N phase to a high-resistivity CrN phase with increasing the nitrogen partial pressure during deposition. Implanted samples have a higher electrical resistivity due to a higher concentration of defects induced by ion irradiation. The results of electrical measurements are plotted in Fig. 5.

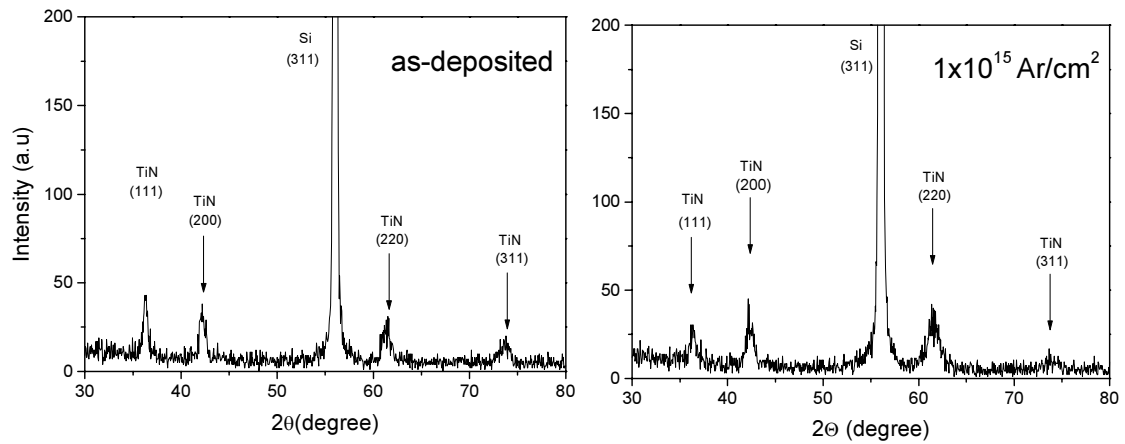


FIG. 4. XRD analysis of as-deposited and implanted TiN films.

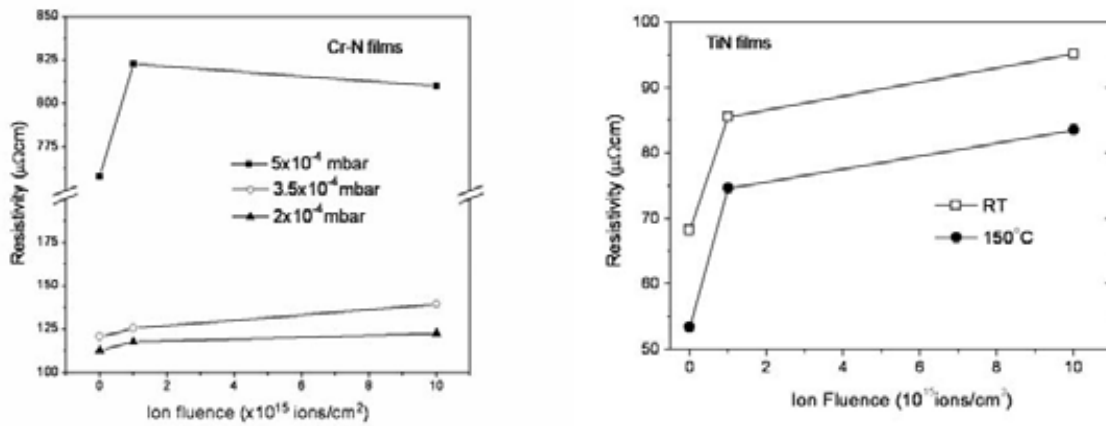


FIG. 5. Electrical resistivity of Cr-N and TiN films as a function of the ion fluence.

3.2. TiN coatings deposited on steel substrates pre-implanted with nitrogen

For the experiments with TiN coatings deposited on stainless steel, it was found that nitrogen pre-implantation of the substrates influences both the microstructure and microhardness of the coatings. The substrates were implanted with 40 keV nitrogen ions to the fluences from 5×10^{16} to 5×10^{17} ions/cm², and the TiN coatings were deposited by reactive sputtering to a thickness of 1.3 μm . Nitrogen implantation to the fluence of 2×10^{17} ions/cm² and higher induced the formation of Fe₂N phase in the near surface region of the substrates. Pre-implantation of the substrates strongly influences the preferred crystal grain orientation of subsequently deposited TiN coatings. Experimental measurements, presented in Fig. 6, show an increase of microhardness of both the substrates and of the deposited coatings with increasing the pre-implantation fluence. Combined ion pre-implantation and deposition of TiN hard coatings increase the microhardness of the starting steel substrates for more than eight times.

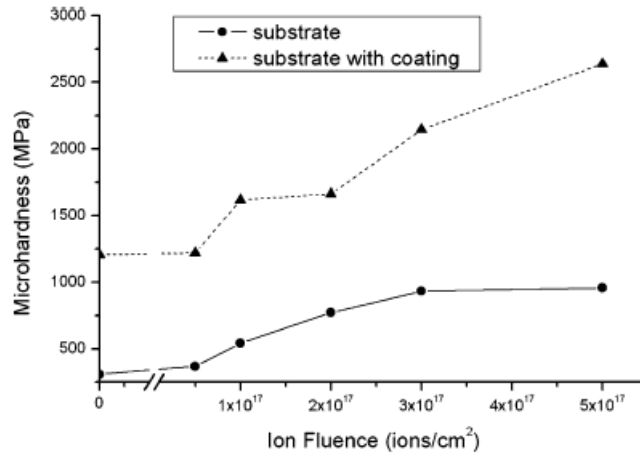


FIG. 6. Measured microhardness values of steel substrates before and after deposition of TiN coatings, as a function of pre-implantation fluence.

3.3. Al/Ti and AlN/TiN multilayers irradiated with Ar ions

Multilayered structures consisted of 10 alternate layers of Al and Ti, or AlN and TiN, deposited on (100) Si wafers to a total thickness of ~ 250 nm. They were irradiated with 200 keV Ar ions to the fluences from 5×10^{15} to 4×10^{16} ions/cm². The projected range of the implanted ions was around mid-depth of the multilayered structures. The as deposited structures exhibited well defined, isolated polycrystalline Al and Ti, or AlN and TiN layers, with sharp interfaces, each being around 25 nm thick. In the metallic system we observed that ion irradiation induces interface mixing, more progressed with increasing the ion fluence. Mixing is most pronounced at the interfaces that are located around the projected ion range. The multilayered structure and the overall surface and interface morphologies were essentially preserved. The estimated mixing rate was found to be close to the value predicted by the ballistic model, unlike the results reported for bilayer systems of the same components, where mixing rates are closer to the predictions of the thermal spike model. Also, the implanted samples exhibit much larger crystal grains, and we observe formation of a lamellar columns stretching over a number of individual layers (Fig. 7).

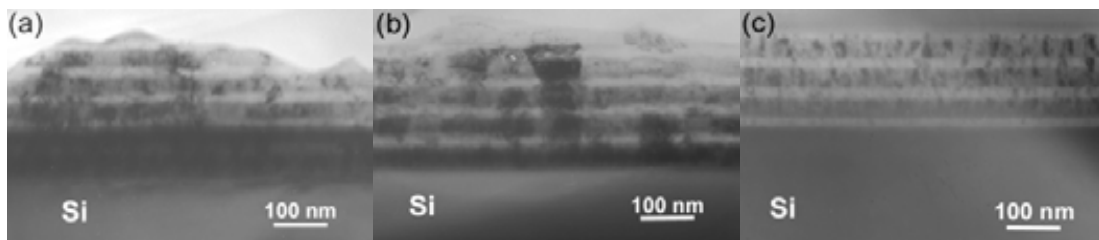


FIG. 7. TEM bright field cross-sectional images: (a) as-deposited Al/Ti; (b) Al/Ti implanted to 2×10^{16} ions/cm²; (c) AlN/TiN implanted to 2×10^{16} ions/cm².

Opposite to Al/Ti system, the AlN/TiN multilayered structures exhibited a remarkable ion irradiation stability. After irradiation with all the applied Ar ion fluences we could not detect any measurable interface mixing. The only change that could be observed was a slight increase of the mean grain size in individual layers. Cross-sectional TEM image of an irradiated sample in Fig. 7 (c) shows well separated AlN and TiN layers with sharp interfaces. Absence of any intermixing was assigned to the nature of interatomic bonding and to mutual immiscibility of AlN and TiN. Extracted Ti depth profiles from RBS analysis of Al/Ti and AlN/TiN structures, implanted with different argon fluences, are shown in Fig. 8.

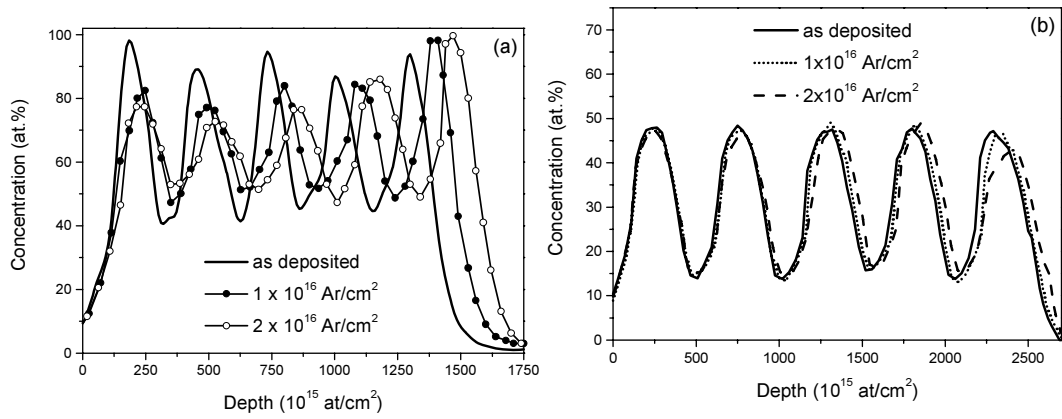


FIG. 8. Extracted point by point Ti depth profiles from Al/Ti (a) and AlN/TiN structures (b).

3.4. High fluence irradiation of Al/Ti multilayers with nitrogen

Irradiation of Al/Ti multilayers was done with 200 keV N₂ ions, to the fluences of 1×10^{17} and 2×10^{17} atoms/cm². The results have shown that, apart from introducing nitrogen in the structures, a high level of their intermixing is induced. Extracted elemental depth profiles of an as-deposited structure and after implantation to 2×10^{17} atoms/cm², from RBS analysis, are shown in Fig. 9. It is seen that about 30 at% of nitrogen is incorporated in the structures around the projected ion range. Also, Al and Ti layers become heavily intermixed, especially in the mid region of the multilayered structure. The multilayered feature of the structure is preserved, but it consists of compositionally graded ternary (Al,Ti)N layers. Individual layers are either Al or Ti rich, and they are tightly bound because they are formed by intermixing of initially isolated layers. The results of TEM analysis of these structures are shown in Fig. 10. The image of the non-implanted sample (a) clearly shows separated layers, bright contrast corresponding to Al and dark contrast to Ti. The layers exhibit a very fine polycrystalline structure. In the implanted sample (b) we still see a layered polycrystalline structure, but in this case the contrast between the layers is much more equalized, particularly in the mid and outer region. This suggests that the material density, which influences scattering of the analyzing electron beam, becomes more uniform. The applied method can be used for fabrication of different compositionally graded ternary (Al,Ti)N multilayers, by altering the ion irradiation fluence and energy.

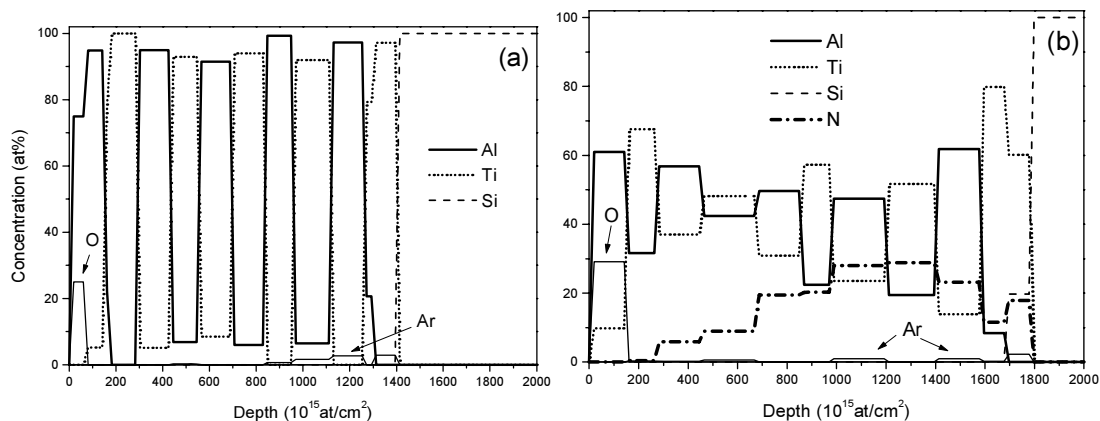


FIG. 9. Extracted depth profiles from Al/Ti multilayers: (a) as-deposited, (b) implanted with nitrogen to 2×10^{17} atoms/cm².

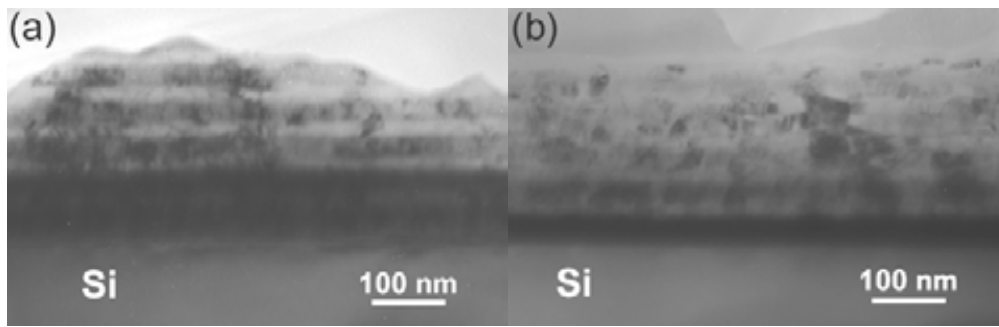


FIG. 10. Cross-sectional TEM images of Al/Ti multilayers: (a) as-deposited, (b) implanted with nitrogen to 2×10^{17} atoms/cm².

4. CONCLUSIONS

Ion irradiation of single component CrN and TiN films induces reordering of the structure, which retains its polycrystalline nature, but consists of larger grains and nano-particles of the same phase. Sheet resistivity measurements can be useful to interpret the compositional and structural changes in the layers as a function of deposition parameters and ion irradiation.

Combined processes of ion pre-implantation and deposition of hard TiN coatings on stainless steel substrates induce an increase of microhardness for more than eight times. Pre-implantation of the substrates induces the formation of Fe-nitride phases. Structure of the deposited TiN coatings shows a strong dependence on ion beam pre-treatment of the substrates.

Multilayered AlN/TiN structures exhibit a much higher stability when exposed to argon ion irradiation compared to the Al/Ti system. In Al/Ti multilayers we observe a progressed intermixing with increasing the ion fluence. Ion irradiation induces an increase in the mean grain size, but the multilayered structure is preserved. In AlN/TiN system no interface mixing is registered for any of the applied irradiation fluences. Different behaviour compared to Al/Ti system is assigned to immiscibility of AlN and TiN.

High fluence nitrogen implantation in Al/Ti multilayers results in highly intermixed structures, consisting of multilayers with different fraction of Al, Ti and N. Although initially isolated Al and Ti layers are fully intermixed, the multilayered structure is preserved. It consists of tightly bound ternary (Al,Ti)N layers with different composition. Ion irradiation induces an increase of the mean grain size, forming larger grains that may stretch over a thickness of a few individual layers.

REFERENCES

- [1] SUNDGREN, J.E., *Structure and properties of TiN coatings*, Thin Solid Films, 128 (1985) 22.
- [2] ZEGHNI, A.E., HASHMI, M.S.J., *The effect of coating and nitriding on the wear behaviour of tool steels*, J. Mater. Process. Tech., 155–156 (2004) 1918.
- [3] HOCK, K., SPIES, H.J., LARICH, B., LEONHARDT, G., *Wear resistance of prenitrided hardcoated steels for tools and machine components*, Surf. Coat. Tech. 88 (1996) 44.
- [4] SPROUL, W. D., *New routes in the preparation of mechanically hard films*, Science 273 (1996) 889.

- [5] HELMERSSON, U., TODOROVA, S., BARNETT, S.A., SUNDGREN, J.-E., MARKERT, L.C., GREENE, J.E., *Growth of single-crystal TiN/VN strained superlattices with extremely high mechanical hardness*, J. Appl. Phys. 62 (1987) 481.
- [6] LI, D., LIN, X.-W., CHENG, S.-C., DRAVID, V.P., CHUNG, Y.-W., WONG, M.-S., SPROUL, W.D., *Structure and hardness studies of CN_x/TiN nanocomposite coatings*, Appl. Phys. Lett. 68 (1996) 1211.
- [7] PALDEY, S., DEEVI, S.C., *Single layer and multilayer wear resistant coatings of (Ti,Al)N: a review*, Mater. Sci. Eng. A 342 (2003) 58.
- [8] WANG, Y.Y., WONG, M.S., CHIA, W.J., RECHNER, J., SPROUL, W.D., *Synthesis and characterization of highly textured polycrystalline AlN/TiN superlattice coatings*, J. Vac. Sci. Tech. A 16 (1998) 3341.
- [9] KIM, D.-G., SEONG, T.-Y., BAIK, Y.-J., *Effects of annealing on the microstructures and mechanical properties of TiN/AlN nano-multilayer films prepared by ion-beam assisted deposition*, Surf. Coat. Tech. 153 (2002) 79.
- [10] CANO, E., MARTINEZ, L., SIMANCAS, J., PEREZ-TRUJILLO, F.J., GOMEZ, C., BASTIDAS, J.M., *Influence of N, Ar and Si ion implantation on the passive layer and corrosion behaviour of AISI 304 and 430 stainless steels*, Surf. Coat. Tech. 200 (2006) 5123.
- [11] SHARKEEV, Y.P., BULL, S.J., PERRY, A.J., KLINGENBERG, M.L., FORTUNA, S.V., MICHLER, M., MANORY, R.R., SHULEPOV, I.A., *On high dose nitrogen implantation of PVD titanium nitride*, Surf. Coat. Tech. 200 (2006) 5915.
- [12] ZIEGLER, J.F., BIRSACK, J.P., LITTMARK, U., *The Stopping and Range of Ions in Solids*, Pergamon, New York (1985).

ION BEAM SYNTHESIS AND MODIFICATION OF SILICON CARBIDE

Yu Liangdeng, Saweat Intarasiri, Teerasak Kamwanna, Somsorn Singkarat

Fast Neutron Research Facility, Chiang Mai University, Chiang Mai, Thailand

Abstract. Silicon carbide (SiC) is a very promising candidate material that is only surpassed by diamond in performance for high-power microelectronic device applications. However, traditional fabrication methods cannot meet requirements of large scale, high purity, good crystalline quality and easy further processing for modern applications. Ion beam synthesis (IBS) of SiC is a new technique to respond to the challenge. High-fluence carbon ions at either single energy of several tens of keV or multiple energies of several hundreds of keV were implanted in silicon wafers at elevated temperatures to fluences of 10^{17} – 10^{18} ions/cm². The single-energy ion implantation was followed by either thermal annealing or swift (high energy) heavy-ion beam annealing for investigating basic effects on synthesis of silicon carbide. The multiple-energy ion implantation was aimed at investigating effects on forming a broadened synthesized Si-C layer. The ion implantation induced C-ion distribution and crystalline structure and quality in the implanted region were characterized and compared for various conditions. With optimized IBS conditions such as the ion fluence and annealing temperature, polycrystalline nano-grained 3C-SiC was obtained in a layer of thickness up to > 1 μm buried in the ion-implanted silicon. Subsequent high-temperature thermal annealing could recrystallize SiC but the required temperature was high, treatment time was long and surface oxide was formed, and it was thus industrially difficult, ineffective and high costly. Using swift heavy ion beams to bombard the C-implanted Si at relatively lower temperatures with extremely low fluences or short time was developed as an alternative for the annealing purpose to recrystallize SiC. The process involves two effects contributing to the recrystallization, energy deposition induced temperature elevation and atomic recoiling motivated atomic mobility. Therefore, swift heavy ion beam annealing (SHIBA) should be more effective on the recrystallization and thus avoiding the use of high temperatures. SHIBA was found to be dominated by the electronic stopping process, namely the higher the energy the better the ion-beam deposited energy.

1. INTRODUCTION

Silicon carbide is a promising candidate material for device applications due to its outstanding properties such as wide band gap, high-temperature stability and high thermal conductivity, radiation hardness and chemical inertness [1][2]. Unfortunately, since it is still difficult to grow SiC material of crystalline quality to meet requirements for a large scale industrial application, small-size and high-cost SiC wafers severely limit their applications at present. Considerable effort has been devoted to developing and improving methods to produce silicon carbide with high purity and good crystalline quality. Among these methods, high-fluence carbon implantation into silicon in combination with subsequent or *in situ* thermal annealing, namely, ion beam synthesis (IBS), has been shown to be able to form polycrystalline or epitaxial cubic SiC (β -SiC) layers in silicon, although details of the layer formation mechanisms are not yet fully understood [3][4]. On the other hand, in the field of Si technology, annealing or crystallization of amorphous Si layers on the crystal-Si substrates by ion-beam irradiation is well known as the ion-beam induced epitaxial crystallization (IBIEC). Over the past two decades there have been a number of experimental and theoretical studies on IBIEC [5]–[18]. Of particular interest are the low temperature characteristics of this method. Amorphous Si layers on the crystal-Si substrates are epitaxially crystallized in a layer-by-layer fashion by IBIEC at temperatures as low as 150°C, far below the temperature of 600°C needed for ordinary solid-phase epitaxial growth during furnace annealing. The rate of IBIEC has also been shown to be increased by the inelastic electronic scattering that occurs when the amorphous Si layer is exposed to a MeV heavy ion beam [14–16]. Ion-beam

irradiation cannot only recrystallize amorphous Si layers, but also anneal defects or crystallize amorphous clusters, if the substrate is kept at a certain high temperature during irradiation. Based on these principles, it is possible that IBIEC will improve the crystallinity of buried β -SiC layers synthesized by IBS in comparison with conventional high temperature annealing.

Of all the existing polymorphs of SiC, β -SiC (3C polytype) is of very great technological interest [16]. It has been shown that IBS has the capability of fabricating polycrystalline or epitaxial β -SiC layers at relatively low temperatures and with low levels of contamination. More than three decades have passed since the publication of the pioneering articles [20][21] on IBS, but the interest of investigators in this problem is still great [22–24]. This is associated with the increasing role that silicon carbide plays in electronic technology. IBS usually consists of high fluence ion beam implantation and subsequent high temperature annealing to remove the defects and recrystallize the sample. In accordance with the previous studies, the key factor that determines the crystalline quality of the β -SiC layer by IBS is the annealing procedure [25]. However, it has been reported also that other conditions like the implantation temperature [22] and the implanted carbon fluence [23] might have some influence on the growth of the buried silicon carbide layer.

The temperature to crystallize the implanted Si-C layer and transform the disordered Si-C bonds into the ordered β -SiC structure [20][24] is of considerable interest [24–27]. The Si-C mixture, after implantation of large fluences of carbon, is assumed to be amorphous [26][27][32]. Carbon atom diffusion in the implanted layer is restricted by the strong Si-C bonds [26][28]. The lowest reported temperature for the start of crystalline SiC formation is 300°C [29]. Other researchers report values of 400°C [26], 500°C [35], 600°C [36], 700°C [37], 800°C [38], 850°C [20] and 900°C [24]. However, some authors demonstrate that much higher annealing temperatures, e.g. 1000°C [39], 1250°C [23] and 1405°C [40] are demanded to achieve crystalline silicon carbide layer in silicon.

Based on the silicon technology developed during past 30 years, besides annealing methods using heating of the material to activate the recrystallization process, a distinct annealing method is ion beam irradiation of the amorphous material. During ion beam irradiation of a-Si clusters embedded in a crystalline substrate at temperatures $>100^\circ\text{C}$, two annealing processes contribute to the recrystallization of the clusters [41]. One of them is the thermal recrystallization process of the isolated amorphous clusters [42], which can be excited either by an external heat source or by the deposited beam power. The other annealing process is ion beam induced epitaxial crystallization (IBIEC) produced by the elastic nuclear energy transferred to the atoms in the collision cascades [43]. High-energy ion bombardment of amorphous semiconductor layers may promote crystallization at the interface separating the amorphous and crystalline substrate phases (a/c interface). The crystallization proceeds then in a layer by-layer manner with migration of the a/c interface towards the surface [43]. Ion implantation into the substrate at large depths hardly changes the film chemistry but facilitates atomic site exchanges and defect migration owing to collision-induced atomic displacements within the amorphous zone. The activation energy for ion beam annealing is 1/5 to 1/10 of the value for thermal annealing [44]. Such very low activation energies, typically below 0.4 eV, control the crystallization process and are most likely related to the mobility of vacancy clusters. Thus, the IBIEC method permits crystallization of amorphous silicon at the low temperature of 150°C, which is well below the typical temperature for thermally-induced solid-phase epitaxy of about 550°C. However, the kinetics of IBIEC is very complex and depends on the nuclear energy deposition, ion fluence, flux and temperature [45].

Furthermore, investigation of the physical nature of the mechanism of silicon carbide formation that depends on the synthesis conditions is of significant theoretical and practical interest. As reported in the majority of papers, synthesis is accomplished by implantation of carbon ions of some specified energy and fluence into a silicon substrate. Under such implantation regimes, the profile of the implanted ion concentration has a Gaussian form, and thus it could be possible for, in a number of cases, occurrence of unwanted effects caused by variations of the concentration distribution with depth [25]. Carbon atoms are distributed in the whole implanted range, but only in a limited region is the concentration of carbon comparable to that of silicon to favour the formation of Si-C. As the depth profile of carbon fluence does not change much even after high-temperature annealing, β -SiC is normally formed within this layer [46].

Several papers have reported to use ion-implanted layers with uniform carbon concentrations to construct a rectangular profile of C atom distribution in silicon. Recently, a multi-energy ion implantation approach has been proposed to produce thick silicon carbide layer in silicon and modify its composition profile [36]. By selecting carefully the implantation energy and fluence of carbon ions, a rectangular carbon concentration profile can be achieved for the buried β -SiC layer using this approach [36]. Attempts to construct such profiles were also reported in refs. [22,23,29,36]. Srikanth et al. [25] applied multiple implantation of C ions into Si with energies 20, 30, 50 and 70 keV in order to overcome the deleterious effects of inhomogeneities occurring due to the Gaussian form of the implanted profile. It is appropriate to provide an homogeneous C concentration of $2 \times 10^{22} \text{ cm}^{-3}$ over the depth range 50–250 nm (with respect to the silicon surface) [36].

Operating IBS at temperatures well above room temperature by *in-situ* annealing helps to reduce implantation-induced damage [47]. Upon *in situ* thermal annealing, Edelman et al. first recognized the usefulness of implantation at high temperature (up to 850°C) [22]. Kimura et al. [28] pointed out that implantation at an elevated temperature led to a reduction in the post-implantation annealing temperature required for the synthesis of crystallized SiC. For example, an implantation at 600°C was shown to be equivalent to an annealing temperature of 1100°C following a room-temperature implantation. The effects of the implantation temperature in the range 525–720°C upon the β -SiC formation were also studied by Reeson et al [23]. Their results show that if the implantation temperature is sufficiently high (>625°C), a layer containing epitaxial β -SiC crystallinities in topotactic relationship with the silicon matrix grows during implantation using the silicon substrate as a seed.

This work consisted of two stages. The first stage was focused on conventional single-energy C-ion implantation in Si followed by thermal annealing to build up an investigation base for the next stage of the research project. It was aimed at searching for optimal conditions of C-ion implantation in Si to result in formation of polycrystalline or epitaxial Si-C and temperatures elevated during C-ion implantation for optimizing crystallization of Si-C, and determining phases and concentration distribution or depth profile of primarily implanted carbon layers in Si substrate. The work in the second stage was extended to swift heavy ion beam annealing (SHIBA) and multiple-energy C-ion implantation. It was aimed at investigating effects of SHIBA on crystallization of SiC, optimization of SHIBA parameters such as ion species, energy and fluence for crystallization of Si-C, and C-ion energy and fluence in multiple-energy ion implantation to form an applicable broad near-rectangular-shape implanted carbon layer.

2. EXPERIMENTS

2.1. Carbon Ion Implantation

2.1.1. Single energy

Samples were two-inch p-type silicon wafers with the resistivity of $\sim 30 \text{ } \Omega\text{-cm}$ and a (100) surface. C-ion implantation was carried out in two sets of conditions. The ion beam conditions of the first set (marked as RT) were: energy of 80 keV, fluence of $2.7 \times 10^{17} \text{ ions/cm}^2$, and beam current density of $2\text{--}5 \text{ } \mu\text{A/cm}^2$ at room temperature, using the Varian ion implanter at Chiang Mai University. The conditions of the second set (marked as HT) were: energy of 40 keV, fluence of $6.5 \times 10^{17} \text{ ions/cm}^2$, beam current density of $2\text{--}5 \text{ } \mu\text{A/cm}^2$, and temperature of 400°C , using the Danfysik ion implanter at Uppsala University. For avoiding channelling effect during ion implantation, the Si samples were oriented at 7° from normal. The pressure in the target chamber during ion implantation was in an order of 10^{-4} Pa . After ion implantation, the Si wafers were cut into pieces with a size of $1 \times 1 \text{ cm}^2$, and some were annealed in a vacuum furnace at temperatures of 800, 900 and 1000°C for 60 minutes, respectively, and some remained as control.

2.1.2. Multiple energy

Samples were two-inch p-type silicon wafers with the resistivity of $\sim 30 \text{ } \Omega\text{-cm}$ and a (100) surface. Two sequences of the ion energy were used in C-ion implantation, namely, an energy-decreasing sequence of 600, 500, 400, 300 keV and an energy-increasing sequence of 300, 400, 500, 600 keV. The ion fluence for each energy was the same, namely $3.2 \times 10^{17} \text{ ions/cm}^2$. The beam current was about $1 \text{ } \mu\text{A}$ and the beam spot was 5 mm in diameter. The ion beam was incident at a random direction with a sample tilting angle of 7° from normal. The samples were at room temperature during ion implantation and the pressure of the sample chamber was 10^{-4} Pa . The ion implantation was undertaken using the 1.7-MV tandem accelerator at Chiang Mai University.

2.2. Analysis and Characterization

2.2.1. C-ion concentration distribution

Two techniques were used to determine the implanted C-ion concentration distribution in silicon, namely Rutherford Backscattering Spectrometry (RBS) and Elastic Recoil Detection Analysis (ERDA). RBS analysis was carried out using the 1.7-MV tandem accelerator at Chiang Mai University. The analyzing ion species was He^{++} , ion energy was 2.13 MeV, and beam current was about 20 nA. The backscattered ions were detected at a scattering angle of 160° by a Si surface barrier detector. The system resolution was 24 keV FWHM, corresponding to a depth resolution of some 60 nm in Si. Computer programs such as SRIM [48], SIIMPL [49] and a self-developed software were used for assisting the analysis of the concentration distributions.

The self-developed program is a direct measurement of a light-element concentration depth profile in a heavy matrix from the RBS spectra themselves without using theoretical calculation for fitting applied by some software such as DataFurnace [50]. The essentials are presented below. In principle, the total yield at channel i , Y_i is a sum of two terms

$$Y_i = C_i^C Y_i^C + C_i^{Si} Y_i^{Si} \quad (1)$$

where Y_i^C and Y_i^{Si} are the RBS yields at channel i from the pure carbon and silicon samples, respectively, and C_i^C and C_i^{Si} are atomic percentage concentrations of carbon and silicon, respectively, namely $C_i^C = N^C(x_i^C)/N(x_i^C)$ and $C_i^{Si} = N^{Si}(x_i^{Si})/N(x_i^{Si})$. Here $N^C(x_i^C)$ and $N^{Si}(x_i^{Si})$ are the number densities of C and Si atoms at scattering depth x_i^C for C and x_i^{Si} for Si, respectively, and C atoms at x_i^C and Si atoms x_i^{Si} together contribute backscattering yields at channel number i , while $N(x_i^C)$ and $N(x_i^{Si})$ are the total number densities at depths x_i^C and x_i^{Si} , respectively. In the region near the Si edge of the RBS spectrum, there is actually no contribution from the He^{++} -C interaction since the kinematic factors of C and Si in our case are 0.26 and 0.57 respectively. This leads to a far separation between the spectrum edge parts of C and Si. Therefore, for this region formula (1) is reduced to

$$Y_i = C_i^{Si} Y_i^{Si} \quad (2)$$

The carbon atomic percentage concentration, C^C , at depth x_i^{Si} is then calculated by the principle

$$C^C + C^{Si} = 1 \quad (3)$$

The conversion from the channel number (now, only for the Si part of the spectrum) to the corresponding depth followed the standard method but taking into account for changed Si and C concentrations by the implantation and a depth-dependent stopping cross section for the analyzing ion due to the existence of C ions in the path of the analyzing ion. The C-ion depth profiles measured by this way were finally deconvoluted by the depth resolution as mentioned above for real profiles by assuming Gaussian distributions of the C ions. The applicability of the program has been discussed elsewhere [51].

The ERDA analysis was carried out using a 29 MeV $^{127}\text{I}^{7+}$ from the 5-MV Pelletron accelerator at the National Tandem Accelerator Facility in Uppsala, Sweden [52]. The data acquisition and analysis system was FAST ComTec GmbH [53], which analyzed the time of flight and the energy signals for each recoil. The conversion from energy spectrum to depth profile was done using Program CONTES [54].

2.2.2. Characterization

A range of techniques were applied for characterization of the implanted layer. Infrared spectroscopy (IR) using a Perkin Elmer FT-Infrared spectrometer with the range of 400–1.500 cm^{-1} and a resolution of 4 cm^{-1} detected Si-C bonds. Raman scattering analysis using a Renishaw 2000 system of a Micro-Raman spectrometer with a spectral resolution of 1–2 cm^{-1} , employing the exciting source of a 514.5-nm radiation coming from an Ar-ion laser with a power of about 25 mW and a power density below 10^2 W/cm^2 (macro configuration), characterized the crystalline degree. RBS/channeling analysis using the tandem accelerator at FNRF with the same beam conditions for RBS analysis studied recrystallization of the implanted crystal. Glancing incidence X ray diffraction (GIXRD) using a Bruker D8 Advance system which employed a copper target X ray tube (CuK_α line, wavelength = 0.1542 nm) with a tungsten filament at 40 kV and the incident angle between the X ray and the sample surface

set to 1° (corresponding to the x ray depth of about 1000 nm in pure silicon) was performed at room temperature for phase identification. Transmission electron microscopy (TEM) was applied to observe the structure. The cross-sectional TEM specimens were prepared by gluing the two samples together face to face to form a sandwich structure. The sandwich was ground to a rod with a diameter of 2.3 mm and then inserted into a Cu tube, which was sliced. Each cross-sectional slices was then ground from both sides to 0.1 mm thickness followed by dimple grinding down to $\sim 10 \mu\text{m}$ at its centre and finally ion milling was applied to thin the samples down to electron transparency. The TEM investigation was carried out in a field emission gun FEI Tecnai F30 ST operated at 300 kV with a point resolution of 2.05 Å. The instrument was equipped with a Gatan Imaging Filter and energy dispersive spectroscopy system.

2.3. *Swift Heavy Ion Beam Annealing (SHIBA) of C-ion Implanted Si*

In the experiment, the samples were 40 keV C-ion implanted Si wafers to the fluence of 6.5×10^{17} ions/cm² at the elevated temperature of 400°C. Two neighbored heavy ion species, iodine and xenon, were used for the swift heavy ion beam annealing (SHIBA) experiment. Multiply charged iodine ions, accelerated by the 5-MV tandem accelerator at the National Tandem Accelerator Facility in Uppsala, Sweden to energies of 10, 20, 30 MeV, respectively, bombarded the samples to fluences of 1, 2, 5×10^{12} ions/cm², respectively, with a fluence rate of 1×10^{10} ions/cm²/s at temperatures of 90, 400, 800°C, respectively. Doubly charged xenon ions, accelerated by the 2-MV Van de Graff ion accelerator at the Ion Beam Center, Surrey, UK to the energy of 4 MeV bombarded the samples to fluences of 5×10^{13} ions/cm² and 1×10^{14} ions/cm², respectively, at the temperature of 500°C.

3. RESULTS AND DISCUSSION

3.1. *Depth Profiles of Single-energy Implanted Carbon in Si*

Because a broad stoichiometric C profile is required for SiC synthesis, C concentration depth profiles must be analyzed. We analyzed C depth profiles of mono-energy C-ion implantation at room temperature (RT) and elevated temperatures (HT) for as-implanted, thermally annealed and ion-beam annealed samples. Figures 1–4 show the analytical results of the C depth profiles. It is seen that the variously measured and predicted depth profiles are in quiet good agreement. Some features of the RT and HT depth profiles can be seen from the figures. The maximum concentration depends on the ion fluence applied.

For fluences as high as 2.7×10^{17} ions/cm² and 6.5×10^{17} ions/cm², the maximum concentrations in percentage of about 20% and 40–50% respectively are reasonable. The corresponding depths at the maximum concentrations as well as the ranges are determined by the energy of the implanted ions. All of these features of the measured profiles are very close to those of theoretical profiles except the fluence, for which the RBS-profiles show lower values, whereas the ERDA-profiles show higher values. For the RBS-profiles, the reason is due to insensitivity of the self-developed method to lower fluences, and for the ERDA-profiles, the higher fluence values are due to the inclusion of the contaminated hydrocarbon. It is interesting to notice that high temperature thermal annealing does not broaden the C depth profile. Some published data for carbon diffusion in silicon show high diffusion coefficients in normal situation [55]. This can be only explained by the implanted carbon already bonded with silicon. We preliminarily conclude from the depth profile analysis [51] that:

- A fluence higher than about 6×10^{17} ions/cm² is necessary for a stoichiometric implantation;

- Either elevated-temperature ion implantation or post-implantation thermal annealing does not much broaden the C depth profile;
- High-fluence implanted C does almost not diffuse in Si, instead may already be combined with Si;
- Our self-developed RBS method works for analysis of light elements in heavy matrix.

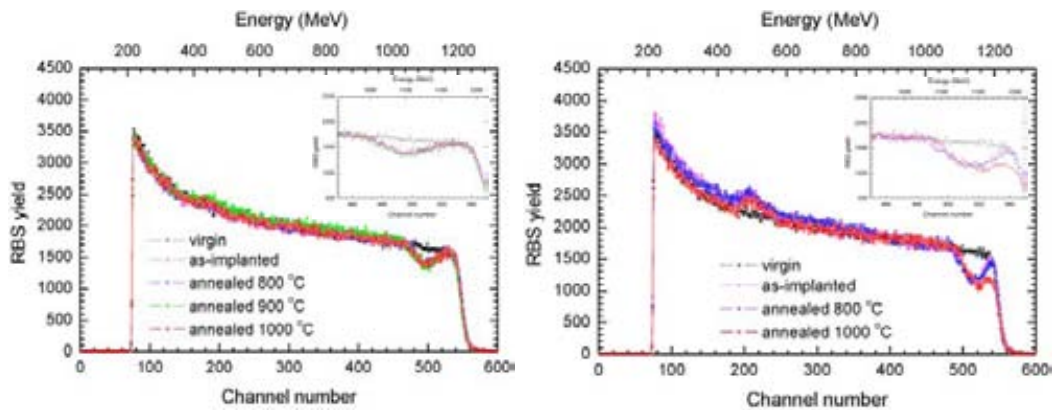


FIG. 1. RBS random spectra. (left) RT, and (right) HT. The dip of the spectrum part (or the deficient part) near the front edge from the C-ion implanted sample, as shown in the insets, allows the self-developed method to calculate the C ion concentration distribution in Si (see further in Figure 3).

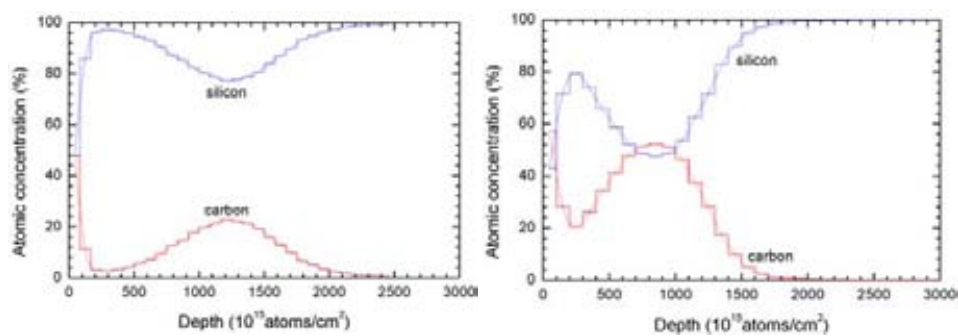


FIG. 2. Atomic concentrations of as-implanted samples measured by ERDA. (left) RT and (right) HT. It shows a high fluence necessary for stoichiometric implantation.

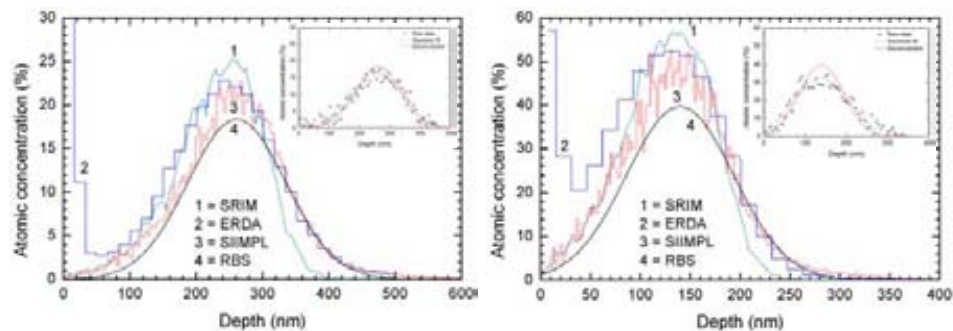


FIG. 3. Summary of the depth profiles of as-implanted C ions in Si obtained by RBS, ERDA, SRIM2003 and SIIMPL. (left) RT and (right) HT. The insets show the RBS-analyzed raw depth profiles and the deconvoluted profiles. It shows that our RBS method reasonably works. The ERDA profiles show the presence of a top layer of carbon on the sample, probably due to surface contamination that could be detected by the sensitive technique.

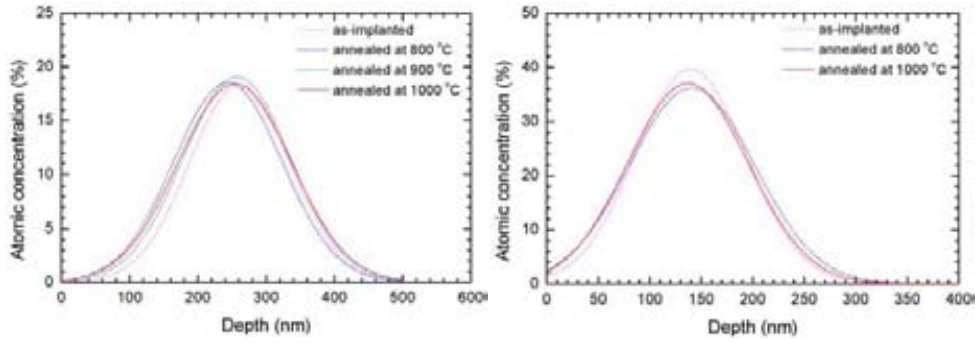


FIG. 4. Depth distributions of the atomic concentration of C ions implanted in Si at various annealing conditions measured by our RBS method. (left) RT and (right) HT. The results show little broadening of the profiles or C diffusion. Note that the diffusion coefficient of carbon in silicon $D_{C-Si} \approx 0.4 \text{ cm}^2/\text{s}$ at about 1000 K [55], which is pretty high

3.2. Characteristics

We mainly focus on the characteristics of recrystallization and the SiC polytype. The results [56] are shown in Figures 5–10. Figure 5 shows the RBS/channelling spectra in the random and aligned directions for the unimplanted and implanted samples. The channelling spectra of the samples were taken in the $\langle 100 \rangle$ direction of the crystals. The formation of a buried layer of mixed Si-C is readily apparent from a dip close to the front edge in all of the implanted spectra. There are two effects in competition to contribute to the features of the aligned spectra. On one hand, the presence of C, which makes the spectrum deficient, and on the other hand, ion-implantation-induced radiation damage to the Si lattice resulting in an increase in the yield. Similar to the random spectra, a deficiency is seen in the Si-signal, between channels 490 to 510 for RT-implanted samples, but between channels 510 to 530 for HT-implanted samples. On either side of this region, the Si-backscattering yield is higher. The implanted and annealed sample can be considered as a sandwich-like structure, i.e. the regrown front silicon layer, the buried β -SiC and the bulk silicon substrate. In the RT-implantation case, for the as-implanted spectra, the coincidence of the dip in the channelling spectra indicates a highly damage or amorphized near-surface silicon layer. The maximum of the aligned yields near the surface around channel 540 are higher than in the deeper regions. This corresponds to the maximum of the radiation damage distribution which lies closer to the surface than the maximum of the carbon distribution. The spectra of the annealed samples look similar to the spectrum of the as-implanted sample, and the yield close to the surface are almost equal to the yield of the random spectrum. Hence, these samples implanted at room temperature are still amorphous in the Si surface layer. The yield maximum in the deeper region decrease as the annealing temperature is increased, indicating a recrystallization in this region. The situation for the HT-implanted samples is somewhat different from that of the RT-implanted samples. It is clearly seen that the dip is deeper and closer to the edge, which agree well with the ERDA results. The aligned yield of the HT samples is about half that of the random yield, and is lower than that of the RT samples, indicating a less damaged lattice resulting from the *in-situ* annealing. Compared with the RT spectra, which show almost no difference among the annealed spectra at the near front edge region, the HT spectra exhibit at this region a decrease in the yield for increasing annealing temperature. This decrease also occurs in the region below the C-ion implanted region, particularly when the annealing temperature is as high as 1000°C. Since diffusion of carbon has been ruled out as analyzed above, these facts indicate that the elevated-temperature ion implantation clearly improves the post-implantation annealing for recrystallization of the Si substrate and thus raises the quality of the synthesized crystal.

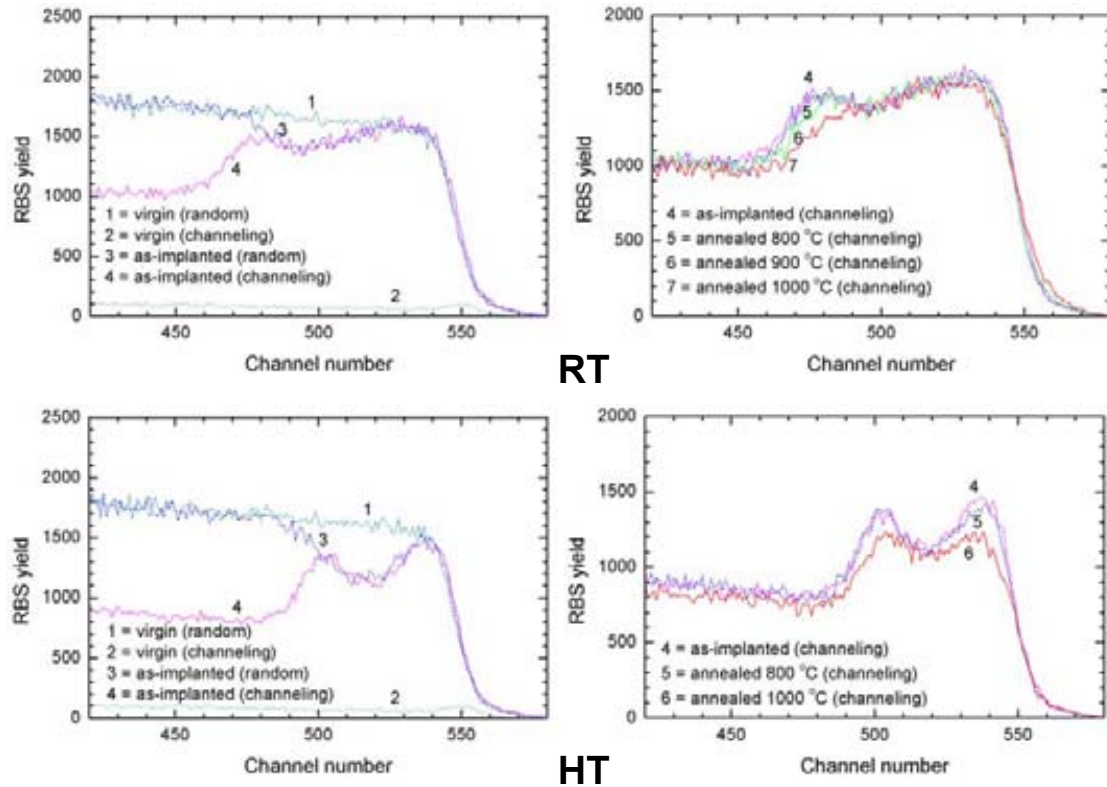


FIG. 5. RBS/channelling spectra. Left figures for each case: comparison between the as-implanted and virgin spectra. Right figures for each case: comparison between the annealed and as-implanted spectra. It is seen that the as-implanted layer is amorphous, whereas the post-implantation annealed layers are recrystallized. It is also seen that the HT (higher fluence) produces better recrystallization than RT because at HT the as-implanted aligned spectra are lower and annealed aligned spectra are improved more than that at RT. Because of very different lattice constants for SiC (3.08 \AA for Si-Si, and 1.89 \AA for Si-C) and Si (5.43 \AA), it is not expected to have good aligned RBS/channelling spectra in this case.

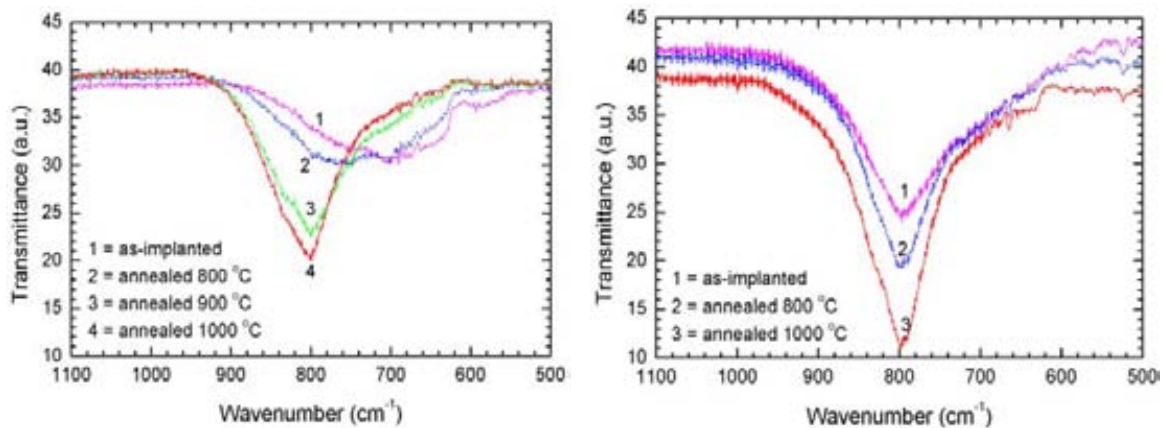


FIG. 6. IR transmittance spectra from cases (left) RT and (right) HT. For RT, as-implanted peak centred at 700 cm^{-1} shows amorphous SiC network. β -SiC has a transverse optical phonon absorption band centred at 796.2 cm^{-1} . HT and annealed spectra show formation and growth of β -SiC.

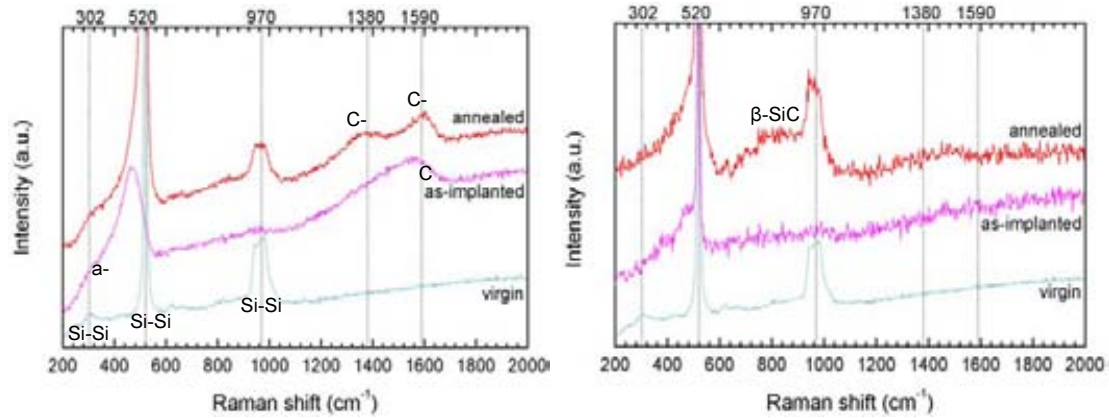


FIG. 7. Raman spectra, annealed at 1000°C. (left) RT and (right) HT. For RT, amorphous phase presents in as-implanted sample and decreased amorphous phase in annealed sample. For HT, amorphous phase is lower in as-implanted sample and β -SiC presents in annealed sample.

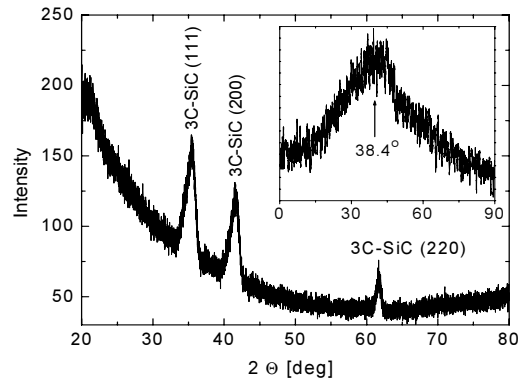


FIG. 8. XRD spectrum of the HT 1100°C-annealed sample, measured at 38.4° from the (001) direction of the substrate. The inset shows the 3C-SiC (111) peak intensity as a function of the θ - 2θ plane angle with respect to the substrate (001) orientation (for the 90° case the plane is parallel to the wafer surface).

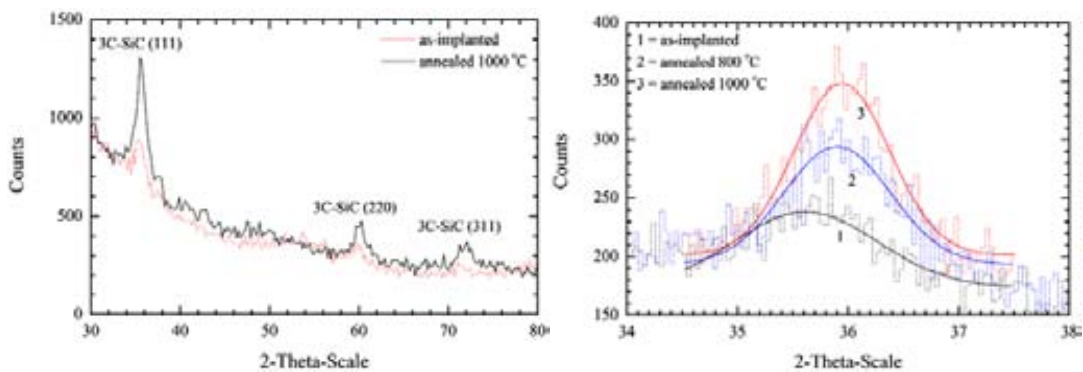


FIG. 9. Glancing incident X ray diffraction (GIXRD) spectra of the 40 keV C-ion implanted Si to a fluence of 6.5×10^{17} ions/cm² at 1°. (left) A large 2θ -range of the spectra of the samples as-implanted and annealed at 1000°C. (right) Comparison of the GIXRD 3C-SiC (111) diffraction peaks obtained from the samples as-implanted, and annealed at 800 and 1000°C.

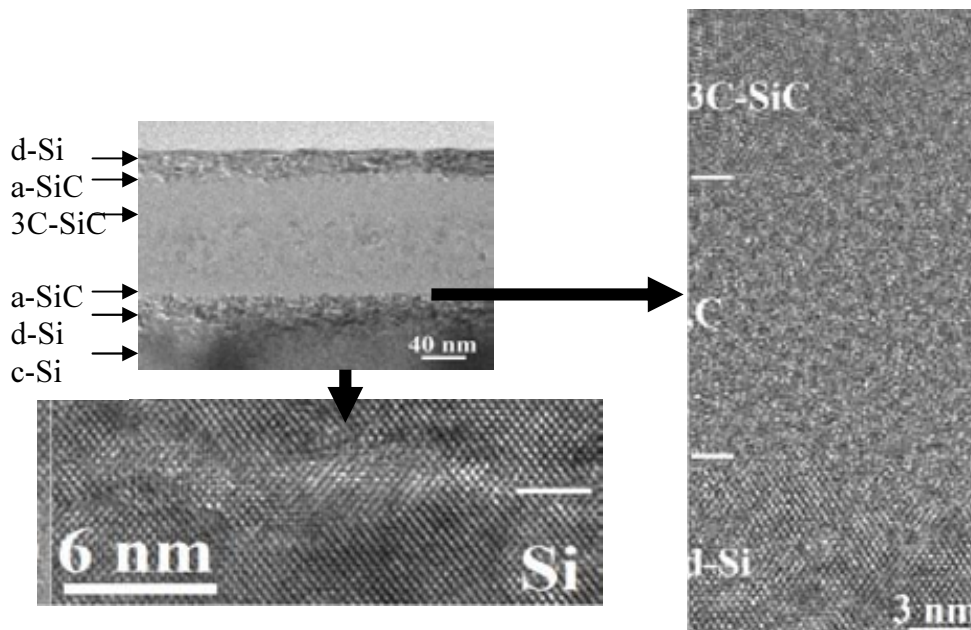


FIG. 10. Cross sectional TEM images of the ion-implanted layer for HT as-implanted sample, showing five sub-layers in the implanted region: *d(amaged)*-Si, *a(morphous)*-SiC, 3C-SiC, *a(morphous)*-SiC, and *d(amaged)*-Si, beneath which is the *c(rystalline)*-Si substrate, as shown by the small arrows. Two special zones are zoomed to show the *a*-SiC sub-layer that is between 3C-SiC and *d*-Si sub-layers and the *c*-Si substrate that is not affected by ion implantation.

Typical IR spectra from our experiments are shown in Figure 6, where the background recorded from the untreated silicon wafers was already subtracted. For the as-implanted RT sample, the spectrum shows a broad band, roughly Gaussian in shape, centred at a wave number of about 700 cm^{-1} . This is related to the presence of an amorphous SiC network in the implanted layer [57, 58]. After annealing, a Lorentzian contribution appears in addition to the Gaussian band. This feature becomes sharper and shifts slightly toward higher wave numbers, approaching the values reported for crystalline SiC. β -SiC typically exhibits a transverse optical phonon absorption band centred at 796.2 cm^{-1} [59, 60]. It is also noticed that after annealing at 800°C , the spectrum shows a broader FWHM than that of the as-implanted one. This indicates the start of the transformation from amorphous to crystalline phase while a certain quantity of the amorphous phase still remains in the system. However, when the annealing temperature is as high as 900°C , the spectral shape becomes fully Lorentzian, indicating that most of the amorphous phase has been transformed to the crystalline phase. For continued annealing, the peak grows in height and narrows in width, indicating a further growth of the SiC layer. For the as-implanted sample of HT case, the spectrum is rather similar to those of the annealed RT-implanted samples. Only the Lorentzian signal from crystalline SiC appears and no Gaussian signal from *a*-SiC is seen. The SiC peak is at a wave number of 797 cm^{-1} with an FWHM of 138 cm^{-1} . This result indicates the crystalline β -SiC has already formed after implantation at 400°C without post-implantation annealing. At further annealing, the peak only grows in height and narrows in width, without shifting in position, with increasing annealing temperature. This indicates the further growth of the SiC layer, similar to the annealed RT-implanted samples.

Figure 7 exhibits Raman spectra from the virgin silicon, as-implanted, and 1000°C annealed samples for both RT and HT cases. For the virgin silicon sample, the spectrum shows the presence of first and second order transverse acoustical phonon (2TA) peaks from the crystalline Si substrate at 520 and 302 cm^{-1} , respectively. A clear peak due to the Si second-order features appearing at 970 cm^{-1} is also present in the virgin sample. For the RT-implantation case, the first bands in the 200–600 cm^{-1} region are modified in relation to highly damaged by the presence of carbon atoms as observed by the peak at $\sim 1550 \text{ cm}^{-1}$ [61]. This gives further evidence of the formation of an amorphous SiC phase by the high dose carbon implantation. After annealing, there is a decrease in the intensity of the amorphous bands due to the recrystallization of the Si region below the implanted layer. However, Raman spectra still show amorphous bands in the annealed sample which indicates the presence of residual amorphous material in the layers. Moreover, the spectrum shows a double band centred at 1380 and 1590 cm^{-1} . This is very similar to the spectra reported for amorphous graphitic carbon [61, 62]. In the HT as-implanted sample, we compare the band of Si-Si bond at 520 cm^{-1} , and observe a lower level of amorphous phase in comparison to the RT-implantation case. The C-C bonds can hardly be observed in the as-implanted sample. After annealing at 1000°C, the spectrum shows “bumps” at 600–800 cm^{-1} , centred at the TO mode of β -SiC at $\sim 796 \text{ cm}^{-1}$ [59]. The LO mode of β -SiC at 969 cm^{-1} is impossible to identify due to the superimposed Si-second-order Raman background. A comparison between the Raman spectra of the samples, showing the amorphous bands related to Si-Si bonds and small bumps of C-C bonds, and the IR spectra from the same samples, showing only a Lorentzian peak related to Si-C bonds in a crystalline network, indicates that the residual amorphous material is mainly formed by homopolar bonds while heteropolar Si-C bonds should almost all be in the crystalline phase.

Figure 8 shows the XRD spectrum of C-ion implanted Si after thermal annealing. Three peaks are observed at $2\theta = 35.5, 41.7$ and 61.6 degrees corresponding to 3C-SiC (111), (200) and (220), respectively [63]. The measurements were done with the θ - 2θ -plane positioned at an angle of 38.4° from the (100) direction of the substrate. For this angle, there is a maximum in the reflected intensity from the 3C-SiC(111), as shown in the inset of the figure. If 3C-SiC is grown on the Si(100) surface, one would expect that the SiC is oriented at 45° from the surface, which is not too far away from the broad maximum centred at 38.4° . According to the literature, the concentration of the (200) peak should be about 20% in relation to the (111). Here we see a relative yield of about 80%, which would indicate a preferential orientation of the (200) facets at 38.4° . From the XRD peaks, the grain size is estimated to be about 8.4 nm according to Scherrer formula [64].

Figure 9 shows typical GIXRD spectra at 1° glancing angle for the as- C^+ -implanted Si and the subsequent thermal annealed samples at 1000°C. The 3C-SiC polytype is observed as peaks at $2\theta = 35.5^\circ, 60.3^\circ$ and 71.9° are for 3C-SiC (111), (220) and (311), respectively [63] on both spectra. The peaks are depth dependent and would disappear at the glancing angles higher than 4° . Therefore, the observed peaks are from the ion-implanted layer. It is noticed that, for the as-implanted sample, the peaks are very weak and broad, due to the poor crystalline quality, while for the post-implantation annealed sample, the peaks are sharper. This fact confirms our previous results of the infrared measurements that the annealing procedure increases the SiC crystallinity, in which a strong decrease of the full width at half maximum (FWHM) of the Si-C absorption peak, centred at 798 cm^{-1} is seen [56]. For understanding of the mechanism of 3C-SiC formation, we further investigated the characteristics of the 3C-SiC (111) peak at $\sim 35.5^\circ$. We deconvoluted those peaks by using Gaussian fit as shown in Figure 9(b). As seen in the figure, as the temperature increases, the FWHM reduces and the peak height increases almost linearly with the temperature, while the peak position remains

constant. The grain size of the polycrystalline SiC was estimated using Scherrer formula [64] to be ~6.4 nm for as-implanted sample and 8.6 and 9.6 nm for annealed at 800 and 1000°C, respectively.

From the results of the GIXRD measurement and the IR measurement, the mean grain size is seen proportional to the inverse of the peak FWHM. For comparison, $\ln(1/\text{FWHM})$ as a function of $10^4/T$ (K) from both our GIXRD and previous IR measurements was studied. We found similar behaviour that the logarithm value of $1/\text{FWHM}$ is slowly decreasing as the reciprocal of the annealing temperature increases. This indicates that the process is governed by the temperature, and the growth of SiC increases with temperature. It is supposed that the SiC grain growth follows an Arrhenius relation with temperature, in which $1/\text{FWHM}$ is proportional to $\exp(-E_a/kT)$, where E_a is the activation energy, k is the Boltzmann constant, and T is the annealing temperature in Kelvin. We have noticed that both IR and GIXRD measurements obtain similar slopes between $\ln(1/\text{FWHM})$ and $1/T$. Thus, the slope from the plot shows an apparent activation energy of ~0.05 eV [65]. Namely, the Si-C bonds can be promptly formed in this case. To our knowledge, there has been no published data found yet on the value of such a transformation reaction in C-ion implanted Si-substrate at high temperature. The value for nucleation and growth of SiC clusters in amorphous matrix under a thermal activation reaction was, however, reported to be ~5.1 eV [66, 67]. The transition is a first-order process and this high value explains the stability of amorphous phase at room temperature.

Figure 10 demonstrates a layered structure of the as-implanted sample by low magnification cross-sectional TEM imaging [68]. Six layers are seen, namely, defective Si (d-Si), amorphous SiC (a-SiC), SiC, a-SiC, d-Si, and crystalline Si (c-Si). The top d-Si layer is believed resulting from the ion bombardment. A similar structure was found in the fifth layer at a depth of about 155 nm and this bottom d-Si layer has almost the same thickness as the top d-Si layer. There is a thicker low contrast layer between the two d-Si layers. A high resolution image, shown in Figure 11 [68], clearly demonstrates 3C-SiC phase in the centre area of this middle layer. Between the 3C-SiC layer and d-Si layers, there are two amorphous layers. Both energy dispersive X ray spectrometry (EDS) and electron energy loss spectroscopy (EELS) results reveal that those amorphous layers consist of silicon and carbon. It is seen that the top amorphous layer is about 35 nm thick while the second amorphous (Si,C) layer near the bottom is only about 15 nm. The average size of the 3C-SiC grains is between 5 and 10 nm. The average grain size obtained by TEM agrees well with the measurements by XRD. At the implantation temperatures and the fluence rate used here, amorphous phases are not expected in pure silicon due to ion beam induced re-crystallization of amorphous regions (a-Si) which are in contact with crystalline silicon (c-Si). Thus, the silicon-rich regions on both sides of the carbon peak, where the carbon concentration is less than the critical number, are not amorphized. These regions are observed as d-Si at the top and bottom layer next to the amorphous zone. This is a clear further indication of the chemical contribution of the implanted carbon atoms to the formation of an amorphous layer, a mechanism that has been explained in Ref. [69] and termed “carbon induced amorphization”. The term reflects the fact that the nuclear collisions induced by the impinging light C-ions cannot alone account for the formation of amorphous material at these elevated implantation temperatures in pure Si, and that therefore the presence of high carbon concentrations must have a strong impact on amorphization. By comparing the ERDA and the TEM results, one should observe that the amorphous layer extends over a depth interval where a fixed carbon concentration of about 17% C is exceeded. As previously known [70], the solid solubility of carbon in c-Si close to the Si melting point is in the range of 10^{17} C/cm³ and almost vanishes at room temperature. Carbon therefore tends to form precipitates. In c-Si it is usually SiC precipitates with cubic 3C

crystal structure. In this experiment, the beam induced nucleation of 3C-SiC precipitates occurs in a sharply limited depth interval within the continuous a-SiC layer. This formation occurs during implantation. The poly-crystalline 3C-SiC inclusions embedded in the continuous amorphous layer centred about the carbon concentration peak where the amounts of C and Si are about the same, are clearly visible in the TEM data. The cross-sectional TEM image shown in Figure 11 reveals that the annealed sample exhibits a similar layered structure as the as-implanted sample. However, the high resolution images clearly show that the middle region between the two d-Si layers consists of crystalline 3C-SiC. The corresponding SAED pattern (Figure 11) showing the three strong spotty rings in accordance with cubic SiC [(111), (220) and (311)] points out that the SiC is polycrystalline. No amorphous (Si,C) layer was found in the annealed sample. The average grain size of the SiC phase is about 8 nm in consistence with the XRD results. It should be pointed out that the SiC layer of the annealed sample is thinner than the thickness of middle layer of the as-implanted sample, whereas the d-Si layers are a little thicker in the annealed sample compared to the corresponding layers in the as implanted sample. One possibility is that the amorphous (Si,C) layer is silicon rich and during the annealing process at 1100°C, the amorphous material is transferred into crystalline Si containing carbon impurities. In the central part of the middle region, containing a stoichiometric mixture of Si and C as seen in Figure 2, the material forms 3C-SiC crystallites.

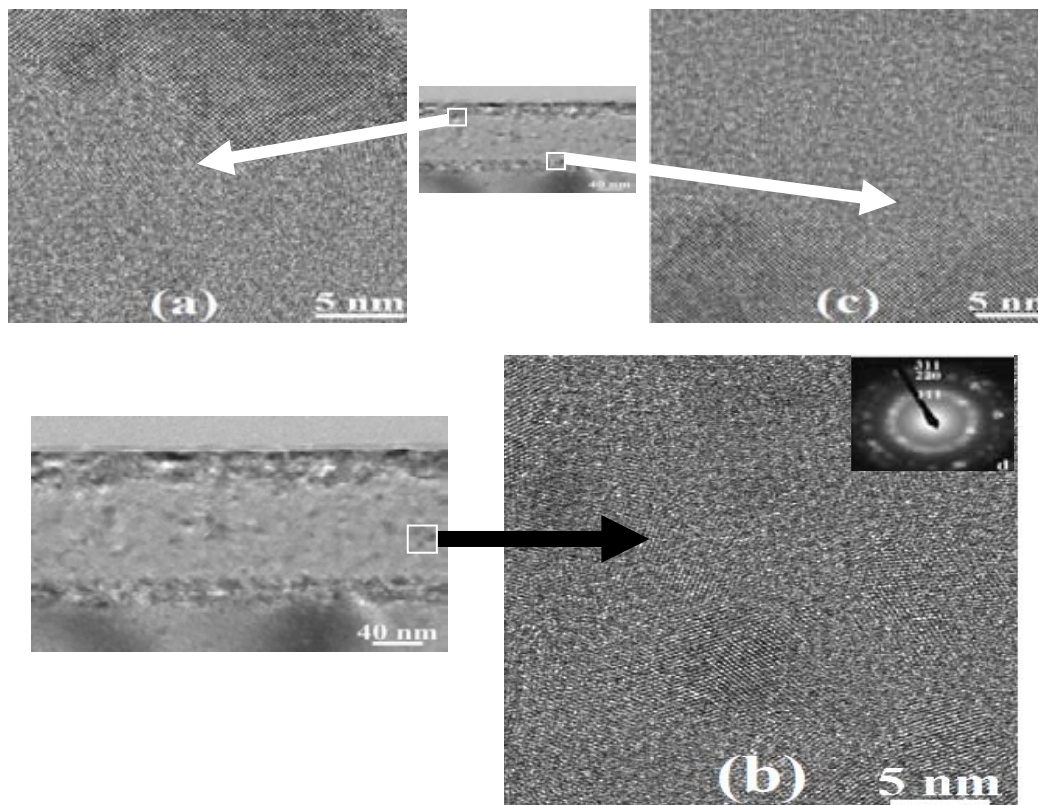


FIG. 11. Cross sectional TEM images of the ion implanted layer for the HT 1100°C-annealed sample. The SAED patterns are in accordance with cubic SiC [(111), (220) and (311)]. No amorphous (Si,C) layer is seen as only three layers are present. The average grain size of the SiC phase is ~8 nm in consistence with the XRD results. The arrows point zoomed zones from the layered structure: (a) the interface between the top d-Si and the middle SiC, (b) the SiC layer between two d-Si layers, and (c) the interface between the middle SiC and the bottom d-Si. Compared with the result of Figure 10, the HT treatment eliminates the a-SiC layers thus benefits formation of high-quality SiC crystals.

Another difference between the as-implanted and the annealed samples is that there is an amorphous layer on the surface of the annealed sample. The composition of this layer was found to be SiO₂ by using EDS and EELS. This result is consistent with the ERDA result, which shows a small amount of oxygen on the annealed sample surface. This is most likely due to oxidation during the annealing. It is generally accepted that [71] the growing of buried layer during annealing proceeds by an Ostwald ripening process, i.e. by the growth of layer precipitates in the centre of the distribution on the expense of smaller dissolving particles in the distribution wings. This process should be responsible for the growing of 3C-SiC in our experiments as well. It is obvious that the annealing improves the crystalline quality of the film, although the formation of nanocrystallites already during the implantation makes it very difficult to obtain a single crystalline 3C-SiC layer. At high temperature the system can crystallize with the preferential orientation that minimizes the surface energy. When crystalline nuclei are present before annealing, they tend to drive the crystallization process in a random manner. We believe that a single crystalline layer can be possibly achieved if the implantation temperature is lowered to room temperature. With a lower implantation temperature the middle layer will be amorphous in the as-implanted sample and during the subsequent annealing, the material will re-crystallize evenly with the substrate (100) Si as a template and the structure will not be influenced by the SiC nanocrystallites that have a rather broad distribution of their orientation.

From the studies of the characteristics of C-ion implanted Si, preliminary conclusions are

- Elevated-temperature C-ion implantation favours formation of SiC;
- Post-implantation thermal annealing favours SiC formation, and the higher the annealing temperature the better;
- The type is cubic silicon carbide, i.e. 3C-Si, or β -SiC, polycrystalline.

3.3. Swift Heavy Ion Beam Annealing (SHIBA)

After the samples were annealed by high-energy heavy ion beam, all the characterization measurements that were done for the previous samples were repeated. The results were compared with those of thermal annealing [72]. The results are shown in Figures 12–22. Relevant descriptions and discussions are given in the figure captions (where IBIEC represents ion-beam induced epitaxial crystallization, i.e. ion beam annealing).

From the characteristics of IR spectra of the SHIBA samples, the SHIBA effects of the implantation temperature, energy and fluence dependences were studied. In study on the temperature dependence, the irradiation fluence used in this case was 1×10^{12} ions/cm². During the irradiations, the samples were heated to 80, 400 and 800°C, respectively, aimed to observe the temperature dependence of the crystallization of the Si-C sub-system during MeV-ion irradiations. Four basic characteristics extracted from peaks in IR spectra are illustrated in Figure 12. As seen from the reduced FWHM of the IR peaks following the rise of target temperature, higher substrate temperature effectively increases the degree of crystallinity of the newly born phase. The substantial increase of the crystallinity with substrate temperature indicates that the process is temperature activated. It is noticed that at the lowest target temperature (80°C), the FWHM of the IR peak is higher than that of the as-implanted one.

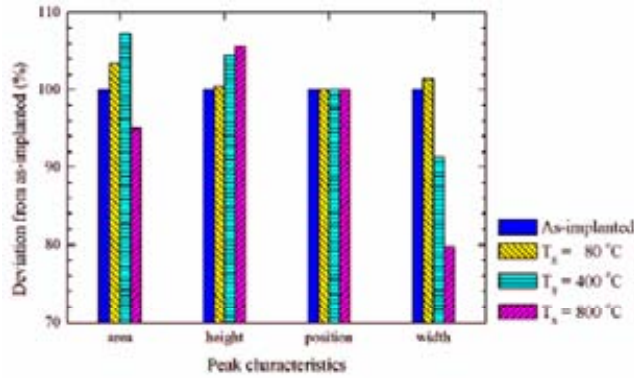


FIG. 12. Study on the implantation temperature dependence of the SHIBA effect on the IR characteristics of the 3C-SiC peaks observed from sample irradiated by 20 MeV I-ions.

This means that at this temperature, the dynamical annealing competes with damage formation, leading to destruction of the nano-crystal SiC formed during ion implantation. For the fluence dependence study, the target temperature was kept at $\sim 800^\circ\text{C}$ and three fluences, i.e. 1, 2 and 5×10^{12} ions/cm², were used, while the ion energy was kept constant at 20 MeV. Details of the IR peak characteristics extracted from spectra are illustrated in Figure 13. As observed from the figure, the peak height increases while the peak width decreases for increasing fluence. Thus, a higher fluence enhances the bonding of C-atoms to Si lattice, resulting in more SiC to be observed by IR. It is noticed that the enhancement of the crystallinity of SiC for increasing fluence is consistent with an increase in point defects, phonons, and electronic excitations at the synthesized layer. Three energies, 10, 20 and 30 MeV, were used to investigate the bombardment energy dependence of the recrystallization of SiC during the ion beam annealing, while the fluence was kept constant at 5×10^{12} ion/cm² and the target temperature was kept at 800°C . Details on peak characteristics extracted from the IR spectra are illustrated in Figure 14. It is obvious that a higher energy enhances the crystallinity of the newly born phase, as observed by the increase of the peak height and the significant reduction of the peak width. It is also noticed that, from the SIIMPL calculation, while the numbers of point defects and phonons decrease, the electronic excitation increases as a function of bombardment energy. Thus, the enhancement of the crystallinity of SiC seems in this case to be attributed to the electronic energy loss mechanism. The IR SiC peak's 1/FWHM change on $10^4/T(\text{K})$ is also analyzed (Figure 15). The slopes indicate the recrystallization activation energy of SiC [73]. The smallest slope from ion beam annealing indicates that the ion beam annealing induces the easiest recrystallization.

Figure 16 exhibits the Raman spectra of several Si samples, i.e. virgin, as-implanted, annealed at 1000°C , and samples subjected to the SHIA-process at 20 and 30 MeV to a fluence of 5×10^{12} ions/cm². For the virgin silicon sample, the spectrum shows the presence of the first and second order transverse acoustical phonon peaks (2TA) from the crystalline Si substrate at 520 and 302 cm⁻¹, respectively. A clear peak due to the Si second-order features appearing at 970 cm⁻¹ is also present in the virgin sample. In the as-implanted sample, the peak at 520 cm⁻¹ is still clear, although the Si-Si bonds are modified by the ion implantation, as evidenced by the disappearance of the peaks at 302 and 970 cm⁻¹. This means that a part of the implanted area is not amorphized but highly damaged. After thermal or ion beam annealing, the peak at 520 cm⁻¹ is sharper and the peaks at 302 and 970 cm⁻¹ are recovered. This means that the damaged silicon has been recovered. The spectrum shows “bumps” at 600–800 cm⁻¹, centred at the TO mode of 3C-SiC (~ 796 cm⁻¹) [74]. Actually, the TO mode would be forbidden in backscattering configuration for the (100) orientation. However, the partial orientation randomness of the crystallites, and the deviation from the real backscattering due

to the large aperture number of the microscope objective aimed at focusing the exciting beam, can justify the TO presence even for the more ordered SiC on Si samples. The LO mode of 3C-SiC ($\sim 973 \text{ cm}^{-1}$) [74] is impossible to identify due to the overlap with the second-order Raman signal provided by the recrystallized Si substrate. Thus, for such thin transparent films, the Raman spectra are dominated by features of the Si substrate and not the SiC. The Raman measurement might not be the right technique for comparing the Si-C products in our case, but gives valuable information on the formation of C-C bonds. As shown in the figure, the SHIBA samples do not show any response from carbon clusterization, which is usually observed as peaks at 1350 and 1580 cm^{-1} for D and G lines due to A_1 and E_{2g2} modes of graphitic crystallites, while for thermally annealed samples, a small bump is seen in that region. It is known that the penetration depth of argon laser of 514.5 nm line in the silicon is $\sim 770 \text{ nm}$. Although the formation of SiC and small structural disorder in the surface region may reduce the penetration depth of the laser, it is possible to probe the whole structural modifications in the surface region of the silicon substrate. We then conclude that the SHIBA process did not induce the formation of any C-C bonds in our samples, but thermal annealing did. We calculated the intensity ratios of the peaks at $\sim 520 \text{ cm}^{-1}$ and $\sim 970 \text{ cm}^{-1}$ and found that the ratios became 2.82, 2.97, 3.80 and 5.73 for SHIBA at 20 MeV, SHIBA at 30 MeV, thermally annealed at 1000°C , and virgin silicon, respectively. Since a higher ratio implies a better recovery of the Si substrate, it is clear that the irradiation at 30 MeV has improved the implantation-damage layer compared to the irradiation at 20 MeV, confirming the infrared measurement results.

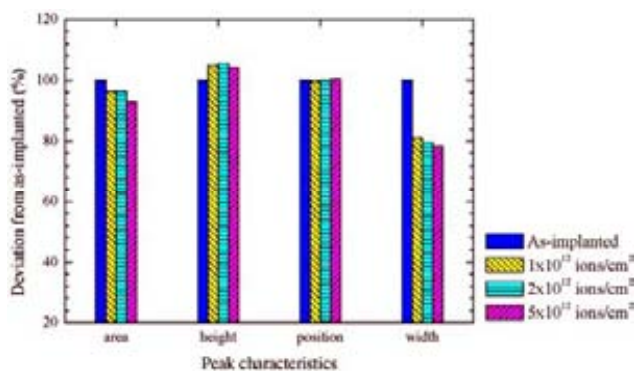


FIG. 13. Heavy ion fluence dependence of the IR characteristics of the 3C-SiC peaks observed from sample irradiated by 20 MeV I-ions. It is clearly seen that the IR peak width and area decrease and the height basically increases as increasing of the fluence, indicating that higher fluences used benefit the crystallinity.

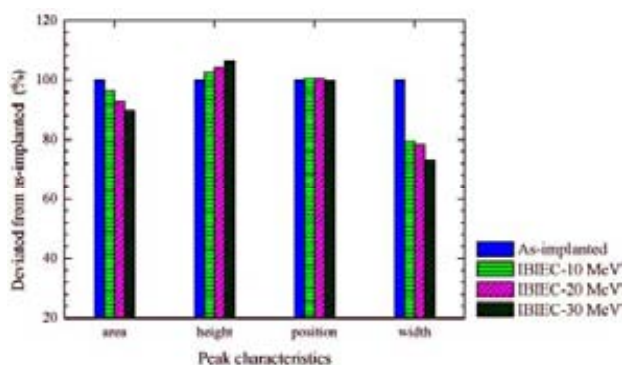


FIG. 14. Heavy ion energy dependence of the IR characteristics of the 3C-SiC peaks observed from sample irradiated by I-ions to a fluence of $5 \times 10^{12} \text{ ions/cm}^2$. It is clearly seen that the IR peak width and area decrease and the height increases as increasing of the ion energy, indicating that higher energy used benefits the crystallinity.

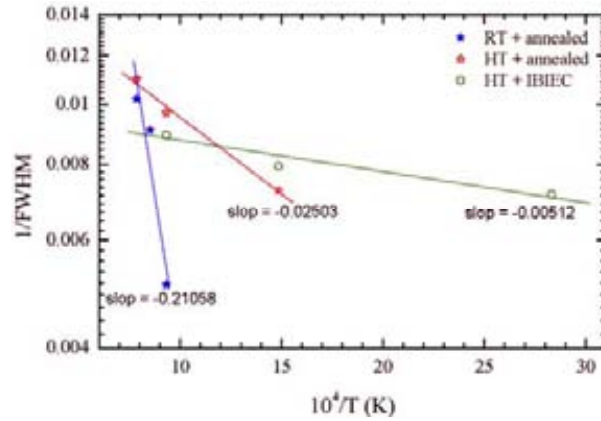


FIG. 15. The dependence of the IR SiC peak's $1/\text{FWHM}$ on $10^4/T(\text{K})$ for ion beam annealing (20 MeV , 1×10^{12}), compared with those of thermal annealing of RT- and HT-implanted samples.

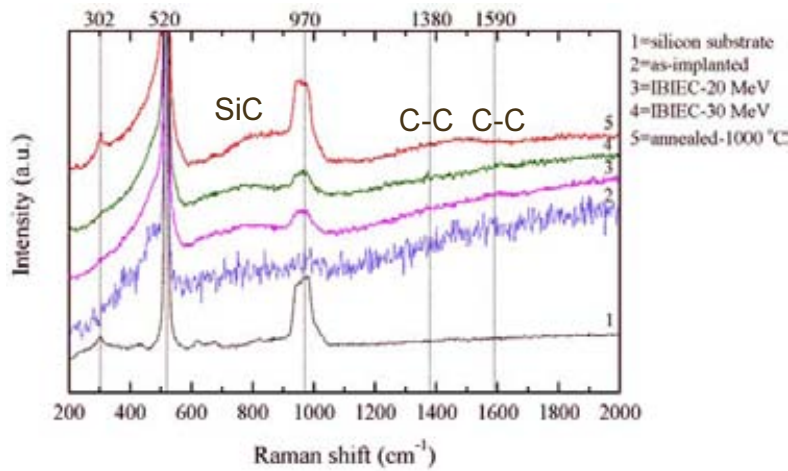


FIG. 16. Raman spectra from samples treated with different methods (heavy ion beam fluence: 5×10^{12}). Heavy ion beam annealing shows similar effect to that of thermal annealing on formation of SiC, however, no induction of graphite formation compared with thermal annealing, which results in a bump in the spectrum related to the graphite formation.

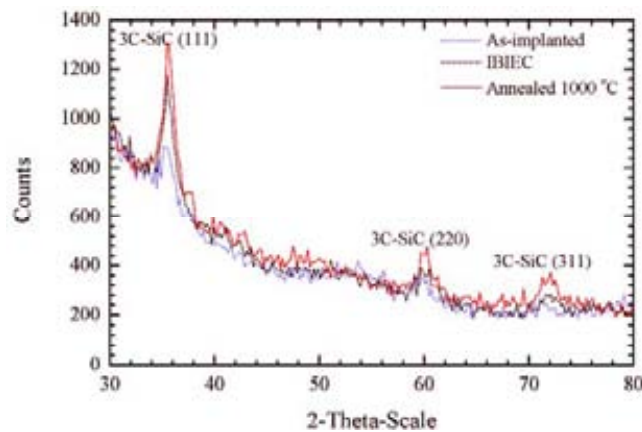


FIG. 17. GIXRD spectra at 1° of as-implanted, thermal annealed (1000°C) and ion beam annealed (20 MeV , 5×10^{12} , 800°C) of the HT C-ions implanted Si. Thermal annealing results in better crystallinity as the peaks for thermal annealing are higher. This may be due to very low ion fluence used in ion beam annealing.

For a deeper understanding of the SHIBA process, we used the GIXRD for comparison of the depth distribution of the synthesized layer using the SHIBA or the thermal annealing processes. Figure 17 shows typical GIXRD spectra at 1° glancing angle of the carbon as-implanted Si and the sample subsequently ion beam annealed at 20 MeV to a fluence of 5×10^{12} ion/cm², or the sample thermally annealed at 1000 °C. Three peaks at $2\theta = 35.5^\circ$, 60.3° and 71.9° corresponding to 3C-SiC (111), (220) and (311), respectively, indicate the appearance of the cubic SiC polytype. For the as-implanted sample, the peaks are very weak and broad, due to the poor crystalline quality, while for the post-implantation processed sample, the peaks are sharper. A comparison between the SHIBA process and the thermal annealing shows the peak intensity of the sample treated by the SHIBA process slightly lower than that of thermal annealing. However, by using the Scherrer's formula, the crystalline grain sizes of the SiC were estimated to be about 6.7, 7.8 and 7.9 nm for as-implanted, annealed at 1000°C and SHIA at 800°C samples respectively. The similarity of the grain size for the solely thermally annealed versus the SHIBA treated samples demonstrates the benefit of the SHIBA process in terms of a low processing temperature. The attenuation of X rays in materials is expressed by its linear absorption coefficient (μ). The absorption coefficients of pure materials are well documented, but not for compounds. Thus, in our calculation, we used $\mu = 147 \text{ cm}^{-1}$ for Si. However, to increase the accuracy for our special ion-implanted sample, we followed the method proposed in Ref. [75] for obtaining the absorption coefficient and found $\mu = 211 \text{ cm}^{-1}$ for poly-SiC. The penetration depth is limited to a few nm when the incident angle is lower than the critical angle. Above the critical angle, the penetration depth increases exponentially. For instance, in the case of silicon at an incident angle of 0.221° (critical angle) the penetration depth is about 20 nm and drastically increases to about 1000 nm at 1° incident angle. Thus, on the basis of GIXRD, from the spectra collected at different incident angles, it is possible to obtain structural information at different depths. Figure 18 shows some GIXRD spectra for the 3C-SiC (111) peak collected at different incident angles (from 0.15° to 2°) for as-implanted, annealed (at 1000°C), and SHIA (at 20 MeV) samples. As shown in the figure, the peak intensity of the SHIBA spectra decreases continuously upon increasing the incident angle. Especially for incident angles higher than 1° , the penetration depth of x rays is far beyond the carbon concentration peak as observed from ERDA. This implies a non-homogeneity of the synthesized layer and it means that at the depth of the carbon peak, well structured SiC can be obtained by SHIBA process, though using the lower substrate temperature. However, thermal annealing has extended the SiC layer from its centre and made the synthesized layer thicker. Accordingly, the intensities of diffraction peaks for annealed samples are similar in all investigated incident angles. This indicates that the fluences for SHIBA process in our experiments are too low to fully recrystalline the whole a-SiC layer, but only at the centre of the C-peak, confirming the results from IR.

The 20 MeV and 30 MeV I-ion-bombarded samples were investigated using transmission electron microscopy (TEM). The low magnification cross-sectional TEM image shown in Figure 19 demonstrates that the 20 MeV iodine-ions irradiated sample has a layered structure. High resolution TEM image (Figure 20) reveals that the top layer consists of single crystal silicon but with a high density of defect. The thickness of the defective silicon (d-Si) layer is ~ 29 nm. It should be pointed out that there are layer-like defects as well as twin structure in the top d-Si region. Below the top d-Si region, an amorphous region was found by high resolution TEM. The composition of the amorphous part, characterized by energy dispersive X ray spectrometry (EDS), contains Si and C. The thickness of this amorphous layer is slightly larger than 30 nm. Below this amorphous region, there is a polycrystalline layer. The high-resolution TEM image as well as a corresponding selected area electron diffraction

pattern in Figure 19 reveals that the polycrystal is 3C-SiC. The size of the 3C-SiC grain is $\sim 5\text{--}10$ nm. Similar to the structure of as-implanted sample, there is also a second amorphous (Si, C) layer between the polycrystalline 3C-SiC layer and the bottom defective silicon layer. The thickness of the second amorphous (Si, C) layer is only ~ 15 nm, which is thinner than the thickness of the first amorphous (Si, C) layer. Furthermore, as seen in the figure, no layer-like defect was found in the bottom d-Si layer. The sample irradiated by 30 MeV I-ions exhibits a similar layered structure to the low-energy irradiated sample. However, the high-energy irradiated sample has a slightly thicker 3C-SiC layer, somewhat larger grain size of 3C-SiC phase, and less disorder compared with the sample of low energy irradiation. So, increasing the ion energy appears to have a similar effect as increasing the annealing temperature for the conventional thermal annealing treatment. It is noted that no SiO_2 surface layer was found in either of the two irradiated samples. The low magnification images clearly show that there exist more defects in the silicon substrate of the irradiated samples. Those defects possibly resulted from the irradiation process during ion beam annealing.

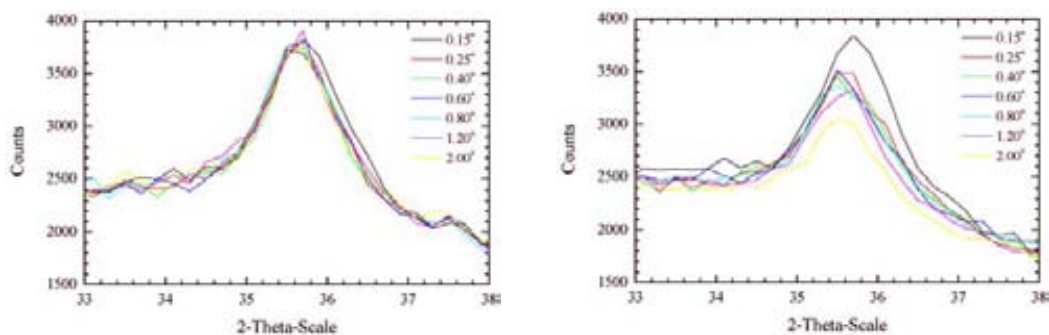


FIG. 18. The depth (incident angle) dependence of the 3C-SiC (111) peak intensity in GIXRD spectra for (a) thermal annealed (1000°C), and (b) ion beam annealed (20 MeV , 5×10^{12}) samples. Thermal annealing shows a thicker SiC layer. This may be due to heavy ion beam not powerful enough.

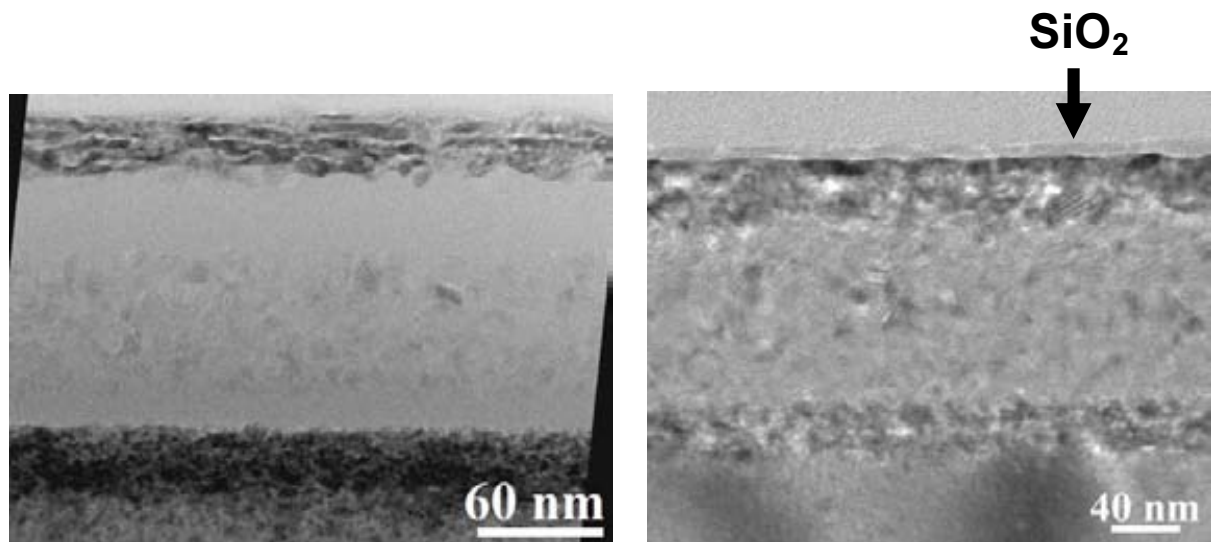


FIG. 19. Comparison of TEM cross sections between (left) ion beam annealed (20 MeV , 5×10^{12}) and (right) thermal annealed (1100°C) samples. A top layer mainly containing SiO_2 is found on the thermal annealed sample surface but not on the ion beam annealed sample surface. This is also evidence showing ion beam annealing better than thermal annealing.

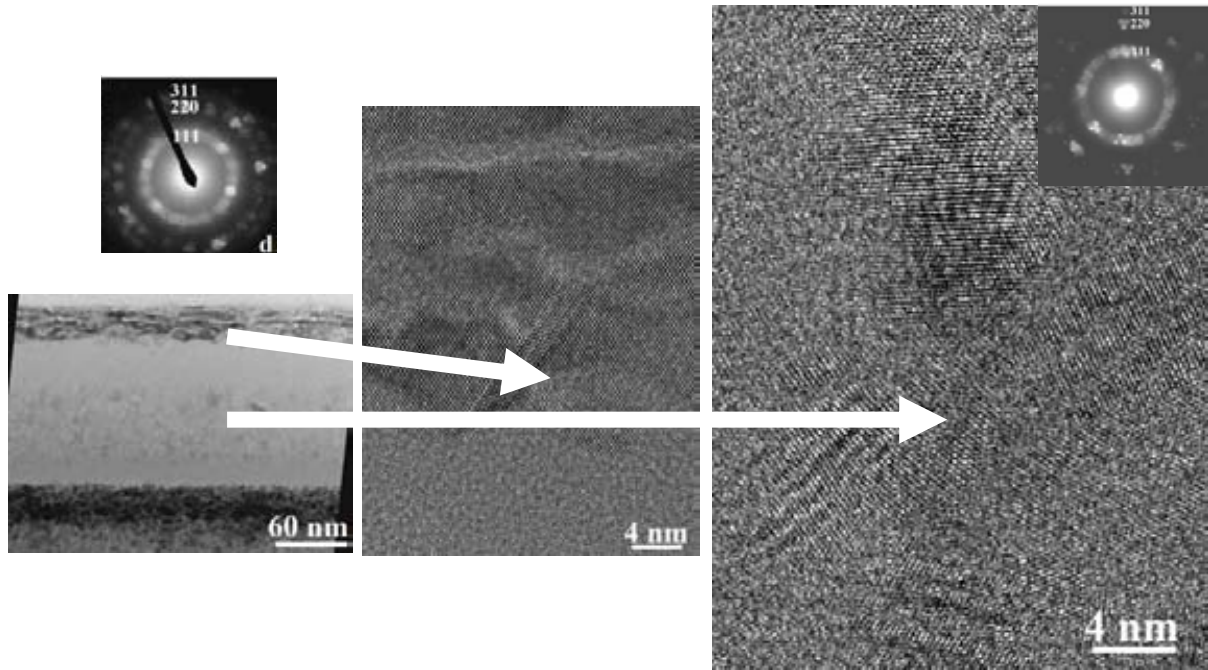


FIG. 20. TEM images of the implanted layer cross section of ion beam annealed sample (20 MeV, 5×10^{12}). The arrows point the zoomed parts. From the formed SiC zone, the SiC grain size is about a few to ten nanometers. The ion-beam-annealing SAED (the up-right inset) is clearer or sharper than thermal-annealing SAED (the up-left inset), indicating better crystallization induced by ion beam annealing.

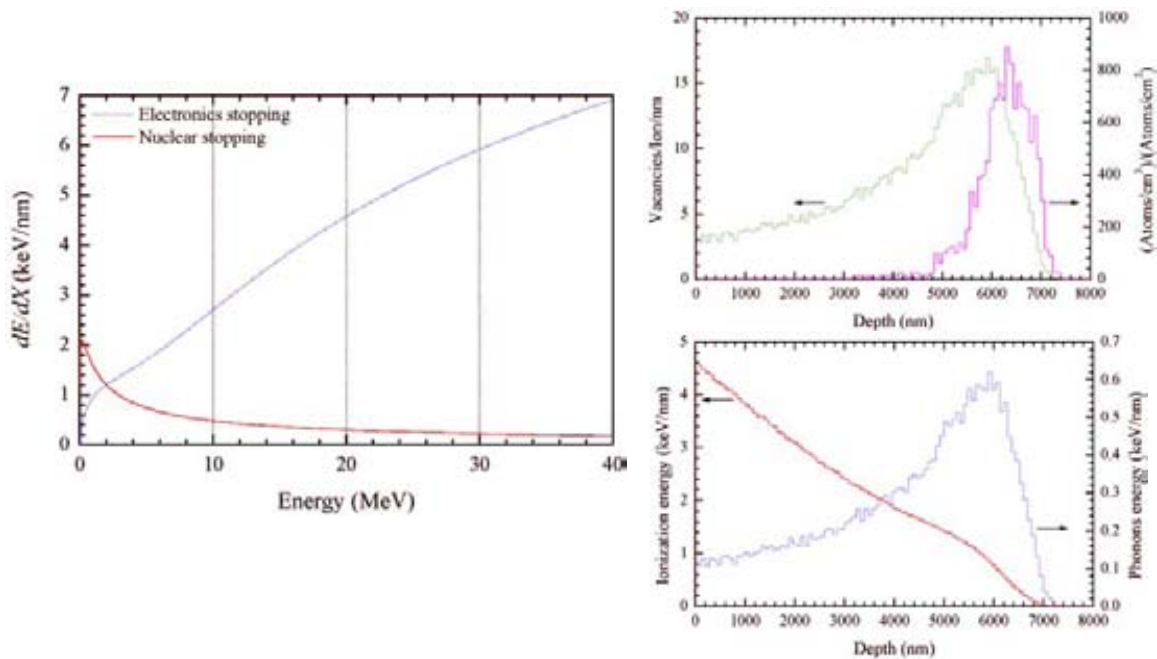


FIG. 21. Mechanism study for ion beam annealing. SRIM-simulated electronic and nuclear stopping powers of I-ion implantation in Si, and their effects occurring in 20 MeV I-ions implanted Si. Reminding of the implanted C range in Si only about a few hundreds of nanometers as shown before, we can see electronic stopping dominating the ion beam annealing process.

The mechanisms involved in SHIBA were studied. Ion implantation simulation shows that in SHIBA the electronic stopping absolutely dominates in the SHIBA ion interaction with the C-ion implanted layer in Si (Figure 21). We attribute the SHIBA effects to the inelastic thermal spikes of the swift heavy ions [76, 77]. Several observations in other material systems, such as the defect annealing [78], track formation [79], and the effects of irradiation temperature [80], support the thermal spike model. In our experiment, when the energy of the projectile increases, the electronic excitation increases, implying a higher temperature in the track and the crystallinity of the SiC improves, possibly due to higher diffusivities of point defects. Additionally, it has been simulated [81] that the spike efficiency increases when the ambient temperature increases. In our experiment, a higher irradiation temperature also improves the crystallinity of SiC in comparison to the lower temperature case owing to an increase in the spike annealing efficiency. From the TEM measurements, one can conclude that the epitaxial-like structure of Si/SiC/Si was not formed. Therefore, in our experimental conditions the irradiation of high-energy heavy ions was not able to produce epitaxial crystallization of the buried layer. However, it is obvious that the ion beam annealing improves the crystalline quality and extends the thickness of the film, although the formation of nano-crystallites already during the ion beam synthesis stage makes it very difficult to obtain a single crystalline 3C-SiC layer. The effect of SHIBA is similar to the purely thermal anneal, but when crystalline nuclei are present before annealing, the swift heavy ions tend to drive the crystallization process in different directions depending on the orientation of the original nano-crystallites [72]. We believe that a single crystalline layer can be achieved if the buried layer is in an amorphous phase. In that case, during the subsequent irradiation, the material will recrystallize evenly with the substrate (100) Si as a template and the structure will not be influenced by the SiC nanocrystallites that have a rather broad distribution of their orientation. Volz et al. [82] demonstrated that epitaxial crystallization of amorphous-like SiC formed by ion beam synthesis may be obtained by irradiation with 800 keV Si-ions. Heera et al. [83] also demonstrated that bulk (and amorphized) 6H-SiC was able to epitaxial recrystallize under irradiation of 300 keV Si-ions. In both studies the processes are dominated by the nuclear stopping mechanism. It is noticed that the fluence required for recrystallization of SiC when nuclear stopping dominates is much higher than when electronic stopping dominates, between $\sim 10^{17}$ ions/cm² and 10^{12} ions/cm². Note also that in the ion beam assisted recrystallization of SiC/Si structures using predominantly nuclear stopping, the remaining C tends to form graphitic structure [84], which is not the case for SHIBA. In the light of this technological advantage, it is worth continuing studies on the recrystallization of buried SiC layer by ion beam annealing using high-energy heavy ion beams.

For a comparison, the SHIBA effect on formation of SiC from Xe-ion beam annealing was also analyzed with Raman spectroscopy. Figure 22 shows the Raman spectra of the Xe-SHIBA samples. In a comparison among the spectra, a small peak can be identified for the higher-fluence bombarded area near 800 cm⁻¹, which is related to the TO mode of β -SiC (which should exactly be at 796 cm⁻¹), but in both spectra from the virgin and low-fluence Xe-ion beam bombarded samples no such peak is seen. This indicates that even low-energy SHIBA with appropriate ion beam fluence is already able to initiate crystallization of SiC. But in a comparison between Figure 16 and this figure, it is obviously seen that higher energy SHIBA is more effective to formation of the crystal, indicating that the factor of energy in SHIBA is dominant but not the ion beam fluence and absolutely not the total area-density energy (the product of the ion energy and the fluence) deposited. The higher the ion energy, the more the crystallization, whereas the total energy even an order higher could hardly contribute to the crystallization. For the I-SHIBA, for example, the total area-density ion energy deposited is about $20 \text{ MeV/ion} \times 2 \times 10^{12} \text{ ions/cm}^2 = 4 \times 10^{13} \text{ MeV/cm}^2$, while for the Xe-SHIBA, for example, the total energy is $4 \text{ MeV} \times 5 \times 10^{13} \text{ ions/cm}^2 = 2 \times 10^{14} \text{ MeV/cm}^2$.

This result demonstrates from an aspect that the electronic stopping plays the key role in the annealing.

Preliminary conclusions from the SHIBA studies are

- Swift heavy ion beam annealing (SHIBA) works, resulting similarly to thermal annealing;
- The higher the ion energy and fluence (in certain ranges), the better;
- Advantages of ion beam annealing compared with thermal annealing:
 - Lower temperature ($n \times 100^\circ\text{C}$ compared with $\sim 1000^\circ\text{C}$)
 - Shorter treatment time (2 min compared with 1 hour)
 - Easier recrystallization
 - No Si-oxide surface layer;
- Conditions to be optimized;
- Mechanism involved should be electronic stopping.

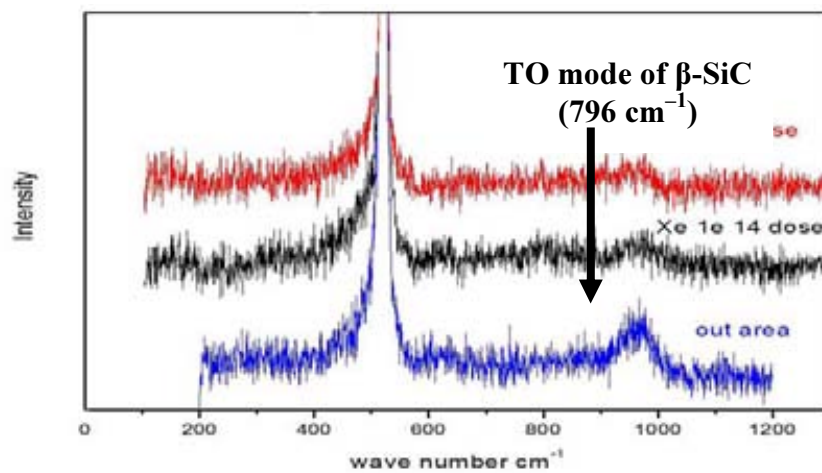


FIG. 22. Raman spectra from the virgin area (i.e. “out area”) of the C-implanted Si sample to be Xe-SHIBA and the 4-Me Xe-bombarded area of the samples with two different fluences as indicated in the figure.

3.4. Multiple-energy C-ion Implantation in Si

Multiple energy C-ion implantation was performed using medium energies of 300 to 600 keV. The use of the medium ion energy was based on the consideration of producing pure implanted profiles without other influences such as diffusion, surface segregation and evaporation. Two opposite sequences of the implantation energy were applied to test any difference in the carbon concentration distribution in the silicon wafer, namely (1) 600, 500, 400, 300 keV, and (2) 300, 400, 500, 600 keV. For each energy, the ion fluence was the same, 3.2×10^{17} ions/cm². During the ion implantation, Rutherford backscattering spectrometry (RBS) was used to analyze *in-situ* the carbon depth profiles, namely, after each energy implantation RBS analyzed the profile. The relevant results are shown in Figure 23–26. The C-ion depth profiles were extracted from the RBS spectra [85] using our self-developed program as mentioned before. As seen from the results, an extremely interesting phenomenon occurs. For the energy-decreasing sequence, the carbon depth profile is considerably broader than that from the energy-increasing sequence, which is well agreed with the program-

simulated profile. Similar phenomenon was also found previously [58]. Graphite was found to deposit on the top surface of Si after each C-ion implantation to form a C layer. The reason for the C-layer deposition is still under investigation. A postulation is the ion backscattering effect. When light ions are implanted in heavy matrix, simultaneously with ion implantation, there exists noticeable ion backscattering. The backscattered ions, particularly from the matrix top surface, with energy considerably high collide with primary incident ions above and near the matrix surface to slow down some portion of the incident ions to become very-low-energy ions. These low-energy ions act as deposited particles to form a top layer on the matrix surface. This deposited layer subsequently has an additional stopping effect to further implanting ions to affect the final ion concentration distribution. This effect is only for solid light-ion implantation but not for light gaseous ion implantation in heavy matrix as the deposited gaseous ions on the top surface are immediately vaporized. Anyway, this result is indeed informative for us to obtain a broad SiC layer buried in Si.

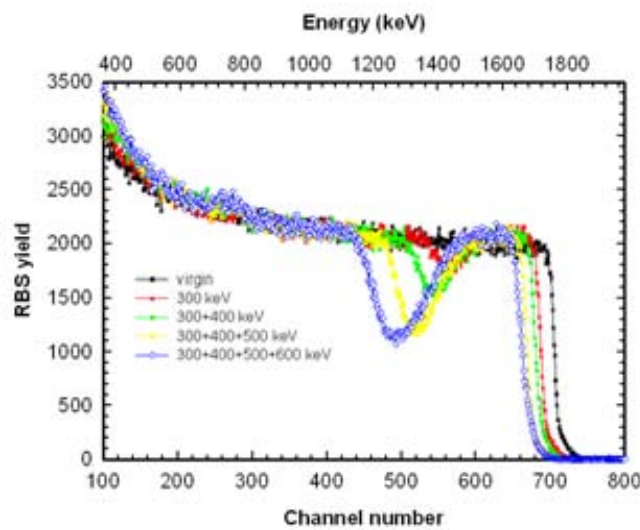


FIG. 23. 3 MeV RBS spectra of the multiple energy C-ions implanted sample with 300, 400, 500 and 600 keV $^{12}\text{C}^+$ ions.

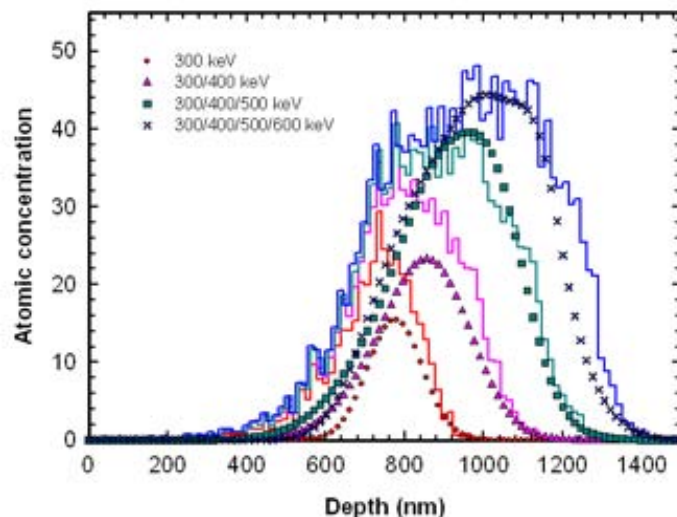


FIG. 24. Depth distributions of the atomic concentrations of the multiple energy C-ions implanted samples extracted from the RBS spectra shown in Fig. 23.

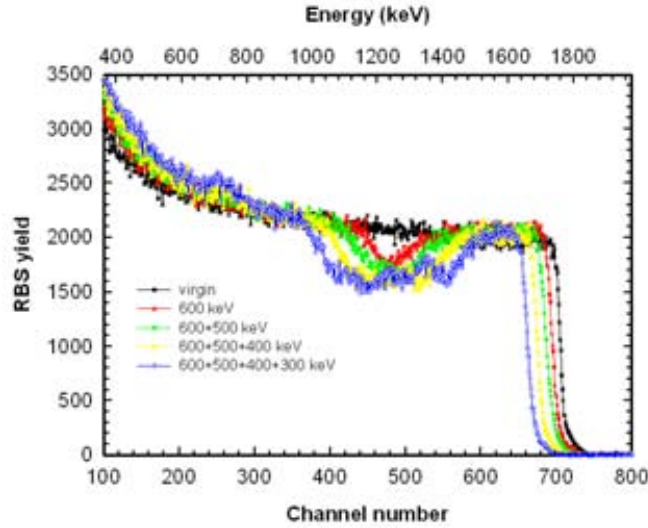


FIG. 25. 3 MeV RBS spectra of the multiple energy C-ions implanted sample with 600, 500, 400 and 300 keV $^{12}\text{C}^+$ ions.

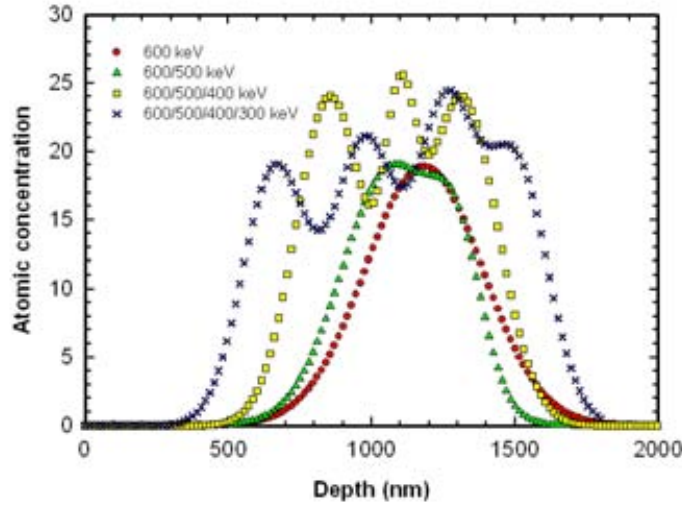


FIG. 26. Depth distributions of the atomic concentrations of the multiple energy C-ions implanted samples extracted from the RBS spectra shown in Fig. 25.

4. CONCLUSIONS

The overall conclusions drawn from the study are as follows:

- The ion beam synthesis technique developed, i.e. high-fluence C-ion implantation in Si wafer at elevated temperature followed by vacuum thermal annealing or swift heavy ion beam annealing, can form buried high-quality polycrystalline nano-grained β -SiC layer in Si wafer.
- Irradiation with swift heavy ion beams lead favourable annealing of SiC, where the effects are governed by the electronic stopping process.
- Neither elevated-temperature ion implantation nor post-implantation thermal annealing can broaden the implanted high-concentration carbon profile. However, multiple-energy C-ion implantation in Si, particularly in the energy-decreasing sequence, favors obtaining a broad buried SiC layer.

ACKNOWLEDGEMENTS

We wish to thank A. Hallén of Royal Institute of Technology, Sweden, M.S. Janson of Department of Physics & Astronomy, University of California, Irvine, USA, G. Possnert of Angstrom Laboratory, Division of Ion Physics, Uppsala University, Sweden, K. Kirkby of Surrey Ion Beam Center, University of Surrey, UK, J. Lu of Department of Engineering Sciences, Uppsala University, Sweden, M. Ottosson of Department of Materials Chemistry, Uppsala University, Sweden, S. Dangtip of Department of Physics, Faculty of Science, Mahidol University, Thailand, and C. Thongleum of Institute for Science & Technology Research & Development, Chiang Mai University, Thailand for collaborations and assistance. This project was supported by the International Atomic Energy Agency under the Coordinated Research Projects on Ion Beam Modification of Insulators.

REFERENCES

- [1] TONG, L., MEHREGANY, M., MATUS, L.G., *Mechanical properties of 3C silicon carbide*, Appl. Phys. Lett. 60 (1992) 2992.
- [2] MORKOC, H., STRITE, S., GAO, G.B., LIN, M.E., SVERDLOV, B., BURNS, M., *Large-band-gap SiC, III-V nitride, and II-VI ZnSe-based semiconductor device technologies*, J. Appl. Phys. 76 (1994) 1363.
- [3] NEJIM, A., HEMMENT, P.L., STOEMENOS, *SiC buried layer formation by ion beam synthesis at 950°C*, J. Appl. Phys. Lett. 66 (1995) 2646.
- [4] LINDNER, J.K.N., STRITZKER, B., *Mechanisms in the ion beam synthesis of SiC layers in silicon*, Nucl. Instrum. Methods B 148 (1999) 528.
- [5] NAKATA, J., *Mechanism of low-temperature ($\leq 300^\circ\text{C}$) crystallization and amorphization for the amorphous Si layer on the crystalline Si substrate by high-energy heavy-ion beam irradiation*, Phys. Rev. B 43 (1991) 14643.
- [6] JACKSON, K.A., *A defect model for ion-induced crystallization and amorphization*, J. Mater. Res. 3 (1988) 1218.
- [7] PRIOLO, F., and RIMINI, E., *Ion-beam-induced epitaxial crystallization and amorphization in silicon*, Mater. Sci. Rep. 5 (1990) 319.
- [8] PRIOLO, F., SPINELLA, C. RIMINI, E., *Phenomenological description of ion-beam-induced epitaxial crystallization of amorphous silicon*, Phys. Rev. B 41 (1990) 5235.
- [9] WILLIAMS, J.S. and ELLIMAN, R.G., *Role of Electronic Processes in Epitaxial Recrystallization of Amorphous Semiconductors*, Phys. Rev. Lett. 51 (1983) 1069.
- [10] WILLIAMS, J.S., ELLIMAN, R.G., BROWN, W.L., SEIDEL, T.E., *Dominant Influence of Beam-Induced Interface Rearrangement on Solid-Phase Epitaxial Crystallization of Amorphous Silicon*, Phys. Rev. Lett. 55 (1985) 1482.
- [11] CUSTER, J.S., BATTAGLIA, A., SAGGIO, M., PRIOLO, F., *Growth-site-limited crystallization of amorphous silicon*, Phys. Rev. Lett. 69 (1992) 780.
- [12] KOBAYASHI, N., HASEGAWA, M., HAYASHI, N., *Low-energy ion-beam-induced epitaxial crystallization of GaAs*, Nucl. Instrum. Methods B 80/81 (1993) 790.
- [13] HEERA, V., HENKEL, T., KOEGLER, R., SKORUPA, W., *Evidence for diffusion-limited kinetics of ion-beam-induced epitaxial crystallization in silicon*, Phys. Rev. B 52 (1995) 15776.
- [14] NAKATA, J., *Evidence of enhanced epitaxial crystallization at low temperature by inelastic electronic scattering of mega-electron-volt heavy-ion-beam irradiation*, J. Appl. Phys. 79 (1996) 682.

- [15] HEERA, V., *Comment on “Evidence of enhanced epitaxial crystallization at low temperature by inelastic electronic scattering of mega-electron-volt heavy-ion-beam irradiation”*, J. Appl. Phys. 80 (1996) 4235.
- [16] NAKATA, J., *Reply to “Comment on ‘Evidence of enhanced epitaxial crystallization at low temperature by inelastic electronic scattering of mega-electron-volt heavy-ion-beam irradiation’”*, J. Appl. Phys. 80 (1996) 4237.
- [17] NAKATA, J., *Epitaxial crystallization during 600°C furnace annealing of amorphous Si layer deposited by low-pressure chemical-vapor-deposition and irradiated with 1-MeV Xe ions*, J. Appl. Phys. 82 (1997) 5546.
- [18] NAKATA, J., *Enhanced crystallization of amorphous Si containing hydrogen without oxygen during ion-beam irradiation at 310 °C and during furnace annealing below 450°C*, J. Appl. Phys. 82 (1997) 5433.
- [19] CHOYKE, W.J., MATSUNAMI, H., PENSL, G., *Silicon Carbide — Recent Major Advances*, Springer, NY. (2004).
- [20] BORDERS, J.A., PICRAUX, S.T., BEEZHOLD, W., *Formation of SiC in Silicon by Ion Implantation*, Appl. Phys. Lett. 18 (1971) 509.
- [21] VAIBYANATHAN, K.V., *Local- and defect-mode infrared absorption of carbon ions implanted in silicon*, J. Appl. Phys. 44 (1973) 583.
- [22] MARTIN, P., DAUDIN, B., DUPUY, M., ERMOLIEF, A., OLIVIER, M., PAPON, A.M., ROLLOND, G., *High-temperature ion beam synthesis of cubic SiC*, J. Appl. Phys. 67 (1990) 2908.
- [23] REESON, K.J., STOEMENOS, J., HEMMENT, P.L.F., *Mechanism of buried β -SiC formation by implanted carbon in silicon*, Thin Solid Films 191 (1990) 147.
- [24] MASAHIRO, D., AKIHISA, Y., MASATOSHI, K., TAKASHI, H., *β -SiC Formation by Low-Energy Ion-Doping Technique*, Jpn. J. Appl. Phys. 29 (1990) 1493.
- [25] KOEGLER, R., EICHHORN, F., MUECKLICH, A., REUTHER, H., HEERA, V., SKORUPA, W., LINDNER, J.K.N., *SiC precipitates formed in Si by simultaneous dual beam implantation of C^+ and Si^+ ions*, Nucl. Instrum. Methods. B 206 (2003) 989.
- [26] LINDNER, J.K.N., *High-dose carbon implantations into silicon: fundamental studies for new technological tricks*, Appl. Phys. A 77 (2003) 27.
- [27] WESCH, W., *Silicon carbide: synthesis and processing*, Nucl. Instrum. Methods. B 116 (1996) 305.
- [28] CHAYAHARA, A., KINCHI, M., KINOMURA, A., MOKUNO, Y., *Formation of Crystalline SiC Buried Layer by High-Dose Implantation of MeV Carbon Ions at High Temperature*, Jpn. J. Appl. Phys., Part 2 32 (1993) L1286.
- [29] LINDNER, J.K.N., VOLTZ, K., PRECKWINKEL, U., GOETZ, B., FROHNWIESER, A., RAUSCHENBACK, B., STRITZKER, B., *Formation of buried epitaxial silicon carbide layers in silicon by ion beam synthesis*, Mater. Chem. Phys. 46 (1996) 147
- [30] KIMURA, T., YUGO, S., ZHOU, S.B., ADACHI, Y., *Formation of silicon carbide layers by the ion beam technique and their electrical properties*, Nucl. Instrum. Methods. B 39 (1989) 238.
- [31] SRIKANTH, K., CHU, M., ASHOK, S., NGUYEN, N., VEDAM, K., *High-dose carbon ion implantation studies in silicon*, Thin Solid Films 163 (1988) 323.
- [32] KIMURA, T., KAGIYAMA, Sh., YUGO, Sh., *Structure and annealing properties of silicon carbide thin layers formed by implantation of carbon ions in silicon*, Thin Solid Films 81 (1981) 319.

- [33] KIMURA, T., KAGIYAMA, Sh., YUGO, Sh., *Auger electron spectroscopy analysis of SiC layers formed by carbon ion implantation into silicon*, Thin Solid Films 122 (1984) 165.
- [34] KIMURA, T., TATEBE, Y., KAWAMURA, A., YUGO, Sh., ADACHI, Y., *Low-Temperature Formation of β -Type Silicon Carbide by Ion-Beam Mixing*, Jpn. J. Appl. Phys. 24 (1985) 1712.
- [35] KIMURA, T., KAGIYAMA, Sh. YUGO, Sh., *Characteristics of the synthesis of β -SiC by the implantation of carbon ions into silicon*, Thin Solid Films 94(1982) 191.
- [36] NUSSUPOV, K.Kh., SIGLE, V.O., BEJSEKHOV, N.B., *Investigation of the formation of Si and SiC crystalline phases in room temperature C⁺ implanted Si*, Nucl. Instrum. Methods B 82 (1993) 69.
- [37] DURUPT, P., CANUT, B., GAUTHIER, J.P., ROGER, J.A., PIVOT, J., *RBS, infrared and diffraction compared analysis of SiC synthesis in C implanted silicon*, Mater. Res. Bull. 15 (1980) 1557.
- [38] EDELMAN, F.L., KUZNETSOV, O.N., LEZHEIKO, L.V., LUBOPYTOVA, E.V., *Formation of SiC and Si₃N₄ in silicon by ion implantation*, Radiat. Eff. 29 (1976) 13.
- [39] AKIMCHENKO, I.P., KISSELEVA, K.V., KRASNOPEVTSEV, V.V., TOURYANSKI, A.G. AND VAVILOV, V.S., *Structure and optical properties of silicon implanted by high doses of 70 and 310 keV carbon ions*, Radiat. Eff. 48 (1980) 7.
- [40] ROTHEMUND, W., and FRITZSCHE, C.R., *Optical absorption and electrical conductivity of silicon carbide films produced by ion implantation*, J. Electrochem. Soc. 121 (1974) 586.
- [41] NGUYEN, N.V., and VEDAM, K., *Spectroscopic ellipsometry studies of crystalline silicon implanted with carbon ions*, J. Appl. Phys. 67 (1990) 3555.
- [42] REESON, K.J., HEMMENT, P.L.F., STOEMENOS, J., DAVIS, J., CELLER, G.E., *Formation of buried layers of β -SiC using ion beam synthesis and incoherent lamp annealing*, Appl. Phys. Lett. 51 (1987) 2242.
- [43] ZEROAL, B., and CARTER, G., *Low energy ion beam annealing of incompletely amorphised layers in Si*, Nucl. Instrum. Methods B 44 (1990) 318.
- [44] NELSON, R.S., HUDSON, J.A., MAZEY, D.J., *The stability of precipitates in an irradiation environment*, J. Nucl. Mater. 44 (1972) 318.
- [45] WILLIAMS, J.S., RIDGWAY, M.C., ELLIMAN, R.G., DAVIES, J.A., JOHNSON, S.T., PALMER, G.R., *MeV ion-beam annealing of semiconductor structures*, Nucl. Instrum. Methods B 55 (1991) 602.
- [46] SPINELLA, C., LOMBARDO, S., PRIOLO, F., *Crystal grain nucleation in amorphous silicon*, J. Appl. Phys. 84 (1998) 5383.
- [47] ROMANO-RODRIGUEZ, A., SERRE, C., CALVO-BARRIO, L., PEREZ-RODRIGUEZ, A., MORANTE J.R., KOEGLER, R., SKORUPA, W., *Detailed analysis of fl-SiC formation by high dose carbon ion implantation in silicon*, Mater. Sci. Eng. B 36 (1996) 282.
- [48] SRIM Program (2003), www.research.ibm.com/ionbeams/srim/
- [49] JANSON, M.S., *Hydrogen diffusion and ion implantation in silicon carbide*, Ph.D. Thesis, Royal Institute of Technology Stockholm (2003), ISSN 0284-0545.
- [50] SURREY ION BEAM CENTER (2005), www.ee.surrey.ac.uk/IBC/ndf/
- [51] INTARASIRI, S., KAMWANNA, T., HALLEN, A., YU, L.D., JANSON, M.S., THONGLEUM, C., POSSNERT, G., SINGKARAT, S., *RBS and ERDA Determinations of Depth Distributions of High-fluence Carbon Ions Implanted in Silicon for Silicon-carbide Synthesis Study*, Nucl. Instrum. Methods B 249 (2006) 859.

- [52] ZHANG, Y., WHITLOW, H.J., WINZELL, T., BUBB, I.F., SAJAVAARA, T., JOKINEN, J., ARSTILA, K., KEINONEN, J., *Detection efficiency of time-of-flight energy elastic recoil detection analysis systems*, Nucl. Instrum. Methods. B 149 (1999) 477.
- [53] Fast ComTee GmbH, *Multiparameter Data Acquisition System User Manual*, Germany (2002).
- [54] JANSON, M.S., *CONTES Instruction Manual*, Internal Report, Uppsala University (2004).
- [55] TIPPING, A.K., et al., *The diffusion coefficient of interstitial carbon in silicon*, Semicond. Sci. Tech. 2 (1987) 315.
- [56] INTARASIRI, S., KAMWANNA, T., HALLEN, A., YU, L.D., JANSON, M.S., THONGLEUM, C., POSSNERT, G. SINGKARAT, S., *Characterization of Crystalline Quality of β -SiC Formed by Ion Beam Synthesis*, Nucl. Instrum. Methods B 249 (2006) 851.
- [57] KATAGAMA, Y., USAMI, K., SHIMADA, T., *Chemical bonding states in the amorphous $\text{Si}_x\text{C}_{1-x}$: H system studied by X-ray photoemission spectroscopy and infrared absorption spectra*, Philos. Mag. B 43 (1981) 283.
- [58] ISHIKAWA, J., and TSUIJI, H., *Carbon negative ion implantation into silicon*, Nucl. Instrum. Methods B 74 (1993) 118.
- [59] ZORBA, T., SIAPKAS, D.I. KATSIDIS, C.C., *Optical characterization of thin and ultrathin surface and buried cubic SIC layers using FTIR spectroscopy*, Microelectron. Eng. 28 (1995) 229.
- [60] OLEGO, D. and CARDONA, M., *Pressure dependence of the optical phonons and transverse effective charge in 3C-SiC*, Phys. Rev. B 25 (1982) 3878.
- [61] CHEHAIDAR, A., CARLES, R., ZWICK, A., MEUNIER, C., CROS, B. DURAND, J., *Chemical bonding analysis of α -SiC: H films by Raman spectroscopy*, J. Non-Cryst. Solids 169 (1994) 37.
- [62] BULLOT, J., SCHMIDT, M.P., *Physics of Amorphous Silicon-Carbon Alloys*, Phys. Status Solidi B 143 (1987) 345.
- [63] JCPDS card No. 29-1129.
- [64] SCHERRER, P., *Göttinger Nachrichten* (1918); ZSIGMONDY, R., *Kolloidchemie*, 3rd Ed. (1920), p. 394.
- [65] INTARASIRI, S., HALLEN, A., LU, J., JENSEN, J., YU, L.D., BERTILSSON, K., SINGKARAT, S., POSSNERT, G., *Activation Energy of the Growth of Ion-beam-synthesized Nano-crystalline 3C-SiC*, Nucl. Instrum. Methods B 257 (2007) 195.
- [66] INOUE, S., YOSHI, K., UMENO, M., and KAWABE, H., *Crystallization behaviour of amorphous SiC films prepared by r.f. sputtering*, Thin Solid Films 151 (1987) 403.
- [67] CALGANO, L., MUSUMECI, P., ROCCAFORTE, F., BONGIORNO, C., FOTI, G., *Crystallisation mechanism of amorphous silicon carbide*, G., Appl. Surf. Sci. 184 (2001) 123.
- [68] INTARASIRI, S., HALLEN, A., LU, J., JENSEN, J., YU, L.D., BERTILSSON, K., SINGKARAT, S., POSSNERT, G., *Crystalline Quality of 3C-SiC Formed by High-fluence C-ion Implantation in Si*, Appl. Surf. Sci. 253 (2007) 4836.
- [69] LINDNER, J.K.N., *Ion Beam Synthesis of buried SiC layers in silicon: Basic physical process*, Nucl. Instrum. Methods B 178 (2001) 44.
- [70] NEWMAN, R.C., WAKEFIELD, J. *The diffusivity of carbon in silicon*, J. Phys. Chem. Solids 19 (1961) 230.
- [71] REESON, K.J., *Fabrication of buried layers of SiO_2 and Si_3N_4 a using ion beam synthesis*, Nucl. Instrum. Methods B 19/20 (1987) 269.

- [72] INTARASIRI, S., et al., *Effects of Low-fluence Swift Iodine Ion Bombardment on the Crystallization of Ion-beam-synthesized Silicon Carbide*, J. Appl. Phys. 101 (2007) 084311.
- [73] DKAKI, M., CALCAGNO, L., MAKTHARI, A.M., RAINERI, V., *Infrared spectroscopy and transmission electron microscopy of polycrystalline silicon carbide*, Mat. Science in Semiconductor Processing 4 (2001) 201.
- [74] FENG, Z.C., MASCARENHAS, A.J., CHOYKE, W.J., POWELL, J.A., *Raman scattering studies of chemical-vapor-deposited cubic SiC films of (100) Si*, J. Appl. Phys. 64 (1988) 3176.
- [75] SASAKI LABO., MSL, Tokyo Inst. Of Tech., Japan <http://lipro.msl.titech.ac.jp/abcoeff/abcoeff2.html> (2007).
- [76] SZENES, G., *General features of latent track formation in magnetic insulators irradiated with swift heavy ions*, Phys. Rev. B 51 (1995) 8026.
- [77] TOULEMONDE, M., DUFOUR, Ch., WANG, Z., PAUMIER, E., *Atomic and cluster ion bombardment in the electronic stopping power regime: A thermal spike description*, Nucl. Instrum. Methods B 112 (1996) 26.
- [78] WANG, Z.G., DUFOUR, Ch., PAUMIER, E., TOULEMONDE, M., *Defects in metals induced by nuclear collisions and their modifications by swift heavy ion irradiations*, Nucl. Instrum. Methods B 115 (1996) 577.
- [79] TOULEMONDE, M., BOUFFARD, S., STUDER, F., *Swift heavy ions in insulating and conducting oxides: tracks and physical properties*, Nucl. Instrum. Methods B 91 (1994) 108.
- [80] DUFOUR, Ch., BEUNEU, F., PAUMIER, E., TOULEMONDE, M., *Experimental evidence of the irradiation temperature effect in bismuth under swift heavy-ion irradiation*, Europhys. Lett. 45 (1999) 585.
- [81] TOULEMONDE, M., DUFOUR, Ch., PAUMIER, E., *The Ion-Matter Interaction with Swift Heavy Ions in the Light of Inelastic Thermal Spike Model*, Acta Phys. Pol. A 109 (2006) 311.
- [82] VOLZ, K., LINDNER, J.K.N., STRITZKER, B., *Ion beam induced amorphization and recrystallization of Si/SiC/Si layer systems*, Nucl. Instrum. Methods Phys. Res. B 120 (1996) 133.
- [83] HEERA, V., STOEMENOS, J., KOGLER, R., SKORUPA, W., *Amorphization and recrystallization of 6H-SiC by ion-beam irradiation*, J. Appl. Phys. 77 (1995) 2999.
- [84] PEREZ-RODRIGUEZ, A., KOGLER, R., CALVO-BARRIO, L., SERRE, C., ROMANO-RODRIGUEZ, A., HEERA, V., SKORUPA, W., MORANTE, J.R., *Ion beam assisted recrystallization of SiC/Si structures*, Nucl. Instrum. Methods Phys. Res. B 112 (1996) 334.
- [85] KAMWANNA, T., YU, L.D., INTARASIRI, S., SINGKARAT, S., HALLEN, A., *RBS Analysis of Light Carbon Ions in Implanted Heavy Silicon Single Crystal*, presented to the 19th International Conference on Ion Beam Analysis (IBA2007), Hyderabad, India, Sep. 23–29, 2007).

OPTIMIZED PRE-AMORPHIZATION CONDITIONS FOR THE FORMATION OF HIGHLY ACTIVATED ULTRA SHALLOW JUNCTIONS IN SILICON-ON-INSULATOR

J.J. Hamilton, K.J. Kirkby

Surrey Ion Beam Centre Advanced Technology Institute, University of Surrey,
Guildford, Surrey, GU2 7XH, UK

Abstract. Pre-amorphization of ultrashallow implanted boron in Silicon-on-insulator is optimized to produce an abrupt box-like doping profile with negligible electrical deactivation and significantly reduced transient enhanced diffusion. The effect is achieved by positioning the as-implanted amorphous/crystalline interface close to the buried oxide interface, to minimize interstitials whilst leaving a single-crystal seed to support solid-phase epitaxy. Based on a simple physical model of our results, we estimate that the interface between the Si overlayer and the buried oxide is an efficient interstitial sink with a recombination length of the order of 10nm or less under our experimental conditions.

Formation of highly activated, ultra-shallow and abrupt profiles is a key requirement for the next generation of CMOS devices, particularly for source-drain extensions [1]. For p-type dopant implants (boron), a promising method of increasing junction abruptness is to use Ge preamorphizing implants (PAI) prior to ultra-low energy B implantation. Advantages of this method are a reduction in the B channelling and an increase in B electrical activation due to the solid-phase-epitaxial (SPE) regrowth process [2]. In future technology nodes, bulk silicon wafers may be supplanted by Silicon-on-Insulator (SOI) since it can offer many advantages over bulk silicon [3].

Unfortunately after SPER interstitial defects remain located at depths greater than the initial amorphous/crystalline (a/c) interface. These excess interstitial atoms agglomerate into 'end-of-range' (EOR) defects situated just below the former a/c interface. During higher temperature annealing these defects undergo a series of transitions from self-interstitial clusters, to {113} defects to dislocation loops depending on the initial PAI and subsequent processing conditions [4]. These defects dissolve during annealing, the self interstitials so released migrate to nearby sinks such as the silicon surface [4]. Transient Enhanced Diffusion (TED) and B electrical de-activation are caused by self interstitials released from the EOR band, which diffuse towards the silicon surface during annealing. These self interstitials are also implicated in the formation of boron interstitial clusters (BICs).

Previous results have shown that electrical deactivation is reduced in SOI compared to bulk Si [5]. This is due to the upper buried oxide (BOX) interface effectively "soaking up" the interstitials from the EOR defect band that would ordinarily move toward the surface. This is explained by the fact that the oxide interface acts as a sink for point-defects coupled with the knowledge that B deactivation is driven by self interstitials released from EOR defects [6]. This work investigates the optimal conditions for B activation using Ge PAI in SOI and develops a model to explain the process.

Experiments were performed on n-type $\langle 100 \rangle$ Cz silicon wafers with a resistivity of $\sim 10\text{--}25 \Omega\cdot\text{cm}$, and on SOI wafers with a 145 nm-thick buried oxide and a 55 nm-thick p-type Si over layer. Silicon and SOITEC[©] SOI wafers were implanted with Ge⁺ at 8, 20, 24, 28, 32 or 36 keV to a dose of $1 \times 10^{15} \text{ cm}^{-2}$, amorphising to depths of $\sim 20, 40, 45, 50, 55$ and 60 nm respectively as determined by Rutherford Backscattering Spectrometry (RBS). The implants were performed using an Applied Materials Quantum X high current Implanter, with an implant orientation of 0° tilt and 0° twist. Boron was subsequently implanted at an energy of 500 eV to a dose of $2 \times 10^{15} \text{ B cm}^{-2}$. The SPE re-growth process was performed at a temperature of 570°C for consistency with previous studies [7] using annealing times from 30 s to 180 s in N₂ ambient. Normal and glancing-exit Rutherford Backscattering Spectrometry (RBS) measurements were used to monitor the re-growth of the amorphous silicon. The amorphous depth was measured using a 1.5 MeV He beam at a glancing angle of 45° to the sample, and the resulting spectra were analysed using the IBA Data Furnace software developed at the University of Surrey [8].

To study the electrical (de)activation of the boron, isochronal annealing (60 s) was carried out using a Process Products Corporation 18 Lamp rapid thermal processing (RTP) annealer, over a temperature range of $700\text{--}1000^\circ\text{C}$, pre-regrowth. The samples were analyzed by Hall Effect measurements using an Accent HL5500 Machine. Rutherford Backscattering was performed in order to check that the samples had recrystallized during annealing, results for the 32 keV and 36 keV Ge PAI in SOI are shown in Fig. 1. A selected portion of the RBS spectra (channel 235 to 265) was chosen to show and emphasize the Si amorphous peaks seen for both PAI conditions. The top figure shows spectra for the 32 keV Ge PAI normal random and channelled spectra and also channelled spectra for samples annealed at 570°C for 76 and 180 s, the lower figure is the same but for 36 keV Ge PAI condition.

In order to determine these regrowth anneal times at 570°C , simulations were made using activation energies from G.E. Olson [9]. Annealing for 180 s would be enough time for the 36 keV Ge PAI samples to fully recrystallize, according to the simulations. The regrowth velocity would be further increased with the presence of boron in the samples [5][9]. For the 32 keV Ge PAI case (top of Fig. 1) there is some re-growth after 76 s anneal time and full recrystallisation is after 180 s, this is shown by a decrease in the amorphous peak size. However the RBS shows that 36 keV Ge PAI in SOI does not recrystallise as a single crystal this is shown by the fact that the channelled and amorphous spectra are coincident for all annealing times.

Since there is not enough of a Si crystal seed (the amorphous layer interface overlaps the BOX interface leaving no single crystal between the two) in the Si overlayer of the 36 keV Ge PAI SOI, SPER can not occur. This presents a limit for the PAI technique in SOI.

Figure 2a shows a bright-field (BF) XTEM micrograph for the case of as-implanted 32 keV Ge in SOI. A thin (~ 4 nm) layer of single crystal Si remains between the amorphous layer and the upper BOX interface. Figure 2b & c show WB dark field micrographs for SOI and bulk Si samples with the same implant condition, after annealing at 700°C for 60 s. Here the amorphous layer is no longer visible and the regrown region consists of single-crystal Si, indicating that SPER has occurred from a single-crystal seed. In the bulk case (Fig. 2c) a band of EOR defects is visible at a depth of ~ 60 nm from the sample surface, but in the SOI (Fig. 2b) no significant defect accumulation is found, and high-resolution imaging (not shown) detects only a small number of isolated $\{113\}$ defects close to the BOX interface.

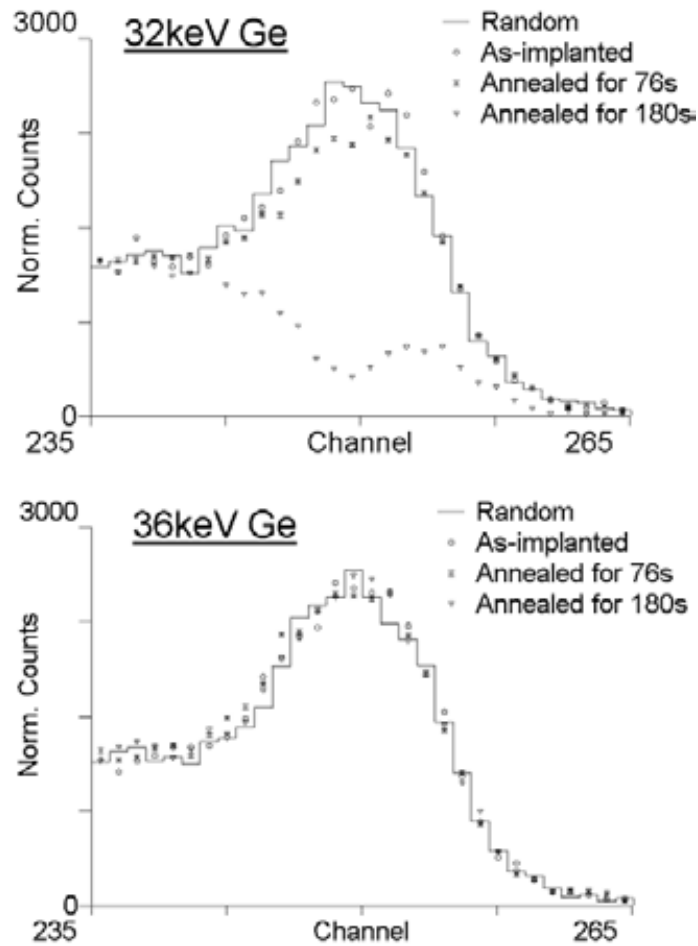


FIG. 1. RBS spectra for 32keV (top) and 36keV (bottom) Ge PAI condition in SOI material. Both figures show the as-implanted random (solid line) and channelled spectra (circles), channelled spectra for annealed samples at 570°C for 76s (hourglass) and 180s (inverted triangle).

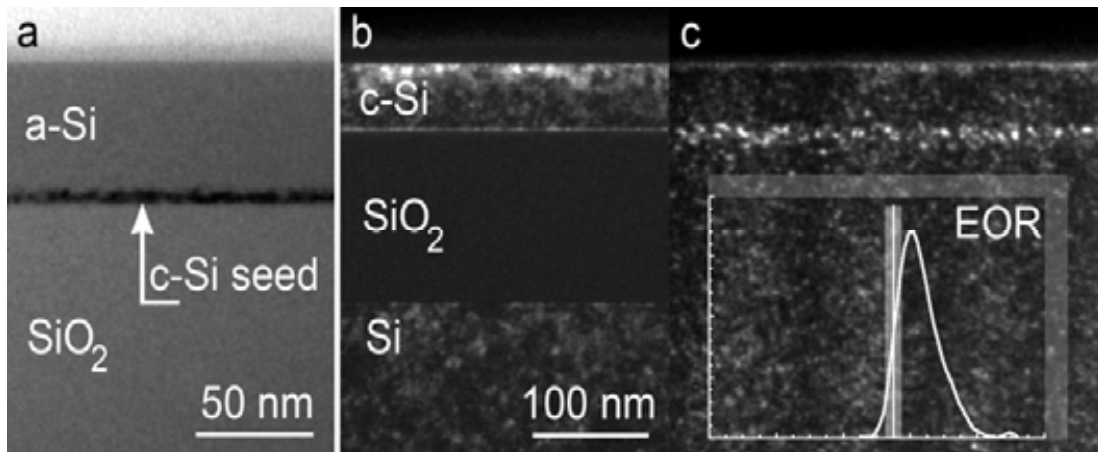


FIG. 2. XTEM micrographs of 32keV Ge PAI B implanted SOI and bulk Si samples. a) BF micrograph of an as-implanted SOI sample; b) and c) WB (-g, g) $g=\langle 400 \rangle$, XTEM micrographs of samples annealed at 700°C for 60s in SOI and bulk Si, respectively.

The inset to Fig. 2c shows the average contrast profile obtained from this micrograph over the EOR region. For small implantation defects and the WB settings we have used, this profile should reliably track the damage depth distribution [11]. Furthermore, for a range of TEM sample thicknesses (~90–150 nm) we find a constant full width at half maximum value, of ~13 nm. The depth where the defect depth distribution would intersect the BOX interface in the SOI case is determined from figure 2b and marked as a vertical line in the inset of Fig. 3c. Clearly, for this ion energy almost all of the damage profile would be located within the BOX. This could have an important impact on activation and diffusion processes in the Si overlayer, because excess Si redistributes at a negligible rate in SiO₂ at the annealing temperatures used in this study [12], and thus cannot escape from the BOX into the Si overlayer.

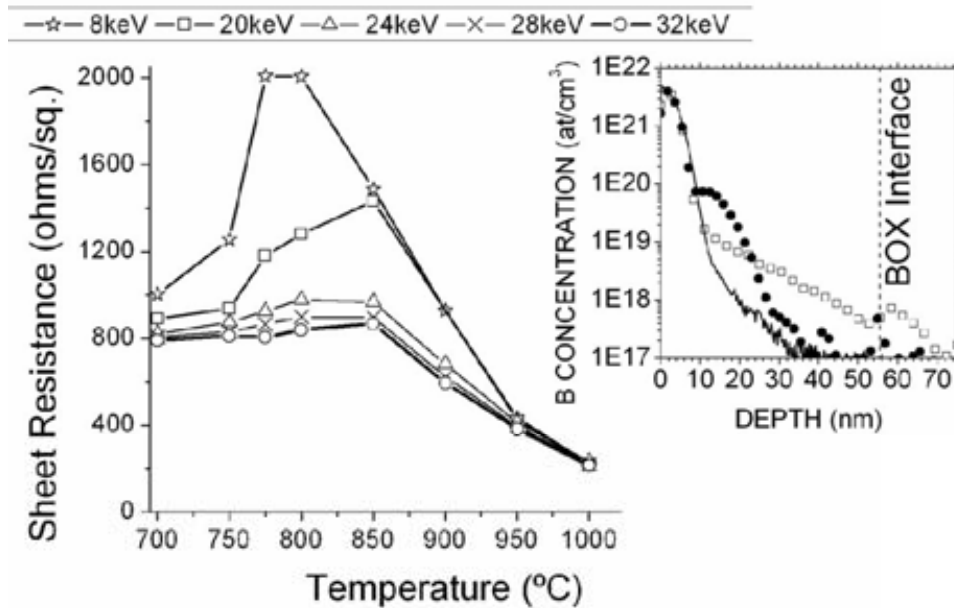


FIG. 3. Van der Pauw resistivity after 60 s isochronal anneals. Open stars, squares, triangles, crosses and circles represent 8, 20, 24, 28 and 32 keV Ge PAI in SOI, respectively. Inset are, SIMS profiles of as-implanted (solid line), 32keV Ge PAI in Bulk Si (open squares) and SOI (closed circles) annealed at 850°C for 60 s.

Figure 3 demonstrates the electrical response of SOI samples with PAI conditions in the range 8–32 keV. At low PAI energies the characteristic deactivation and reactivation of B is seen, arising in the usual way from the formation and subsequent dissolution of BICs. However, as the PAI energy is increased, bringing the EOR defect band towards the BOX interface, the amount of deactivation decreases very dramatically indeed.

The effects in term of diffusion can be seen from SIMS profiles for the 32 keV PAI case, after annealing at 850°C, shown in the inset to figure 3. Comparing SOI to bulk Si, the amount of TED in the SOI is much less, the ‘kink’ concentration where the B diffuses out from the implant is higher indicating better activation, and the junction is much more abrupt. Indeed, we see for the first time in a sample that has not been co-implanted to suppress TED that the ‘kink’ level in the SOI is close to the regular solubility limit for B in silicon. These beneficial effects indicate that the number of interstitials reaching the B-doped near-surface region has been greatly reduced.

The SIMS profile for the 32 keV bulk Si sample shows a peak in the tail of the B profile, corresponding to the position of the EOR defect band (~60 nm). This peak is not seen in the SOI sample, where the excess silicon which would have formed an EOR band and caused B

deactivation has been effectively locked within the BOX. The peak in the SIMS profile at ~55 nm seen in the SOI material corresponds to B segregated at the BOX interface.

At this point the question arises as to whether, contrary to previously published arguments concerning interface recombination, all of our results might be explained in terms of the locking of the excess interstitial distribution within the BOX. To test this idea we estimate the dose of excess interstitials implanted in the Si overlayer as a function of PAI energy, using kinetic Monte Carlo (kMC) simulations. The simulated Ge implant profiles in SOI are compared with measured SIMS results to confirm the accuracy of the results.

The excess interstitial distributions for the as-implanted SOI samples were integrated from the amorphous/crystalline interface downwards in order to find the dose N_C of excess interstitials remaining within the overlayer after amorphization, and the dose N_B which was effectively locked within the BOX. The resulting fraction of excess interstitials remaining in the overlayer, $F_C = N_C / (N_B + N_C)$, is shown in Fig. 3. In the same plot we also show the amount of deactivation, expressed as the difference in active carrier density values at maximum deactivation (corresponding to the R_s peaks in Fig. 2), between the two energies E and 32 keV for each Ge PAI energy. Clearly, deactivation starts to occur well before the excess interstitials are significantly cut off by the BOX, indicating that a further effect is involved.

A more accurate, yet straightforward description can be provided using a simplified model of the proportion of interstitials emerging from the EOR band that will flow to the upper part of the Si overlayer and deactivate B atoms. We first treat the EOR band geometry as a simple ‘plane’ at depth x , placed at the centroid of the excess interstitial depth distribution in the region beyond the a/c interface. This approximation enables a simple calculation of the fluxes towards the top and bottom interfaces of the Si overlayer during annealing, $\phi_1 = D_I C_{I,EOR} / (x+L_1)$, $\phi_2 = D_I C_{I,EOR} / (d-x+L_2)$, where D_I is the interstitial diffusivity, $C_{I,EOR}$ is the interstitial concentration at the EOR depth, d is the thickness of the Si overlayer and L_1, L_2 are the recombination lengths for interstitials at its upper and lower interfaces, respectively.

The fraction of interstitials flowing to the surface is then given by $F_1 = (d-x+L_2)/(d+L_1+L_2)$. As is well known [12], the recombination length at the surface, L_1 , is less than a few nm during TED and can certainly be neglected in comparison to the thickness d . We therefore have as a good approximation $F_1 = (d-x+L_2)/(d+L_2)$. This quantity, multiplied by the initial fraction in the overlayer, F_C , is plotted as a family of curves in Fig. 4, for the cases, $L_2 = (0, 10, 30, 100, \infty)$ nm. The case $L_2 \rightarrow \infty$, for which $F_1 \rightarrow 1$, corresponds to ignoring the sinking effect of the BOX interface, whereas the case $L_2 = 0$ corresponds to assuming a perfect sink. The shape of the actual deactivation curve is clearly best matched by small values of L_2 , indicating that the BOX interface is an efficient sink for interstitials, and plays an important role in the control of defects, deactivation and TED in SOI layers.

In conclusion, we have demonstrated and explained an optimal approach for preamorphization in SOI. Two phenomena are involved; a) the SOI BOX interface acts as an efficient sink for self interstitials, b) the overlap of the interstitial profile with the BOX interface cuts the initial number of interstitials within the Si overlayer. The consequent reduction in the number of interstitials driving BIC formation in the near surface region leads to more stable electrical activation, less TED, and a more abrupt junction. The optimum result is achieved by tailoring the Ge PAI to ensure that the amorphous/crystalline interface is placed as close as possible to the BOX, consistent with the requirement to maintain a single-crystal Si layer adjacent to the upper BOX interface for reliable SPER. These results provide a sound physical basis for future modelling and design for SOI based technology.

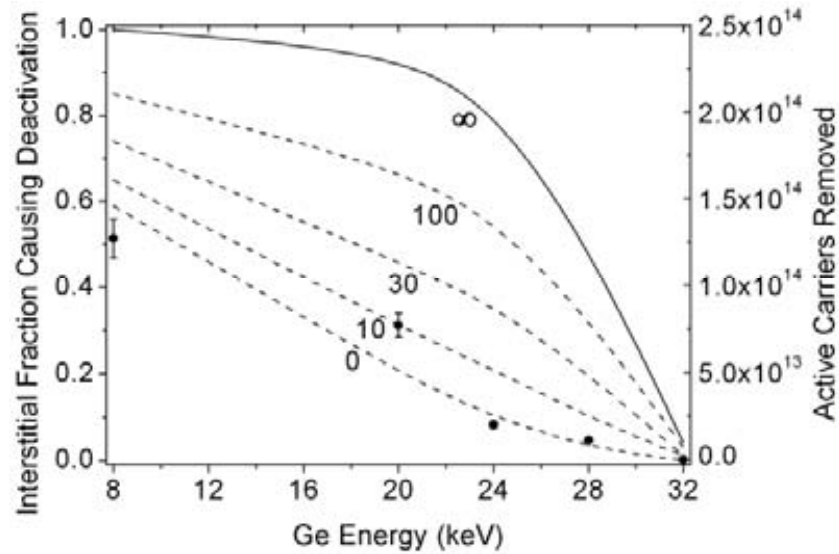


FIG. 4. Interstitial fraction causing deactivation as a function of recombination length ($L_2 = 0, 10, 30, 100, \infty$) & active carriers removed in SOI as a function of PAI energy. Represented by lines and symbols respectively (in some cases error bars are smaller than symbol size).

ACKNOWLEDGEMENTS

In addition to the IAEA the authors wish to thank the UK Engineering and Physical Sciences Research Council (EPSRC) and the Ion Beam Centre University of Surrey for their support. J.J.H. is supported by EPSRC Doctoral Training Awards.

REFERENCES

- [1] The International Technology Roadmap for Semiconductors, 2005.
- [2] LINDSAY, R., et al., *Mat. Res. Soc. Symp. Proc.* 765 (2003) D7.4.1.
- [3] CELLER, C.K., SORIN CRISTOLOVEANU, *Frontiers on Silicon-on-Insulator*, *J. Appl. Phys.* 93 (2003) 4955.
- [4] COLOMBEAU, B., et al., *Mat. Res. Symp. Proc.* 810 (2004) C3.6.
- [5] HAMILTON, J.J., et al., *Electrical activation of solid-phase epitaxially re-grown ultra-low energy boron implants in Ge pre-amorphised silicon and SOI*, *Nucl. Instrum. Methods B* 237 (2005) 107.
- [6] PAWLAK, B.J., et al., *Evidence on the mechanism of boron deactivation in Ge-preamorphized ultrashallow junctions*, *Appl. Phys. Lett.* 84 (2004) 2055.
- [7] OLSON, G.L., *Mat. Res. Soc. Symp. Proc.* 35 (1985) 25.
- [8] JEYNES, C., et al., *Elemental thin film depth profiles by ion beam analysis using simulated annealing - a new tool*, *J. Phys. D.* 36 (2003) R97.
- [9] OLSON, G.L., ROTH, J.A., *Mat. Sci. Rep.* 3 (1988) 1.
- [10] HAMILTON, J.J., et al., A., *Diffusion and activation of ultra shallow B implants in silicon-on-insulator: End-of-range defect dissolution and the buried Si/SiO₂ interface*, *Appl. Phys. Lett.* 89 (2006) 42111.
- [11] TSOUKALAS, D., TSAMIS C., NORMAND, P., *Mat. Res. Symp. Proc.* 669 (2001) J3.7.
- [12] COWERN, N.E.B., ALQUIER, D., OMRI, M., CLAVERIE, A., NEJIM, A., *Transient enhanced diffusion in preamorphized silicon: the role of the surface*, *Nucl. Instrum. Methods B* 148 (1999) 257.

PUBLICATIONS RESULTING FROM THE CRP

INTARASIRI, S., KAMWANNA, T., HALLÉN, A., YU, L.D., THONGLEUM, C., POSSNERT, G., SINGKARAT, S., *Ion Beam Synthesis of SiC Layer in Si Substrate*, NECTEC Tech. J. Vol. V, No. 16 (Nov. 2004–Oct. 2005) 634.

INTARASIRI, S., HALLÉN, A., RAZPET, A., SINGKARAT, S., POSSNERT, G., *Ion beam synthesis of silicon carbide*, Solid State Phenomena 107 (2005) 51.

INTARASIRI, S., KAMWANNA, T., HALLEN, A., YU, L.D., JANSON, M.S., THONGLEUM, C., POSSNERT, G., SINGKARAT, S., *RBS and ERDA Determinations of Depth Distributions of High-fluence Carbon Ions Implanted in Silicon for Silicon-carbide Synthesis Study*, Nucl. Instrum. Methods B 249 (2006) 859.

INTARASIRI, S., KAMWANNA, T., HALLEN, A., YU, L.D., JANSON, M.S., THONGLEUM, C., POSSNERT, G., SINGKARAT, S., *Characterization of Crystalline Quality of β -SiC Formed by Ion Beam Synthesis*, Nucl. Instrum. Methods B 249 (2006) 851.

INTARASIRI, S., HALLEN, A., LU, J., JENSEN, J., YU, L.D., BERTILSSON, K., SINGKARAT, S., POSSNERT, G., *Activation Energy of the Growth of Ion-beam-synthesized Nano-crystalline 3C-SiC*, Nucl. Instrum. Methods B 257 (2007) 195.

INTARASIRI, S., HALLÉN, A., LU, J., YU, L.D., OTTOSSON, M., JENSEN, J., SINGKARAT, S., POSSNERT, G., *Effects of Low-fluence Swift Iodine Ion Bombardment on the Crystallization of Ion-beam-synthesized Silicon Carbide*, J. Appl. Phys. 101 (2007) 084311.

INTARASIRI, S., HALLÉN, A., LU, J., JENSEN, J., YU, L.D., BERTILSSON, K., SINGKARAT, S., POSSNERT, G., *Crystalline quality of 3C-SiC formed by high-fluence C^+ -implanted Si*, Appl. Surf. Sci. 253 (2007) 4836.

HAMILTON, J.J., COWERN, N.E.B., KIRKBY, K.J., COLLART, E.J.H., BERSANI, M., GIUBERTONI, D., GENNARO, S., PARISINI, A., *Boron deactivation in pre-amorphised silicon-on-insulator: Efficiency of the buried oxide as an interstitial sink*, Appl. Phys. Lett. 91 (2007) 92122.

KAH, M., SMITH, A.J., HAMILTON, J.J., SHARP, J.A., YEONG, S.H., COLOMBEAU, B., GWILLIAM, R., WEBB, R.P., KIRKBY, K.J., *Interaction of the end-of-range (EOR) defect band with the upper buried oxide (BOX) interface for B and BF_2 implants in SOI and Si with and without pre-amorphising implant*, J. Vac. Sci. Technol. B (in press).

ABOY, M., PELAZ, L., MONSERRAT, J., BERMÚDEZ, F.J., HAMILTON, J.J., *Boron diffusion and activation in SOI and Bulk Si: The role of the buried interface*, Nucl. Instrum. Methods B 257 (2007) 152.

HAMILTON, J.J., et al., *The effect of the buried Si/SiO₂ interface on dopant and defect evolution in PAI USJ*, J. Vac. Sci. Technol. B 24 (2006) 442.

HAMILTON, J.J., COLLART, E.J.H., COLOMBEAU, B., BERSANI, M., GIUBERTONI, D., KAH, M., COWERN, N.E.B., KIRKBY, K.J., *Effect of B dose and Ge pre-amorphization energy on the electrical and structural properties of ultrashallow junctions in silicon-on-insulator*” Mater. Res. Soc. Symposium Proc. 912, (2006) C01.10.

MOK, K.R.C., COLOMBEAU, B., JARAIZ, M., CASTRILLO, P., RUBIO, J.E., PINACHO, R., SRINIVASAN, M.P., BENISTANT, F., MARTIN-BRAGADO, I., HAMILTON, J.J., *Modelling and Simulation of the Influence of SOI Structure on Damage Evolution and Ultra-Shallow Junction Formed by Ge Pre-amorphization Implants and Solid Phase Epitaxial Regrowth*, Mater. Res. Soc. Symposium Proc. 912 (2006) C03.04.

HAMILTON, J.J., COLOMBEAU, B., SHARP, J.A., COWERN, N.E.B., KIRKBY, K.J., COLLART, E.J.H., BERSANI, M., GIUBERTONI, D., PARISINI, A., *Diffusion and activation of ultra shallow B implants in silicon-on-insulator: End-of-range defect dissolution and the buried Si/SiO₂ interface*, Appl. Phys. Lett. 89 (2006) 42111.

HAMILTON, J.J., COLLART, E.J.H., BERSANI, M., GIUBERTONI, D., GENNARO, S., BENNETT, N.S., COWERN, N.E.B., KIRKBY, K.J., *Optimal pre-amorphization conditions for the formation of highly activated ultra shallow junctions in Silicon-On-Insulator*, AIP Conf. Proc., Ion Implantation Technology 866 (2006) 73.

HAMILTON, J.J., COLLART, E.J.H., COLOMBEAU, B., JEYNES, C., BERSANI, M., GIUBERTONI, D., SHARP, J.A., COWERN, N.E.B., KIRKBY, K.J., *Electrical activation of solid-phase epitaxially re-grown ultra-low energy boron implants in Ge pre-amorphised silicon and SOI*, Nucl. Instrum. Methods B 237 (2005) 107.

HAMILTON, J.J., COLLART, E.J.H., COLOMBEAU, B., BERSANI, M., GIUBERTONI, D., SHARP, J.A., COWERN, N.E.B., KIRKBY, K.J., *Understanding the role of buried Si/SiO₂ interface on dopant and defect evolution in PAI USJ*, Mater. Sci. Eng. B 124–125 (2005) 215.

COLLART, E.J.H. FELCH, S.B., GRAOUI, H., KIRKWOOD, D., TALLAVARJULA, S., VAN DEN BERG, J.A., HAMILTON, J.J., COWERN, N.E.B., KIRKBY, K.J., *Advanced front-end processes for the 45nm CMOS technology node*” Mater. Sci. Eng. B 114–115 (2004) 118.

ZHANG, K., UHRMACHER, M., KRAUSER, J., HOFSSÄSS, H., *Magnetic texturing of ferromagnetic thin films by sputtering induced ripple formation*, J. Appl. Phys., submitted.

WU, W.-Y., TING, J.-M., ZUTZ, H., LYZWA, D., GERHARDS, I., RONNING, C., HOFSSÄSS, H., *Comparative study of self-assembling of multilayers using reactive sputter deposition and mass selective ion beam deposition*, submitted to Int. Conf. on Diamond, Diamond-Like Materials, Carbon Nanotube, and Nitrides, Berlin (2007).

ZHANG, K., ROTTER, F., UHRMACHER, M., RONNING, C., HOFSSÄSS, H., KRAUSER, J., *Ion induced nanoscale surface ripples on ferromagnetic thin films with correlated magnetic texture*, New J. Phys. 9 (2007) 29.

TAKAHIRO, K., ZHANG K., ROTTER, F., SCHWEN, D., RONNING, C., HOFSSÄSS, H., KRAUSER, J., *Morphological change of carbon surfaces by sputter erosion*”, Nucl. Instrum. Methods B 256 (2007) 378.

ZHANG, K., ROTTER, F., UHRMACHER, M., RONNING, C., HOFSSÄSS, H., KRAUSER, J., *Pattern formation by Sputter erosion of Si- and C-surfaces*, Surf. Coat. Technol. 201 (2007) 8299.

HOFSSÄSS, H., ROTTER, F., UHRMACHER, M., ZHANG, K., RONNING, C., KRAUSER, J., *Sputter erosion of ferromagnetic thin films*, Surf. Coat. Technol. 201 (2007) 8477.

RONNING, C., GERHARDS, I., SEIBT, M., HOFSSÄSS, H., WU, W.Y., TING, J.M., *Self-assembled nano-scale multilayer formation using physical vapor deposition methods*, Nucl. Instrum. Methods. 242 (2006) 261.

GERHARDS, I., STILLRICH, H., RONNING, C., HOFSSÄSS, H., SEIBT, M., *Self-organized Nanoscale Multilayer Growth in Hyperthermal Ion Deposition*, Phys. Rev. B 70 (2004) 245418.

JAKŠIĆ, M., MEDUNIĆ, Z., SKUKAN, N., BOGOVAC, M., WEGRZYNEK, D., *Fabrication of a Si photodiode for position sensitive radiation detection*, IEEE Trans. Nucl. Sci. 54 (2007) 280.

JAKŠIĆ, M., BOGDANOVIĆ RADOVIĆ, I., BOGOVAC, M., DESNICA, V., FAZINIĆ, S., KARLUŠIĆ, M., MEDUNIĆ, Z., MUTO, H., PASTUOVIĆ, Ž., SIKETIĆ, Z., SKUKAN, N., TADIĆ, T., *New capabilities of the Zagreb ion microbeam system*, Nucl. Instrum. Methods B 260 (2007) 114.

SIMON, A., KALINKA, G., JAKŠIĆ, M., PASTUOVIĆ, Ž., KISS, A.Z., *Investigation of radiation damage in a Si PIN photodiode for particle detection*, Nucl. Instrum. Methods B 260 (2007) 304.

BHARUTH-RAM, K., et al., *Mössbauer study of 3C-SiC following ^{57}Mn implantation*, Proc. Int. Conf. on Applications of the Mössbauer Effect, Kanpur, India, Sept (2007) in press.

BHARUTH-RAM, K., et al., *Mössbauer spectroscopy of Fe sites and interactions in CVD diamond following ^{57}Mn implantation*, Proc. Int. Conf. on Hyp. Int., Iguasu Falls, Brasil, Aug. (2007) in press.

GUNNLAUGSSON, H.P., et al., *Defect magnetism observed with ^{57}Fe Mössbauer spectroscopy following implantation of ^{57}Mn* , Proc. Int. Conf. on Applications of the Mössbauer Effect, Kanpur, India, Sept 2007 (in press).

NAIDOO, D., et al., *^{57}Mn Mössbauer investigations in p-type SiGe single crystals*, Proc. Int. Conf. on Applications of the Mössbauer Effect, Kanpur, India, Sept (2007) in press.

WEYER, G., GUNNLAUGSSON, H.P., MANTOVAN, R., FANCIULLI, M., NAIDOO, D., BHARUTH-RAM, K., AGNE, T., *Defect-related local magnetism at dilute Fe atoms in ion-implanted ZnO*, J. Appl. Phys. 102 (2007) 113915.

BHARUTH-RAM, K., HOFSSÄSS, H., RONNING, C., *^{151}Eu sites in GaN*, Proc. Int. Conf. on Applications of the Mössbauer Effect, Kanpur, India, Sept (2007) in press.

WEYER, G., GUNNLAUGSSON, H.P., BHARUTH-RAM, K., DIETRICH, M., MANTOVAN, R., NAICKER, V., D.N., R.S., *Acceleration of diffusional jumps of interstitial Fe with increasing Ge concentration in Si_{1-x}Ge_x alloys observed by Mössbauer spectroscopy*, Hyp. Int., vol. 158, (2005) 417.

GUNNLAUGSSON, H.P., BHARUTH-RAM, K., DIETRICH, M., FANCIULLI, M., FYNBO, H.O.U., WEYER, G., *Identification of substitutional and interstitial Fe in 6H-SiC*, Hyp. Int. 169 (2006) 1319.

GUNNLAUGSSON, H.P., BHARUTH-RAM, K., DIETRICH, M., FANCIULLI, M., FYNBO, H.O.U., WEYER, G., *Formation of Fe-B pairs in silicon at high temperatures*, Hyp. Int. 169 (2006) 1315.

BALABANOV, S., TSVETKOVA, T., BORISOVA, E., AVRAMOV, L., ZUK, J., BISCHOFF, L., *Optical properties of Si⁺ and C⁺ implanted polymers*, Proc. IX Int. Conf. on Laser and Laser-Information Technologies, Oct.4–7 (2006) Smolyan, Bulgaria p.201.

TSVETKOVA, T., BALABANOV, S., AVRAMOV, L., BORISOVA, E., BISCHOFF, L., *Si⁺ implantation induced photoluminescence enhancement in PMMA*, Proc. 5 Int. Conf. “New Electrical and Electronic Technologies”, June 12–15 (2007) Zakopane, Poland, “Przeglad Elektrotechniczny”, ISSN 0033-2097, R.84 NR3(2008) 72.

BALABANOV, S., TSVETKOVA, T., BORISOVA, E., AVRAMOV, L., BISCHOFF, L., *Dose dependence of visible range diffuse reflectivity for Si⁺ and C⁺ ion implanted polymers*, XVth Int. Conf. on “Vacuum, Electron and Ion Technologies”, VEIT’07, Sept.17–21, 2007, Sozopol, Bulgaria, J. Phys. Conf. Series, 113 (2008) 012038.

BALABANOV, S., TSVETKOVA, T., BORISOVA, E., AVRAMOV, L., BISCHOFF, L., *Spectral distribution of UV range diffuse reflectivity for Si⁺ ion implanted polymers*, XVth Int. Conf. on “Vacuum, Electron and Ion Technologies”, VEIT’07, Sept.17–21, 2007, Sozopol, Bulgaria, J. Phys. Conf. Series, 113 (2008) 012039.

TSVETKOVA, T., BALABANOV, S., AVRAMOV, L., BORISOVA, E., ANGELOV, I., BISCHOFF, L., *Photoluminescence enhancement in ion implanted PMMA*, Vacuum (2007) in press.

TSVETKOVA, T., BALABANOV, S., AVRAMOV, L., BORISOVA, E., ANGELOV, I., BISCHOFF, L., *Photoluminescence properties of Si⁺ implanted polymers*, Vacuum (2007) in press.

MARQUES, A.C., WAHL, U., CORREIA, J.G., RITA, E., SOARES, J.C, *Lattice location and perturbed angular correlation studies of implanted Ag in SrTiO₃*, Nucl. Instrum. Methods B 249 (2006) 882.

ARAÚJO, J.P., LOPES, A.M.L., RITA, E., CORREIA, J.G., AMARAL, V.S., WAHL, U., ISOLDE COLLABORATION, *Local probe studies on oxides using radioactive Isotopes*, Mater. Sci. Forum 514 (2006) 1593.

MARQUES, A.C., CORREIA, J.G., WAHL, U., SOARES, J.C, *Study of point defects and phase transitions in undoped and Nb-doped SrTiO₃ using perturbed angular correlations*, Nucl. Instrum. Methods B 261 (2007) 604.

LIST OF PARTICIPANTS

- Bharuth-Ram, K. School of Physics
University of KwaZulu-Natal
Durban 4041
South Africa
- Hofsäss, H. Zweites Physikalisches Institut
University of Göttingen
Friedrich-Hund-Platz 1
D-37073 Göttingen
Germany
- Jakšič, M. Rudjer Boskovic Institute (RBI)
Department of Experimental Physics
Laboratory for Ion Beam Research
P.O. Box 180
10002 Zagreb
Croatia
- Kirkby, K. Advanced Technology Institute
University of Surrey
Guildford
Surrey, GU2 7XH
United Kingdom
- Milosavljević, M. Laboratory for Atomic Physics, VINČA
Institute of Nuclear Sciences
P.O. Box 522
Mike Petrovića Alsa 12-14B
11001 Belgrade
Serbia
- Tsvetkova, T. Institute of Solid State Physics
Bulgarian Academy of Sciences
72 Tzarigradsko Chaussee
1784 Sofia
Bulgaria
- Wahl, U. Instituto Tecnológico e Nuclear
Departamento Física
Estrada Nacional 10
2686-953 Sacavém
Portugal
- Yu, L. Fast Neutron Research Facility
Chiang Mai University
Chiang Mai 50200
Thailand